NASA TECHNICAL NOTE

NASA TN D-6477

EXPERIMENTAL INVESTIGATION OF THE INFLUENCE OF THE TURBULENT BOUNDARY LAYER ON THE PRESSURE DISTRIBUTION OVER A RIGID TWO-DIMENSIONAL WAVY WALL

by

Lado Muhlstein, Jr.
Ames Research Center

and

Richard G. Beranek
George C. Marshall Space Flight Center

NATIONAL AERONAUTICS AND SPACE ADMINISTRATION • WASHINGTON, D. C. • AUGUST 1971

1. Report No.	2. Government Accession No.	3. Recipient's Catalog No.
NASA TN D-6477		

4. Title and Subtitle
EXPERIMENTAL INVESTIGATION OF THE INFLUENCE OF THE TURBULENT BOUNDARY LAYER ON THE PRESSURE DISTRIBUTION OVER A RIGID TWO-DIMENSIONAL WAVY WALL

5. Report Date
August 1971

6. Performing Organization Code

7. Author(s)
Lado Muhlstein, Jr. and
Richard G. Beranek

8. Performing Organization Report No.
A-3846

10. Work Unit No.
126-14-11-04-00-21

9. Performing Organization Name and Address
Ames Research Center
Moffett Field, Calif., 94035 and
George C. Marshall Space Flight Center
Marshall Space Flight Center, Ala., 35812

11. Contract or Grant No.

13. Type of Report and Period Covered
Technical Note

12. Sponsoring Agency Name and Address
National Aeronautics and Space Administration
Washington, D.C. 20546

14. Sponsoring Agency Code

15. Supplementary Notes

16. Abstract

The static-pressure distribution was measured on the surface of a series of five rigid sinusoidal wavy wall models at Mach numbers from $M = 0.80$ to 1.35 and ratios of boundary-layer displacement thickness to model wavelength of 0.0025 to 0.13. Effects of wavelength and amplitude-to-wavelength ratio were examined. For the conditions of the tests, it is shown that the turbulent boundary layer causes a large attenuation of the pressure distribution at subsonic speeds and both an attenuation and a large phase shift relative to the inviscid case at supersonic speeds. These effects are greatest near $M = 1.0$ and decrease rapidly with increasing or decreasing Mach numbers. At supersonic Mach numbers, the pressure coefficient multiplied by $\sqrt{M^2 - 1}$ correlates closely with the thickness of the subsonic portion of the boundary layer. Results extrapolated to zero boundary-layer thickness are presented and compared with three inviscid theories.

17. Key Words (Suggested by Author(s))
Boundary layer
Wavy wall
Transonic aerodynamics
Low supersonic aerodynamics

18. Distribution Statement
Unclassified – Unlimited

19. Security Classif. (of this report)	20. Security Classif. (of this page)	21. No. of Pages	22. Price*
Unclassified	Unclassified	106	$3.00

*For sale by the National Technical Information Service, Springfield, Virginia 22151

SYMBOLS

A_1 amplitude of fundamental component of pressure-coefficient distribution determined by Fourier analysis

A_2 amplitude of second harmonic of the pressure-coefficient distribution determined by Fourier analysis

a wave amplitude, m (in.)

C_p pressure coefficient, $\frac{p - p_\infty}{q_\infty}$

H displacement of variable boundary-layer test fixture wall (0 = flush with tunnel wall), m (in.)

L wavelength, m (in.)

M Mach number

p static pressure, N/m^2 (lb/ft^2)

p_t total pressure, N/m^2 (lb/ft^2)

q_∞ dynamic pressure, $\frac{\rho_\infty U_\infty^2}{2}$, N/m^2 (lb/ft^2)

U velocity, m/s (ft/s)

x distance along wall in direction of air flow, m (in.)

y distance from wall to position in boundary layer, m (in.)

β $\sqrt{M^2 - 1}$

δ boundary-layer geometric thickness, distance from wall to point where $\frac{U}{U_\infty} = 0.98$, m (in.)

$\delta_{M=1.0}$ distance from wall to point in boundary layer where M = 1.0, m (in.)

δ^* boundary-layer displacement thickness, $\int_0^\delta \left(1 - \frac{\rho U}{\rho_\infty U_\infty}\right) dy$, m (in.)

ρ density, kg/m^3 ($slugs/ft^3$)

ϕ_1 phase angle of the fundamental component of the surface pressure coefficient relative to the wall displacement (positive, leading), deg

ϕ_2 phase angle of the second harmonic of the surface static-pressure coefficient relative to the wall displacement (positive, leading), deg

$( )_\infty$ free-stream condition

EXPERIMENTAL INVESTIGATION OF THE INFLUENCE OF THE TURBULENT BOUNDARY LAYER ON THE PRESSURE DISTRIBUTION OVER A RIGID TWO-DIMENSIONAL WAVY WALL

Lado Muhlstein, Jr.
Ames Research Center

and

Richard G. Beranek
George C. Marshall Space Flight Center

SUMMARY

The static-pressure distribution was measured on the surface of a series of five rigid sinusoidal wavy wall models at Mach numbers from $M = 0.80$ to 1.35 and ratios of boundary-layer displacement thickness to model wavelength of 0.0025 to 0.13. Effects of wavelength and amplitude-to-wavelength ratio were examined. For the conditions of the tests, it is shown that the turbulent boundary layer causes a large attenuation of the pressure distribution at subsonic speeds and both an attenuation and a large phase shift relative to the inviscid case at supersonic speeds. These effects are greatest near $M = 1.0$ and decrease rapidly with increasing or decreasing Mach numbers. At supersonic Mach numbers, the pressure coefficient multiplied by $\sqrt{M^2 - 1}$ correlates closely with the thickness of the subsonic portion of the boundary layer. Results extrapolated to zero boundary-layer thickness are presented and compared with three inviscid theories.

INTRODUCTION

It has recently been shown that the thickness of the turbulent boundary layer has a large influence on the flutter boundary of flat rectangular panels at low supersonic Mach numbers (refs. 1-2). The boundary layer has also been suspected of causing large discrepancies between theory and experiment in cylinder flutter studies (ref. 3). In addition, the effects of the thickness of the boundary layer on the surface pressure distribution are of crucial interest in the study of differential ablation or "crosshatching." As a result, several attempts have been made to study the effects of the boundary layer on rigid and moving wavy surfaces (refs. 4-10, for example). In an effort to provide basic information that would be useful in developing and evaluating theoretical models, a program was undertaken to obtain detailed experimental information on the effect of the thickness of the turbulent boundary layer on the pressure distribution on a rigid, two-dimensional, sinusoidal wavy wall. Besides being applicable to the fields of panel flutter, cylinder flutter, differential ablation, and boundary-layer flow in general, this information, extrapolated to zero boundary-layer thickness, should prove useful for evaluating various inviscid flow theories in the transonic speed range.

Prior to this investigation, only one very limited experimental study (ref. 6) was made of flow past a wave-shaped wall at low supersonic Mach numbers, and two studies were made of flow past a wavy cylinder (refs. 7 and 8). Both wavy cylinder studies showed evidence of flow separation over the waves, apparently because the amplitude-to-wavelength ratio was too large. Because the present study concentrates on data in the vicinity of $M = 1.0$ where flow separation is even more likely, it was decided to use very small amplitude-to-wavelength ratios.

Tests were conducted at Mach numbers from 0.80 to 1.35 for a series of five sinusoidal wavy wall models and a flat wall model. Wavelengths of 0.05080, 0.15240, and 0.25400 m (2.0, 6.0, and 10.0 in.), and amplitude-to-wavelength ratios (a/L) of 0.005, 0.010, and 0.015 were studied. Results extrapolated to zero boundary-layer thickness are presented and compared with three inviscid theories.

APPARATUS

Models

Five sinusoidal wavy wall models were constructed. Three had wavelengths of 0.15240 m (6.00 in.) with amplitude-to-wavelength ratios (a/L) of 0.005, 0.010, and 0.015. The other two had wavelengths of 0.05080 m (2.00 in.) and 0.25400 m (10.00 in.) with an $a/L = 0.005$. A typical model is shown in figure 1; the pertinent dimensions of all the models are given in figure 2 which also shows the distribution of the static-pressure orifices.

For rigidity, the wavy wall models were constructed from 0.076 m (3 in.) thick aluminum alloy plate. The sinusoidal wave patterns were formed by a numerically controlled milling machine and the resulting surface was hand polished. Measurement showed that all surface points within any wave were within 1.27×10^{-5} m (±0.0005 in.) of sinusoidal.

Boundary-Layer Probe

The probe for measuring the boundary layer on the wavy wall models and the fixture used for varying the boundary-layer thickness are shown in figure 3 as installed in the Ames 2- by 2-Foot Transonic Wind Tunnel. The probe was designed to traverse the entire length of the model and from the surface of the model to 0.076 m (3 in.) into the tunnel stream. Probe position was controlled by a programmable servo system so that repeat measurements could be made at the same point. Measured reposition accuracy of the system was $\pm 7.62 \times 10^{-5}$ m (±0.003 in.) axially and $\pm 3.81 \times 10^{-5}$ m (±0.0015 in.) normal to the surface of the model.

The probe was attached to the wind-tunnel model support system with the probe body extending into the wind-tunnel diffuser. The probe was fully retracted from the test section while surface static pressure was measured and the struts and outboard motor pod were also removed to further reduce interference effects.

The probe was designed for maximum stiffness for positioning accuracy and for minimum interference with measured pressures. Maximum tunnel blockage by the probe was limited to 1.5 percent.

The boundary-layer total pressure was measured with a conventional pitot tube with a tip opening 1.27×10^{-4} m (0.005 in.) high and 1.52×10^{-3} m (0.060 in.) wide. The static-pressure sensing probe was a 7.62×10^{-4} m (0.030 in.) diameter stainless steel tube with a 4° included angle conical tip. Two 2.54×10^{-4} m (0.010 in.) diameter orifices were located 15 tube diameters downstream of the cone-cylinder junction. The static and total pressure probes were insulated from the remainder of the probe system and contact with the model surface was indicated electrically.

Further details of the probe system can be found in reference 11.

Wind Tunnel

The experiments were conducted in the Ames 2- by 2-Foot Transonic Wind Tunnel, which is the continuous flow type with porous test section walls surrounded by a plenum chamber (see ref. 12). Mach number is continuously variable from 0.60 to 1.40 and dynamic pressure is continuously variable from 9,576 to 71,820 Newtons/M^2 (200 to 1500 psf). Because of the installation of the traversing probe in the wind-tunnel diffuser, maximum Mach number was limited to 1.35 during these tests.

Variable Boundary-Layer Test Fixture

The fixture for varying the boundary-layer thickness consisted of a splitter plate with a sharp leading edge installed in one side wall of the wind tunnel. This splitter plate could be positioned by remote control to be flush with the wall or to project up to 0.0254 m (1 in.) into the airstream. Dimensions of the test fixture are shown in figure 4. When the splitter plate was flush with the tunnel wall, the boundary-layer thickness on the model was maximum. When the splitter plate was moved into the airstream, a portion of the tunnel wall boundary layer was directed into the plenum chamber surrounding the test section and a thinner boundary layer was established on the splitter plate. The boundary-layer thickness in the model test region was variable by this means between the approximate limits of 0.00254 and 0.03175 m (0.1 and 1.25 in.)

INSTRUMENTATION

Measurement of Pressures

Wall static pressures and boundary layer rake total pressures were measured by a scanivalve system using conventional strain gage differential pressure transducers. Pressure within the boundary layer sensed by the traversing probe system was measured by a single pressure transducer. The transducer was conncted to the probe tip by a short length of tubing to stabilize the pressure rapidly.

TEST PROCEDURE

Flow Conditions in Test Region

Typical static-pressure distributions on a flat wall in the model test area are shown in reference 1. Also shown are typical boundary layer profiles and variations of boundary layer thickness with wall position.

Data Recording Procedures

The surface static pressures for all models were recorded with the traversing probe in the fully retracted position and the struts and outboard pod removed as previously mentioned.

Detailed surveys of the boundary layers on the wavy wall models were performed at Mach numbers of 1.20 and 1.35 by measuring total-pressure profiles and static-pressure profiles during separate tunnel runs. The traversing probe could not be used at Mach numbers below 1.20 because of tunnel choking problems and interference with desired results.

A flat wall model was tested to determine the reference static pressure distribution for use in correcting the wavy wall data. These pressures were measured and recorded in the same manner as those on the wavy wall. The boundary layer on the flat wall was measured with three total-pressure rakes positioned at the four stations shown in figure 4. A different run was required for measuring the boundary layer at each station.

Data Computation

The surface static pressures measured on the wavy wall models were reduced to coefficient form. To improve accuracy, the wavy wall data used in this report were then corrected by subtracting the static-pressure coefficient that existed on the flat wall at the same station under identical test conditions. The corrections usually varied between $C_p = \pm 0.015$ and never exceeded ± 0.030. The corrected surface static-pressure coefficients for each wave with orifices at 1/16 wavelength intervals were then reduced to their Fourier components. The results are presented as the amplitude and phase angle of the fundamental component and the second harmonic. Data from the wave farthest downstream usually are not presented because they contained some effects of the traversing probe system mounted in the diffuser.

The boundary-layer velocity and Mach number profiles over the wavy wall models were obtained by first reducing the measured static-pressure and total-pressure profiles to coefficient form. These data were then used to determine the Mach number and velocity at various heights above the model surface. This procedure eliminated the effects of any slight differences in tunnel total pressure that may have existed between the static-pressure and total-pressure measurements.

The boundary-layer velocity and Mach number profiles over the flat wall model were computed from the total-pressure profile and a surface static pressure.

The height in the boundary layer at which the local Mach number was equal to 1.0 was determined from the boundary layer Mach number profile, which was first normalized by the free stream Mach number to eliminate the effects of small variations of Mach number during different tunnel runs.

RESULTS AND DISCUSSION

Influence of Boundary-Layer Displacement Thickness on the Pressure Distribution

A typical example of the corrected static-pressure distribution over the models is shown in figure 5. No separated flow or strong shock waves are apparent. The waveforms are approximately sinusoidal. The deviation from a sinusoidal pressure distribution was greatest near $M = 1.0$ and for models with large a/L because of the increased amount of mixed subsonic and supersonic flow present.

The amplitudes (A_1 and A_2) and phase angles (ϕ_1 and ϕ_2) of the pressure distributions for all five models are plotted in figures 6 to 10 as a function of the dimensionless boundary-layer displacement thickness (δ^*/L). The quantities A_1 and A_2 are the peak amplitude of the fundamental and second harmonic components of the pressure distribution as determined by Fourier analysis. The quantities ϕ_1 and ϕ_2 are the corresponding phase angles relative to the wavy wall. All data presented in this report were taken on waves with orifices at 1/16 wave intervals. It is clear that the thickness of the turbulent boundary layer has a very pronounced effect. At subsonic speeds, the effect is primarily an attenuation in amplitude, whereas at supersonic speeds the effect is both an attenuation and a phase shift.

At subsonic speeds ϕ_1 remains near 180° as predicted by inviscid theory and ϕ_2 remains near 90°. Both are essentially unchanged by changes in boundary-layer thickness. At supersonic speeds ϕ_1 is near 90° for low values of δ^*/L and increases with increasing δ^*/L. The increase in ϕ_1 with δ^*/L decreases with increasing Mach number; ϕ_2 behaves similarly except for a much greater rate of increase with δ^*/L.

The quantities A_1 and A_2 decrease with increasing δ^*/L at all Mach numbers, with the effects greatest at subsonic and low supersonic speeds, and decreasing rapidly above $M = 1.20$. Figure 9(c) at $M = 0.95$ shows that for $\delta^*/L = 0.1$, A_1 is 66 percent below its value at $\delta^*/L = 0$.

The boundary-layer thickness used in analyzing the wavy wall data is the thickness on the flat wall model at the tunnel station corresponding to the center of the wave being analyzed. When a wave center did not coincide with a point where the boundary layer was measured, the boundary-layer thickness was obtained by interpolation or extrapolation as necessary.

The boundary-layer data obtained on the wavy wall models were not used in the analysis because of the problem of determining the boundary-layer thickness for flow over a wavy wall.

Although it is expected that the profile shape as well as the thickness of the boundary layer will affect the results, no attempt has been made to analyze these data using some measure of

profile shape as a parameter. Because of the expected effect of the boundary-layer profile shape, an integrated boundary-layer thickness (δ^*) was used rather than the geometric boundary-layer thickness (δ). The integrated thickness, it is believed, would reduce the sensitivity of the data to changes in profiles. In addition, since at many conditions the pressure coefficients measured are small, the inevitable resultant scatter in the data would probably mask any systematic variation with boundary-layer profile shape. The curves shown in these figures are a cubic polynomial least squares fit to the data presented. The extrapolation of these curves to zero boundary-layer thickness is shown. Because of the limited amount of data at low values of δ^*/L for some models, the extrapolation of the least squares fit curve is somewhat uncertain. The steady component (A_0) is not presented because it was generally small and was not considered significant. Higher harmonics were generally very small and erratic except at $M = 0.95$ where A_3 was approximately 50 percent of A_2.

In figure 11, the amplitude and phase of the fundamental component and second harmonic for models 3–5 are overplotted as a function of δ^*/L. The wavelengths of these models are 0.15240, 0.05080, and 0.25400 m (6, 2, and 10 in.), respectively, with $a/L = 0.005$. This figure indicates that, within the accuracy of the data, the quantity δ^*/L is a valid dimensionless parameter. The curve shown in figure 11 is a cubic polynomial least squares fit to the combined data.

The amplitude and phase angles of the fundamental and second harmonic are presented in figure 12 as a function of a/L for various constant values of δ^*/L including zero. The amplitude of the fundamental component A_1 for $\delta^*/L = 0$ is very linear except near $M = 1.0$. At subsonic speeds, this linearity continues with increasing δ^*/L whereas at supersonic speeds, A_1 as a function of a/L becomes less linear with increasing δ^*/L.

The second harmonic A_2 generally increases at an increasing rate with increasing a/L and ranges from 10 to 20 percent of A_1 except at $M = 0.95$ where it exceeds 30 percent. It should be noted that the percentage of A_2 present generally decreases with increasing δ^*/L at subsonic Mach numbers and increases with increasing δ^*/L at supersonic Mach numbers. This occurs because at subsonic Mach numbers the boundary layer introduces lower speed flow which is more linear, whereas at supersonic Mach numbers a lower speed flow is less linear for a given value of a/L.

The linearity of A_1 alone should not be interpreted as proof of aerodynamic linearity since a sizable A_2 component is present at some conditions.

The quantity ϕ_1 is independent of a/L over the entire Mach number range whereas ϕ_2 is independent at subsonic Mach numbers but shows a small dependence on a/L at supersonic Mach numbers.

The amplitude and phase of the fundamental and second harmonic component of the pressure distribution as functions of Mach number for various fixed δ^*/L are presented in figure 13 for each model. Although some of the curves for A_1, A_2, and ϕ_2 for $\delta^*/L = 0$ are erratic, the systematic behavior of most components at intermediate values of δ^*/L indicate that these results are valid. The accuracy of the second harmonic component is expected to be much less than the accuracy of the fundamental component, particularly at conditions where the second harmonic becomes very small. In summary, the extrapolations to $\delta^*/L = 0$ should be used with discretion.

Figure 13 shows that boundary-layer effects on A_1 are large near M = 1.0 but decrease rapidly with increasing or decreasing Mach number. The effect of boundary layer thickness on phase angle is small at subsonic speeds and large over the entire supersonic speed range covered by these data. An interesting feature shown in figure 13(d) is that, for values of $\delta^*/L \simeq 0.1$, the usual large increase in A_1 near M = 1.0 is almost eliminated.

The shaded region on the plots of A_1 in figure 13 indicates the range of δ^*/L over which experimental data were obtained and is applicable to all four components (A_1, A_2, ϕ_1, and ϕ_2) for each configuration.

The results of a Reynolds number study performed at $M_\infty = 0.8$ are presented in figure 14. Amplitude and phase angle of the fundamental and second harmonic components of the static pressure coefficients are presented as a function of δ^*/L for Reynolds numbers per meter (foot) of 7.62×10^5, 1.066×10^6, and 1.676×10^6 (2.5×10^6, 3.5×10^6, and 5.5×10^6). All curves are essentially identical at all three Reynolds numbers, indicating that δ^*/L accounts for all Reynolds number effects. All other data presented in this report were obtained at a constant unit Reynolds number of 1.066×10^6 (3.5×10^6) per meter (foot).

Figure 15 presents the amplitude and phase angle of the combined data from the L = 0.05080, 0.15240, and 0.25400 m (2, 6, and 10 in.) models, a/L = 0.005, as a function of δ^*/L for the four supersonic Mach numbers. These data are plotted in one figure to show the large effect of boundary-layer thickness and Mach number.

This same information is presented in figure 16 in the form of $C_p\beta$ as a function of $\delta_{M=1.0}/L$. The quantity $\delta_{M=1.0}$ is defined as the distance from the model surface to the point in the boundary layer over the flat wall where the local Mach number is equal to 1. The determination of this quantity is discussed in the section entitled Data Computation. The pressure coefficient amplitudes A_1 and A_2 were multiplied by β to eliminate Mach number effects as predicted by linear theory. It is seen that the $\delta_{M=1.0}$ boundary-layer thickness very nearly collapses all ϕ_1 data into a single curve over the full supersonic Mach number range of these data. The differences of these curves are within the expected accuracy of these data. The quantity ϕ_2 also collapses, although not as completely as ϕ_1. However, it should be noted that the ϕ_2 data contain a much larger amount of scatter. Multiplying A_1 and A_2 by β approximately collapses the pressure coefficient amplitude data. These data conclusively demonstrate that at supersonic Mach numbers most of the amplitude attenuation and phase shift are produced by the subsonic portion of the boundary layer.

The relationship between δ^* and $\delta_{M=1.0}$ as derived from the experimental data at the four supersonic Mach numbers is shown in figure 17.

Contours of constant Mach number within the boundary layer and into the free stream are shown in figure 18 for the models with a/L = 0.005 and L = 0.05080 and 0.15240 m (2 and 6 in.) at M = 1.20 and L = 0.1524 m (6 in.) at M = 1.35. For reference purposes, δ, δ^*, and $\delta_{M=1.0}$ for the flat wall are shown at each condition. These contours of constant Mach number were derived from boundary-layer measurements made with the traversing probe at 17 stations on the L = 0.15240 m (6 in.) model and at 9 stations on the L = 0.05080 m (2 in.) model. Wall static-pressure measurements made with the probe extended and retracted indicated that interference at the probe pressure sensing point was small.

A comparison of the experimental results extrapolated to $\delta^*/L = 0$ with theoretical inviscid flow results is shown in figure 19 as a function of a/L and in figure 20 as a function of Mach number. The analytical results used for comparison are linear theory, the nonlinear transonic flow theory of Hosokawa (ref. 13) and a nonlinear method of characteristics solution. The values used for the linear theory and the nonlinear transonic flow theory of Hosokawa are taken from reference 14. The nonlinear method of characteristics results were computed using the program discussed in reference 15.

For the conditions where it is valid (fully supersonic flow) the nonlinear method of characteristics results agree well with experiment (fig. 19f) for both the amplitude and phase of the fundamental component and the amplitude of the second harmonic. The phase angle of the second harmonic is in poor agreement; however the experimental values of ϕ_2 are known to be of lower accuracy.

CONCLUSIONS

Based on analysis of the data presented showing the effects of the thickness of the turbulent boundary layer on the pressure distribution over a rigid wavy wall, the following can be concluded:

1. The thickness of the turbulent boundary layer has a large effect on the amplitude of the pressure distribution at all Mach numbers tested.

2. The thickness of the turbulent boundary layer has a small effect on phase angle of the pressure distribution at subsonic Mach numbers, but has a large effect on this quantity at supersonic Mach numbers.

3. The effect of boundary-layer thickness on both amplitude and phase angle of the pressure distribution decreases rapidly with increasing supersonic Mach number.

4. Over the supersonic Mach number range of these tests, the pressure coefficient multiplied by $\sqrt{M^2 - 1}$ correlates closely with the thickness of the subsonic portion of the boundary layer.

Ames Research Center
National Aeronautics and Space Administration
Moffett Field, Calif., 94035, April 30, 1971

REFERENCES

1. Muhlstein, Lado, Jr.; Gaspers, Peter A. Jr.; and Riddle, Dennis W.: An Experimental Study of the Influence of the Turbulent Boundary Layer on Panel Flutter. NASA TN D–4486, 1968.

2. Gaspers, Peter A., Jr.; Muhlstein, Lado, Jr.; and Petroff, Daniel N.: Further Experimental Results on the Influence of the Turbulent Boundary Layer on Panel Flutter. NASA TN D–5798, 1970.

3. Stearman, R.; Lock, M.; and Fung, Y. C.: Ames Tests on the Flutter of Cylindrical Shells. GALCIT Structural Dynamics Rep. SM 62–37, California Institute of Technology, December 1962.

4. Anderson, W. J.; and Fung, Y. C.: The Effect of an Idealized Boundary Layer on the Flutter of Cylindrical Shells in Supersonic Flow. GALCIT Structural Dynamics Rep. SM 62–49, California Institute of Technology, Dec. 1962.

5. Miles, John W.: On Panel Flutter in the Presence of a Boundary Layer. J. Aero. Space Sci., vol. 26, no. 2, Feb. 1959, pp. 81–93.

6. McClure, James D.: On Perturbed Boundary Layer Flows. Rep. 62–2, MIT Fluid Dynamics Res. Lab., June 1962.

7. Anderson, William J.: Supersonic Wind Tunnel Tests of Wavy-Walled Cylinders. Office of Aerospace Research, ARL 65–203, Oct. 1965.

8. Czarnecki, K. R.; and Monta, William J.: Pressure Distributions and Wave Drag Due to Two-Dimensional Fabrication – Type Surface Roughness on an Ogive Cylinder at Mach Numbers of 1.61 and 2.01. NASA TN D-835, 1961.

9. Zeydel, E. F. E.: Study of the Pressure Distribution on Oscillating Panels in Low Supersonic Flow With Turbulent Boundary Layer. NASA CR–691, 1967.

10. Dowell, E. H.: Generalized Aerodynamic Forces on a Flexible Plate Undergoing Transient Motion in a Shear Flow With an Application to Panel Flutter. AIAA Paper 70–76, 1970.

11. Zeydel, E. F. E.: Panel Flutter Aerodynamics. Georgia Institute of Technology, Final Report. NASA CR–69144, 1965.

12. Spiegel, Joseph M.; and Lawrence, Leslie F.: A Description of the Ames 2- by 2-Foot Transonic Wind Tunnel and Preliminary Evaluation of Wall Interference. NACA RM A55I21, 1956.

13. Hosokawa, I.: Transonic Flow Past A Wavy Wall. J. Phys. Soc. Japan, vol. 15, no. 11, Nov. 1960, pp. 2080–2086.

14. Zeydel, E. F. E.: Research Study on Panel Flutter Aerodynamics, Georgia Institute of Technology, Final Report, Project B–207, NASA CR–83826, 1967.

15. Platzer, M.; Beranek, R.; and Saunders, L.: On Some Aerodynamic Aspects of the Panel Flutter Problem. Aero-Astrodyn. Res. Rev. no. 3, Oct. 1965, pp. 23-32. NASA TM X–53389.

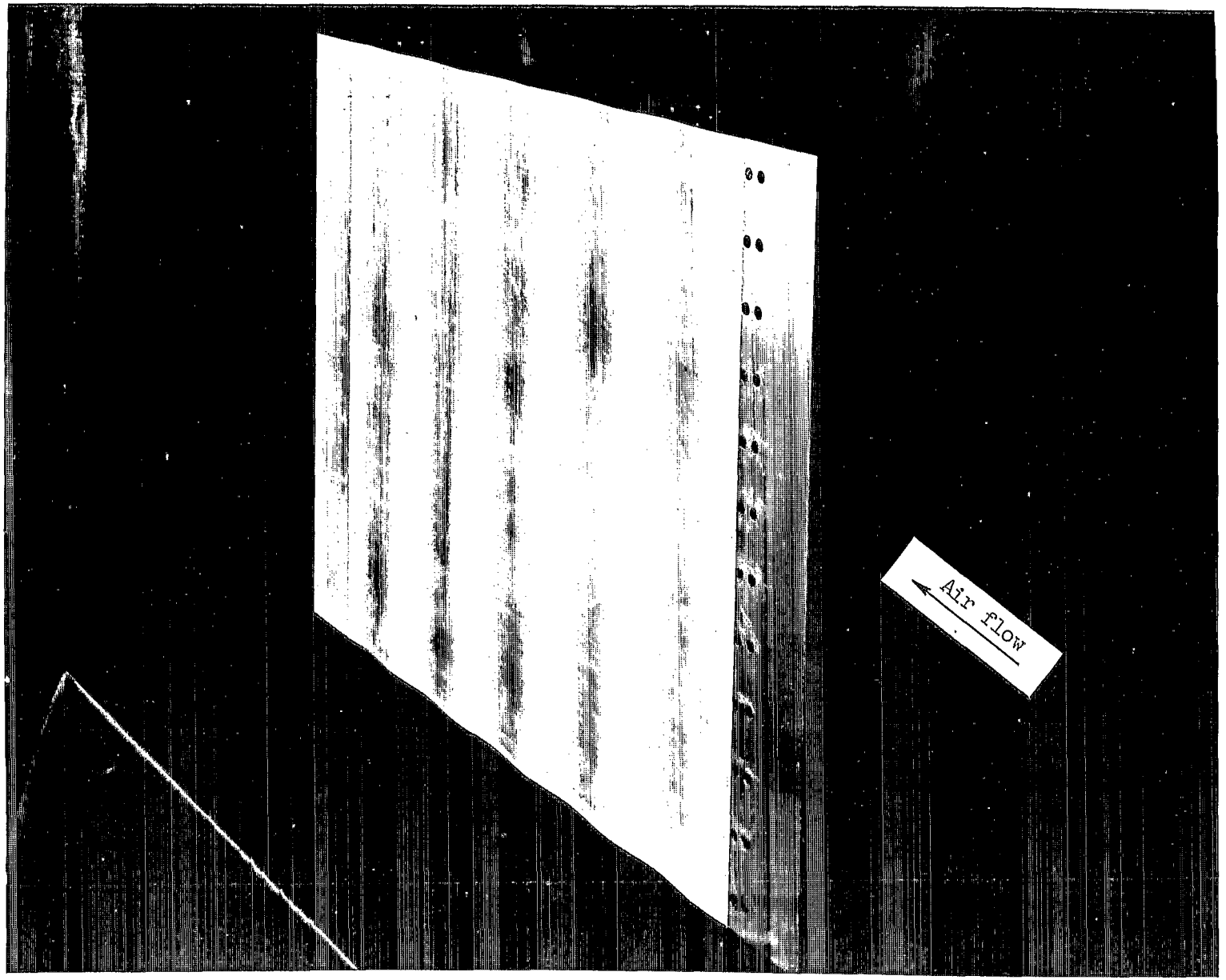

Figure 1.- Three-fourths front view of a typical wavy-wall model.

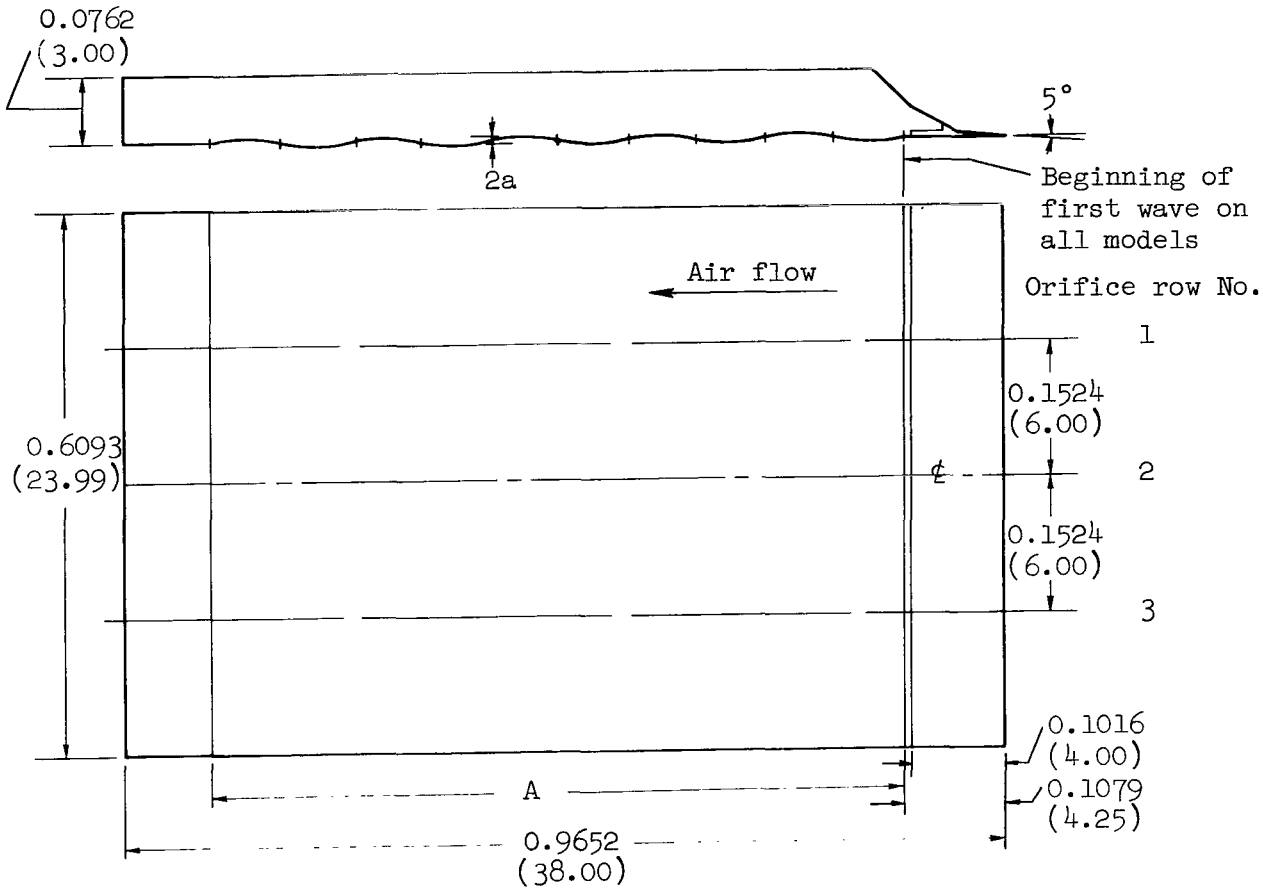

Note: All dimensions
are in m (in.)

Model	Wave-length, L, m (in.)	Amplitude a, m (in.)	Amplitude to wavelength ratio, a/L	Total number of waves	"A" dimension, m (in.)	Fully instrumented wave No. (17 orifices)
1	0.15240 (6.00)	0.002286 (0.090)	0.015	5	0.7620 (30.00)	1, 3, 5
2	0.15240 (6.00)	0.001524 (0.060)	0.010	5	0.7620 (30.00)	1, 3, 5
3	0.15240 (6.00)	0.000762 (0.030)	0.005	5	0.7620 (30.00)	1, 3, 5
4	0.05080 (2.00)	0.000254 (0.010)	0.005	16	0.8128 (32.00)	1, 5, 11, 15
5	0.25400 (10.00)	0.001270 (0.050)	0.005	3	0.7620 (30.00)	1, 2, 3

Figure 2.- Dimensions and general layout of wavy-wall models.

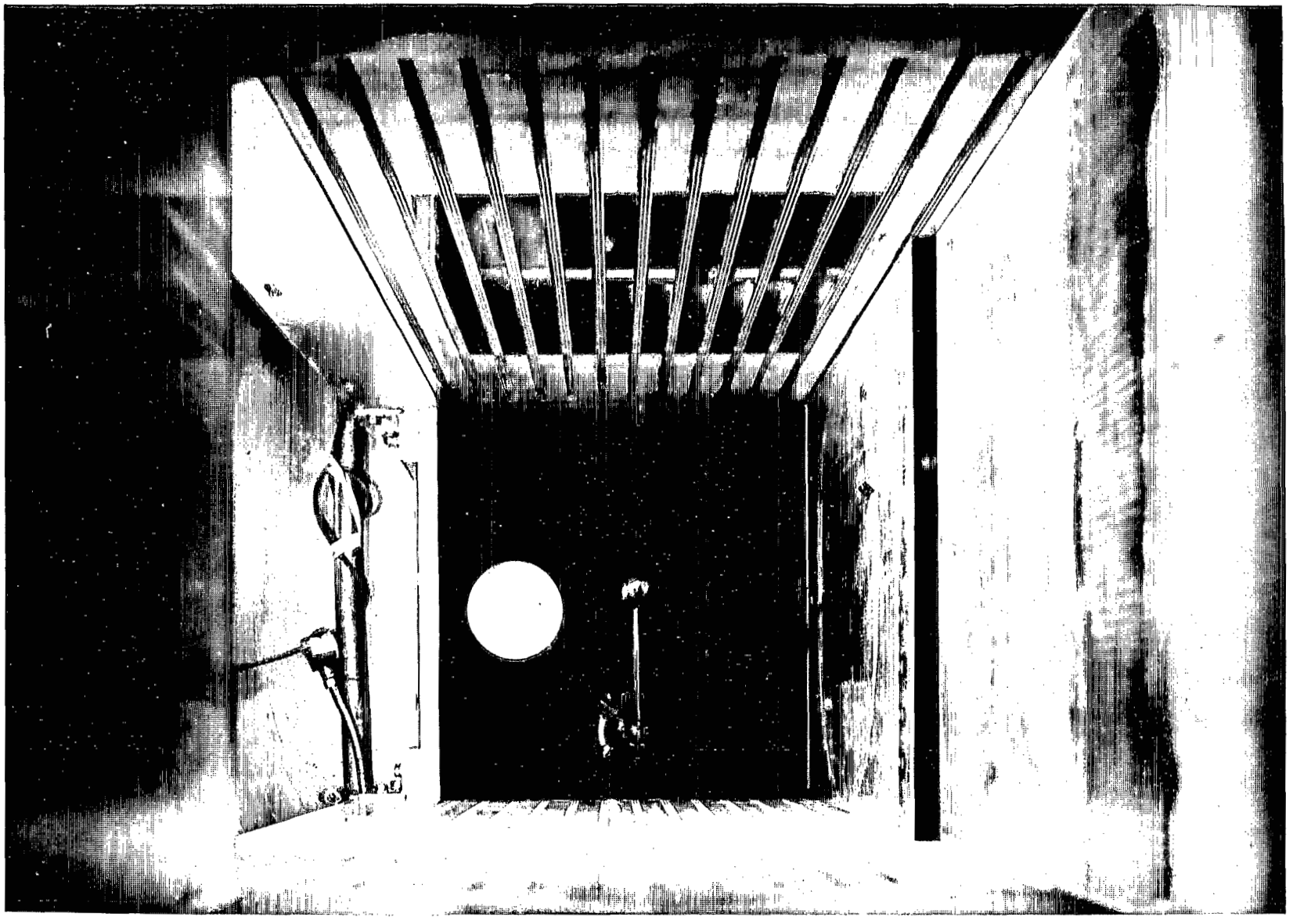

Figure 3.- Front view of traversing probe and variable boundary-layer test fixture installed in the Ames 2-by 2-Foot Transonic Wind Tunnel.

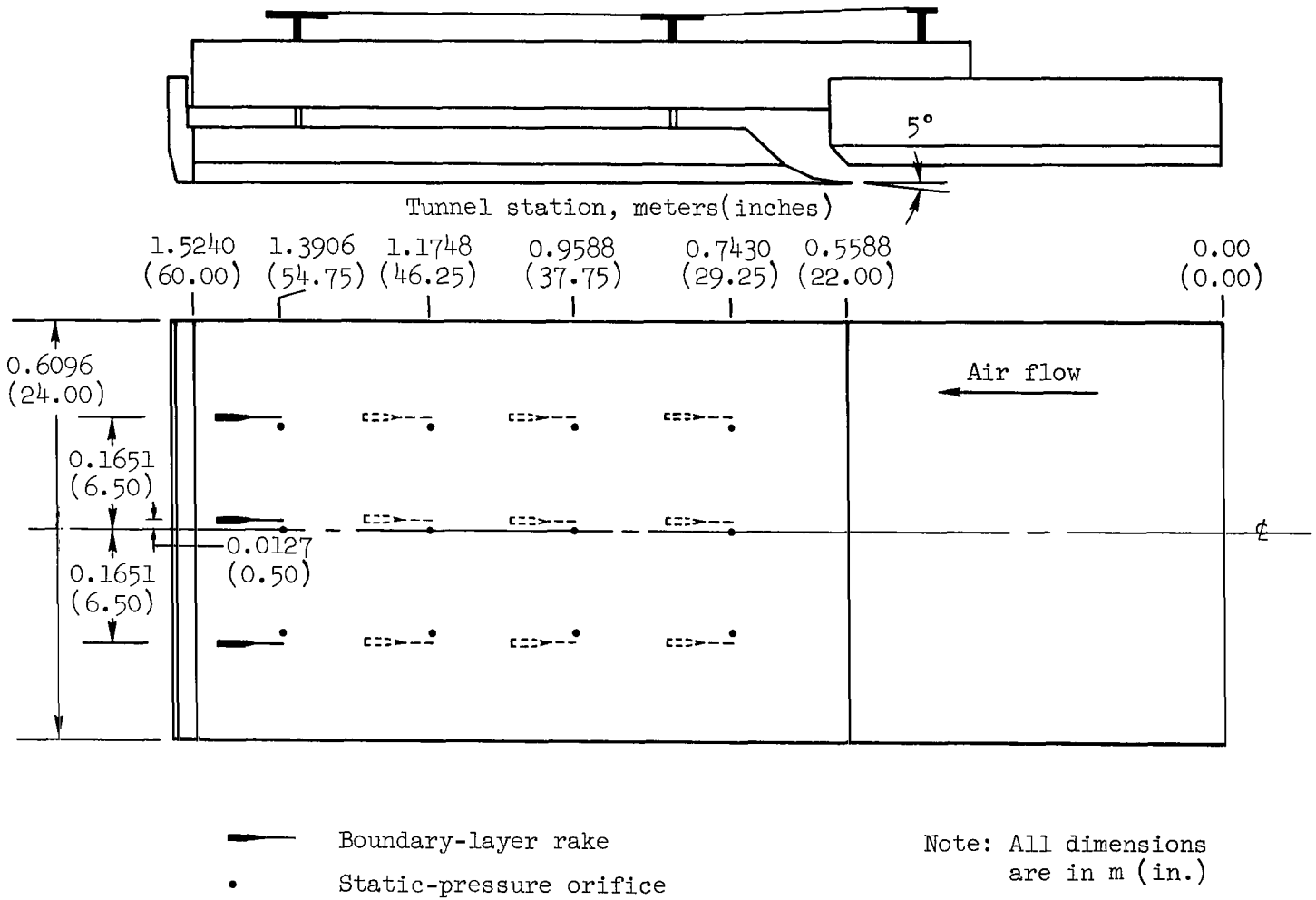

Figure 4.- Layout of variable boundary-layer test fixture.

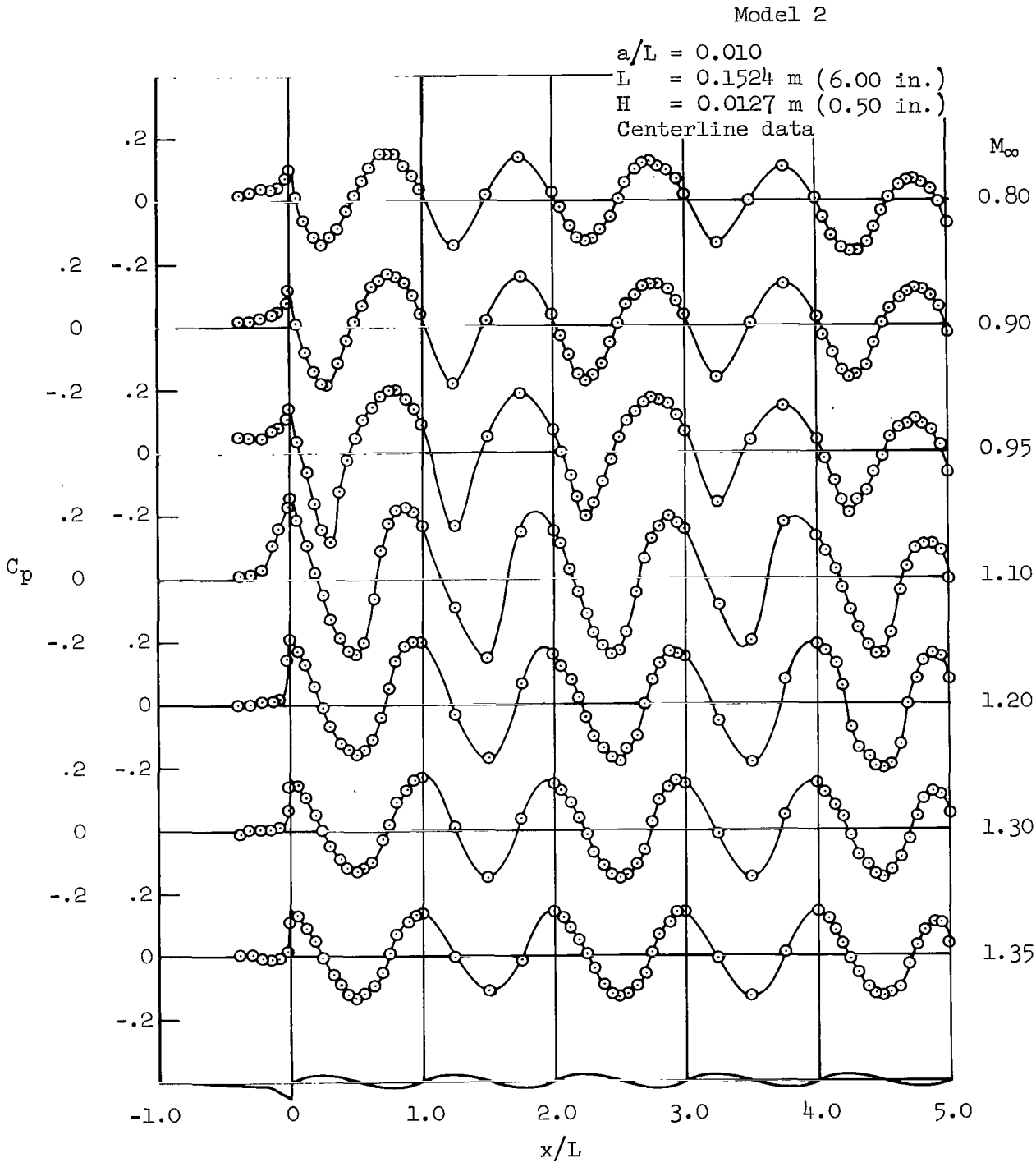

Figure 5.- Typical corrected static-pressure distributions over wavy-wall model.

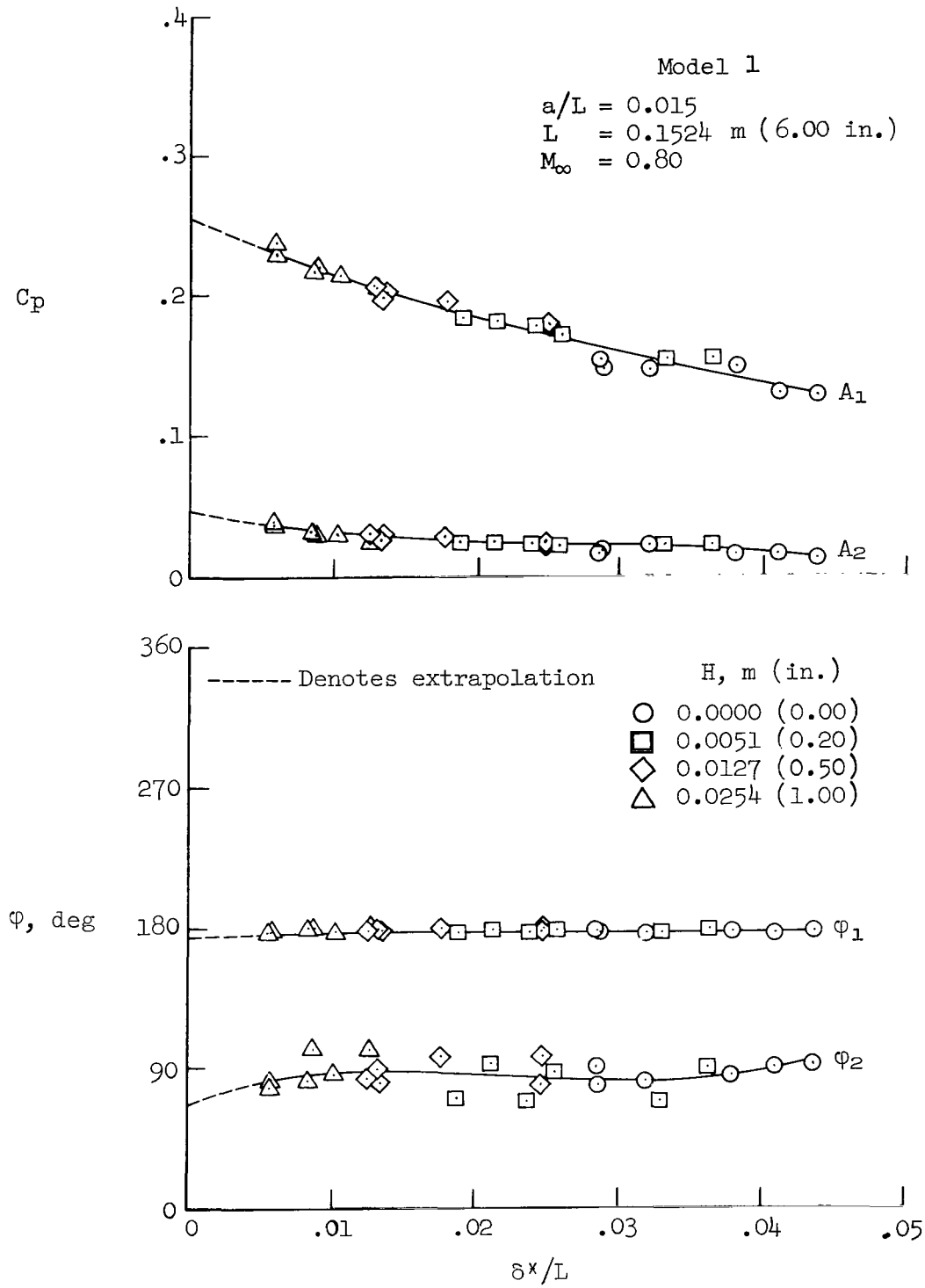

(a) $M_\infty = 0.80$

Figure 6.- Fourier components of the pressure coefficient on wavy-wall model 1 as a function of the dimensionless boundary-layer displacement thickness; a/L = 0.015, L = 0.15240 m (6.00 in.).

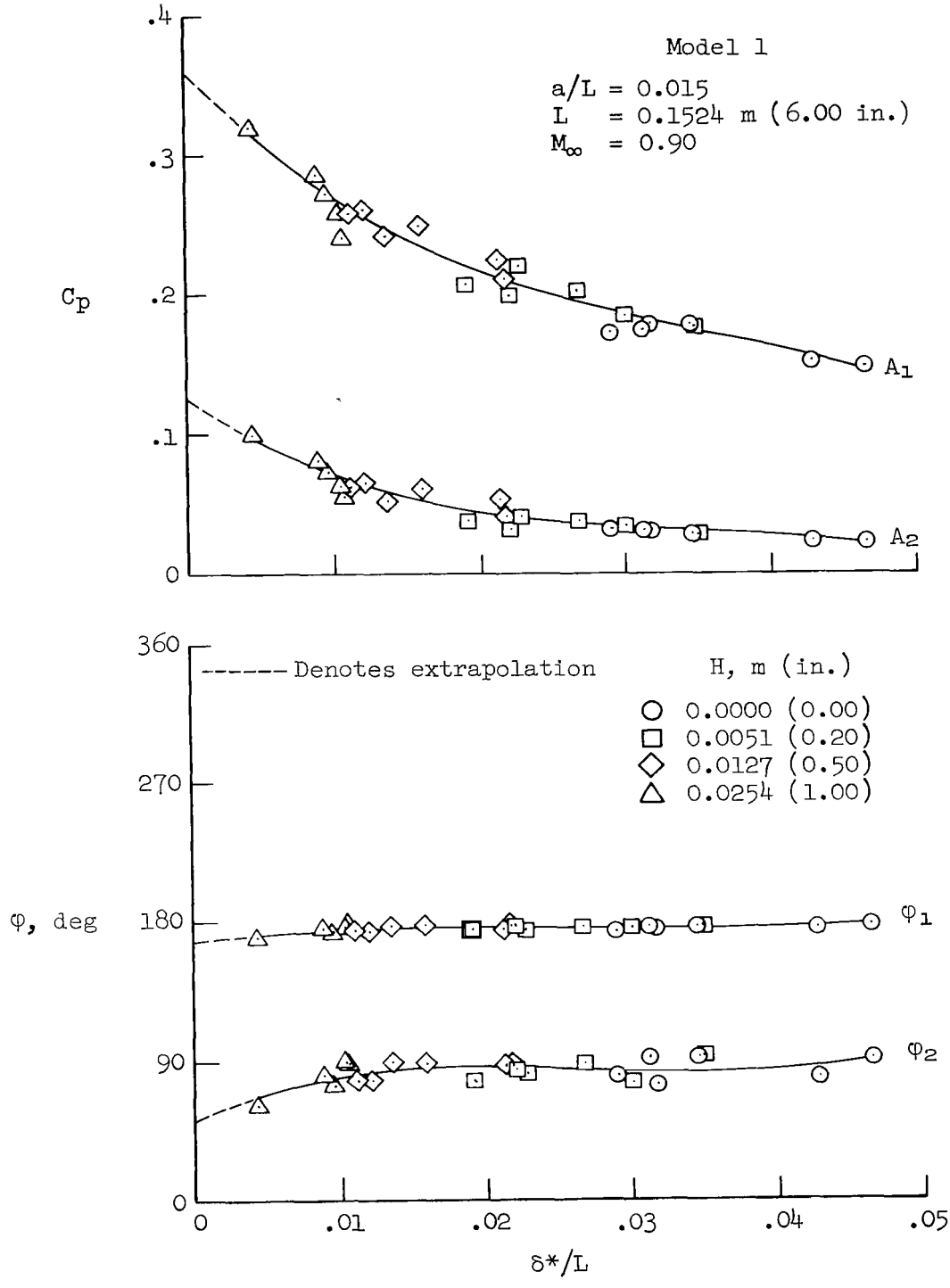

(b) $M_\infty = 0.90$

Figure 6.- Continued.

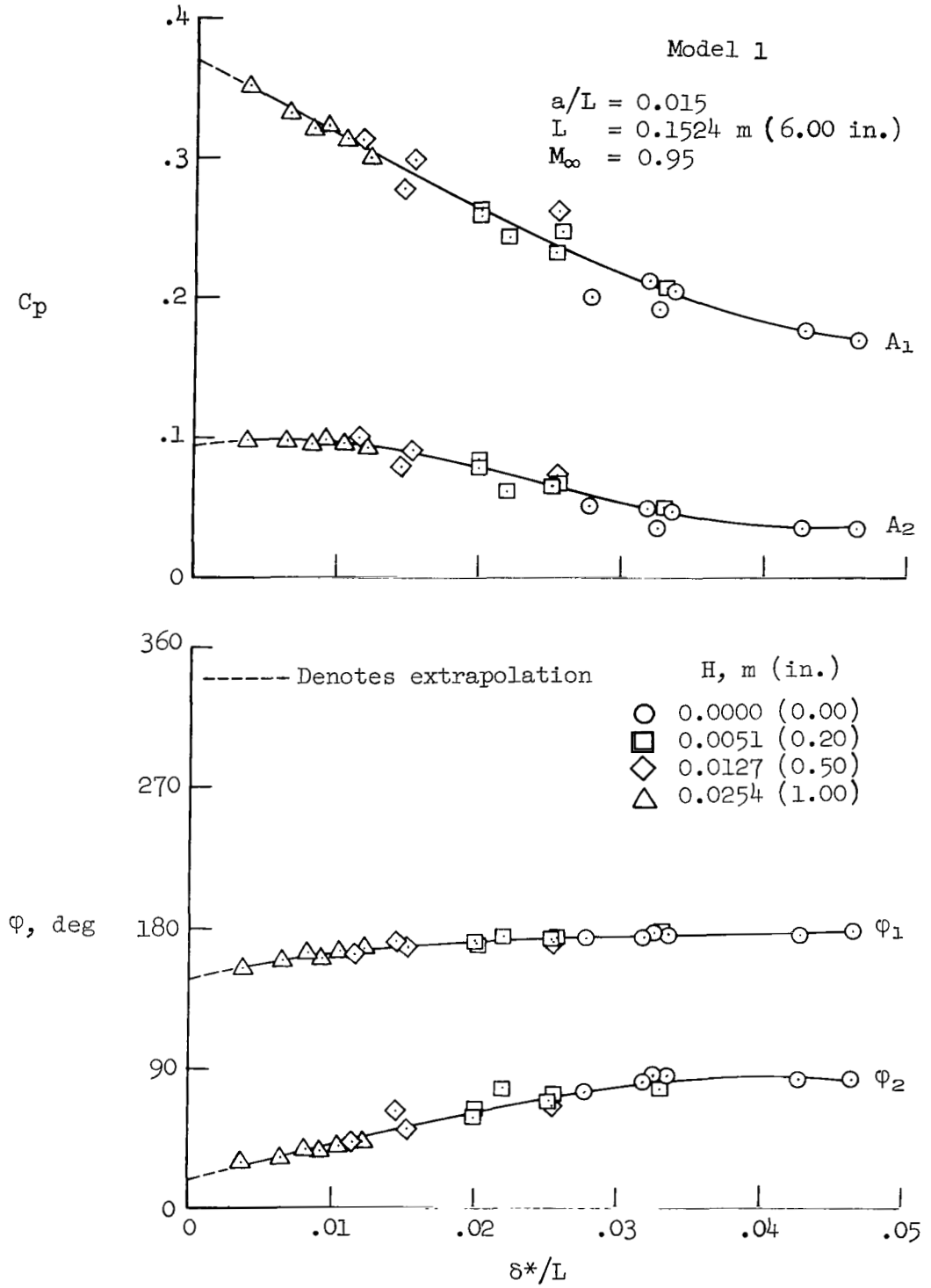

(c) $M_\infty = 0.95$

Figure 6.- Continued.

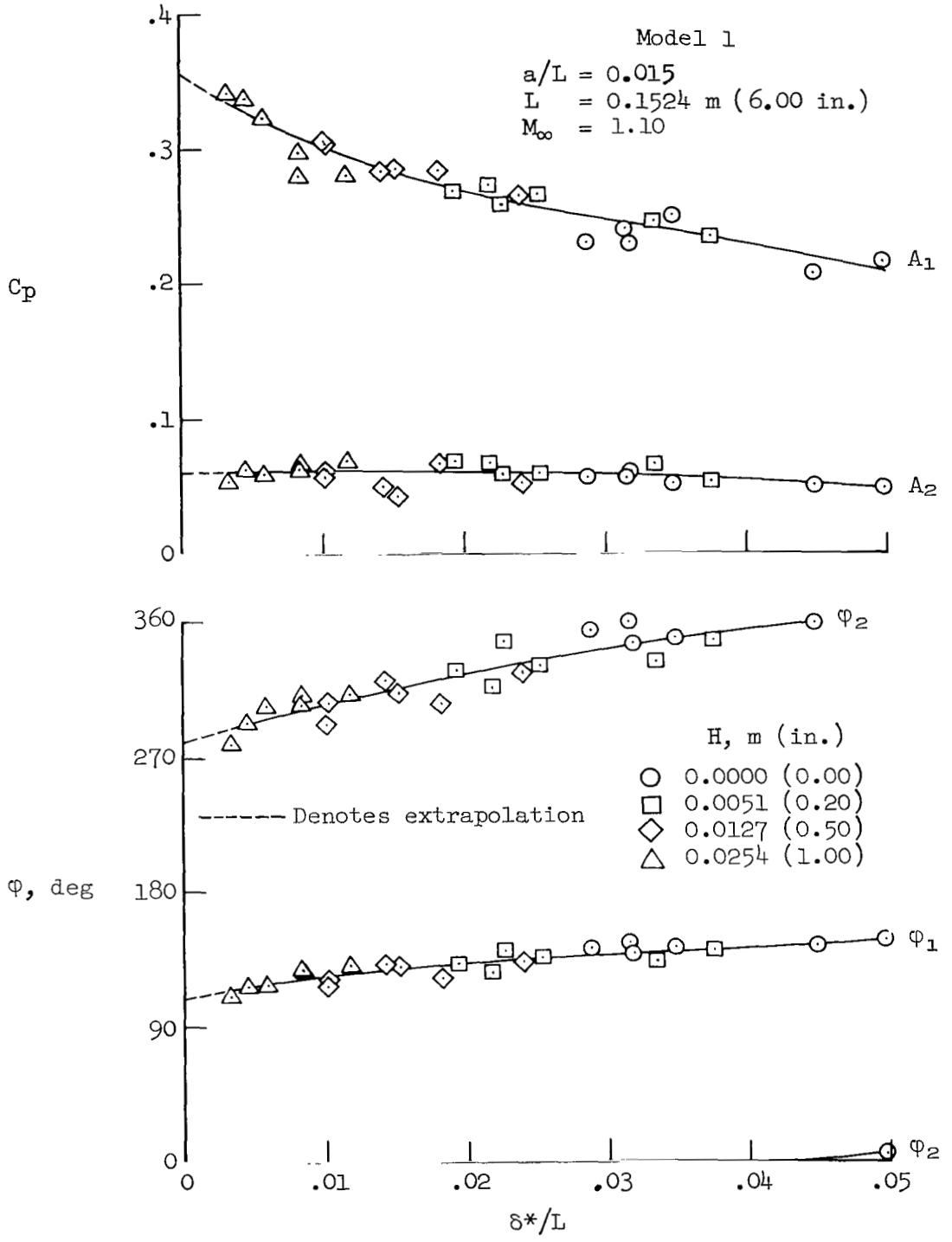

(d) $M_\infty = 1.10$

Figure 6.- Continued.

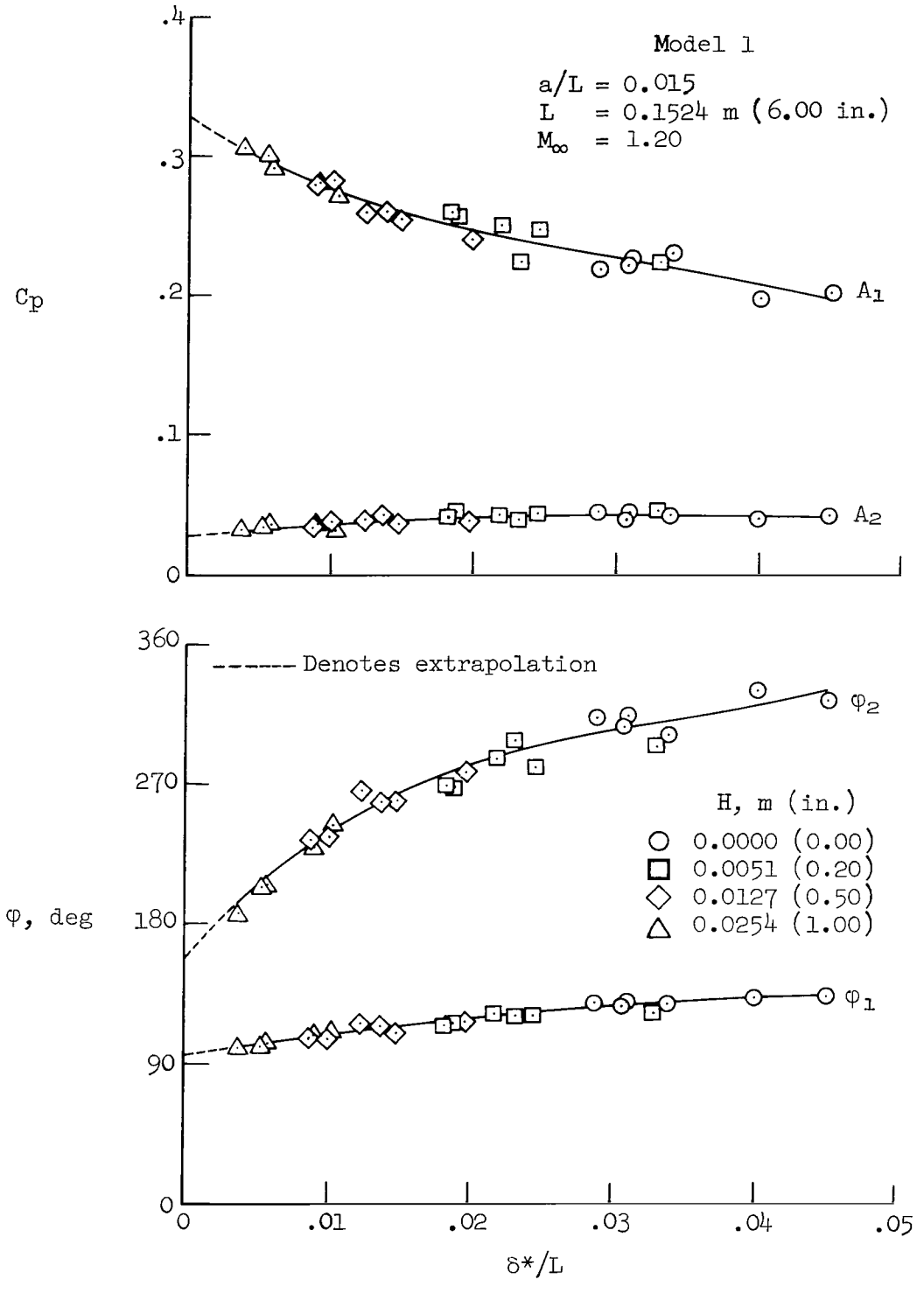

(e) M_∞ = 1.20

Figure 6.- Continued.

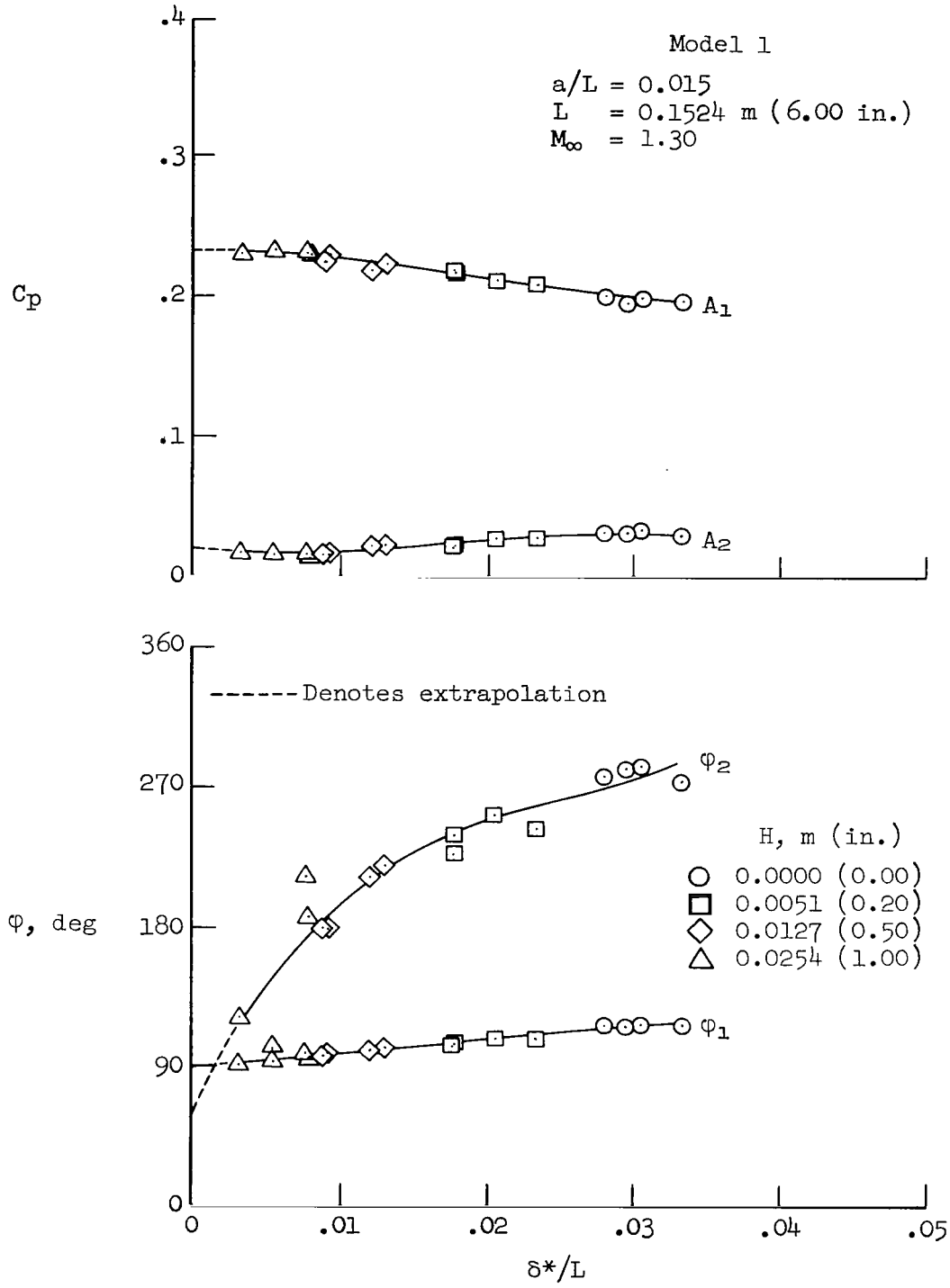

(f) $M_\infty = 1.30$

Figure 6.- Continued.

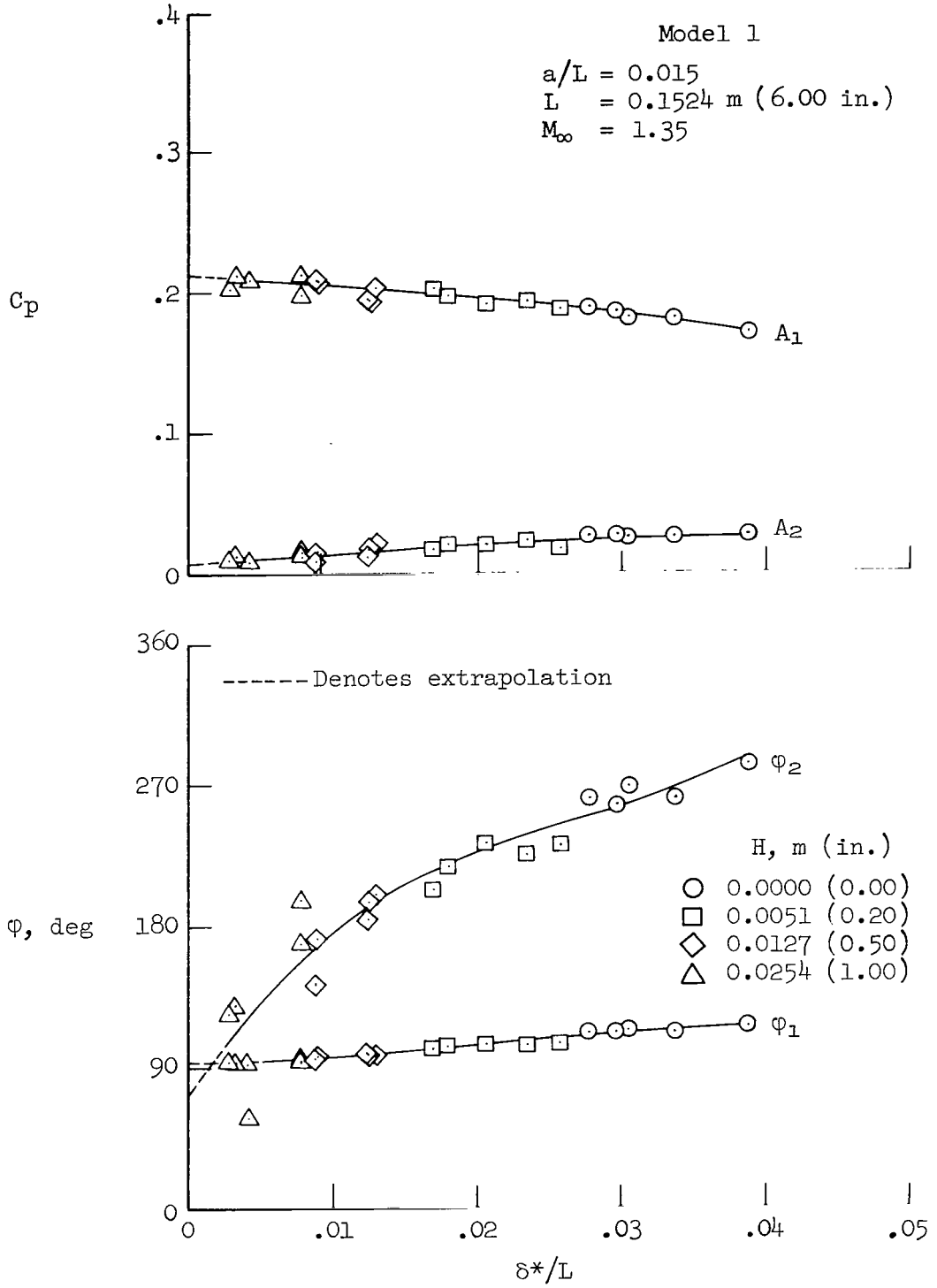

(g) M_∞ = 1.35

Figure 6.- Concluded.

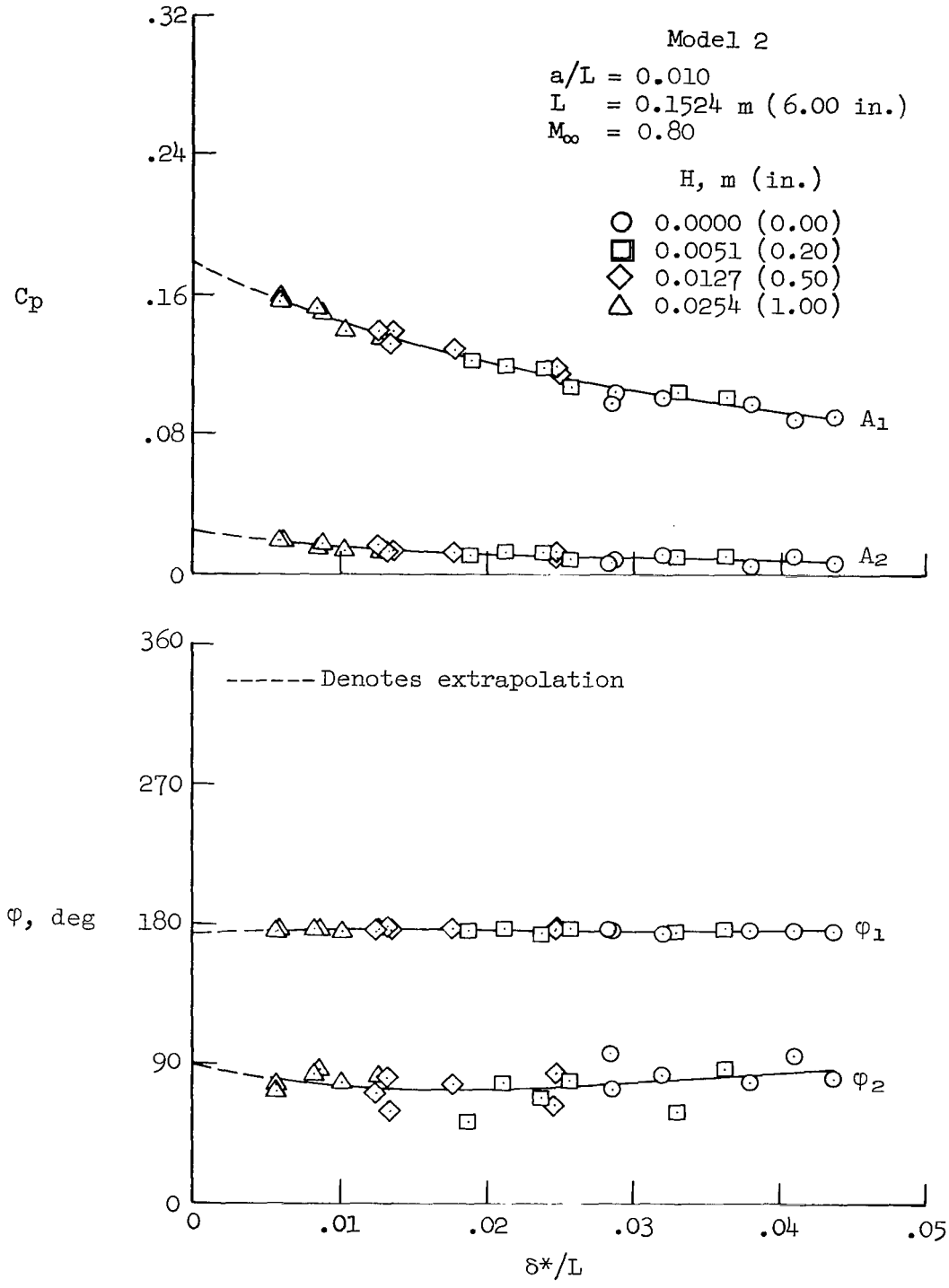

(a) M_∞ = 0.80

Figure 7.- Fourier components of the pressure coefficient on wavy-wall model 2 as a function of the dimensionless boundary-layer displacement thickness; a/L = 0.010, L = 0.15240 m (6.00 in.).

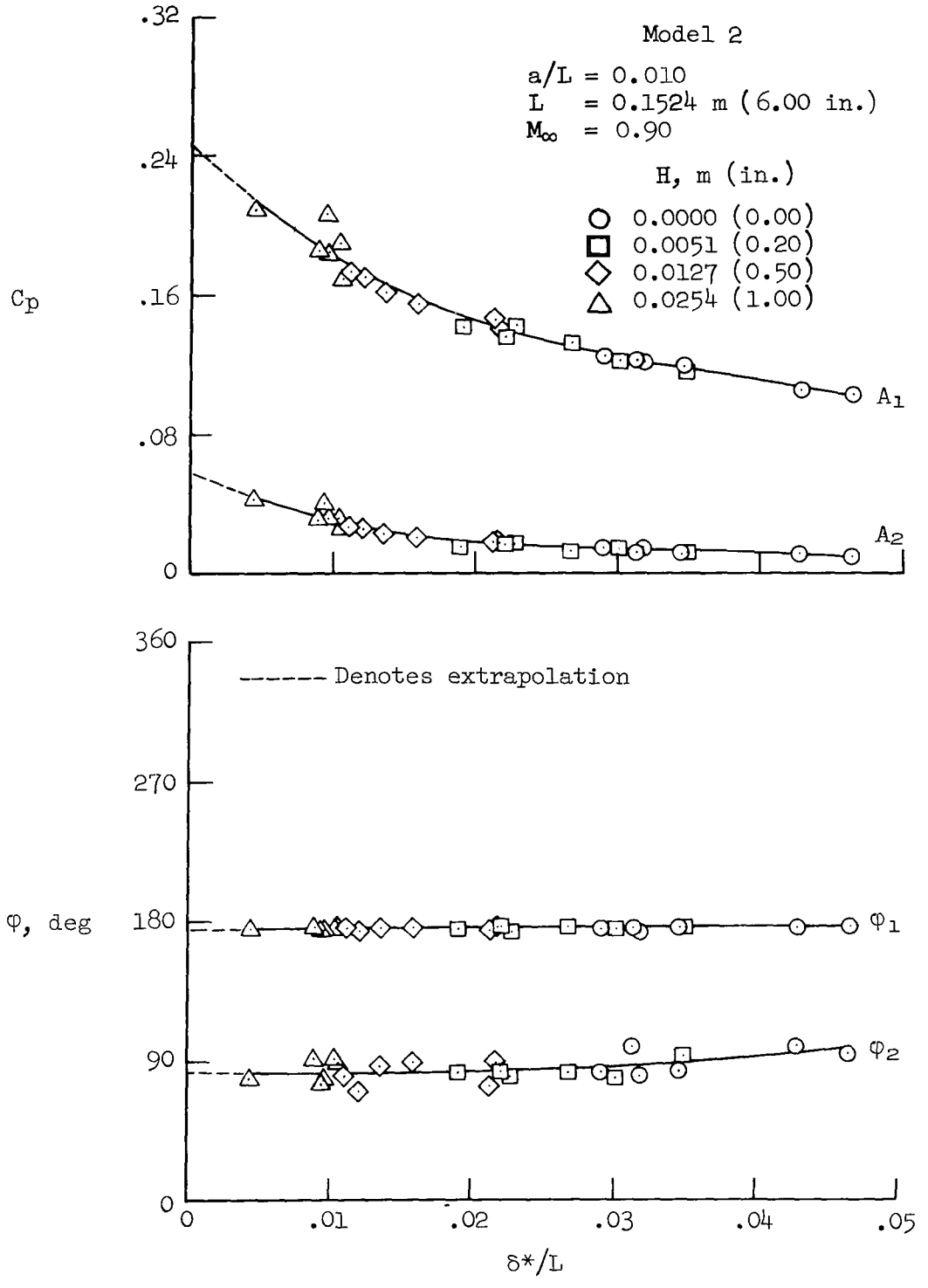

(b) $M_\infty = 0.90$

Figure 7.- Continued.

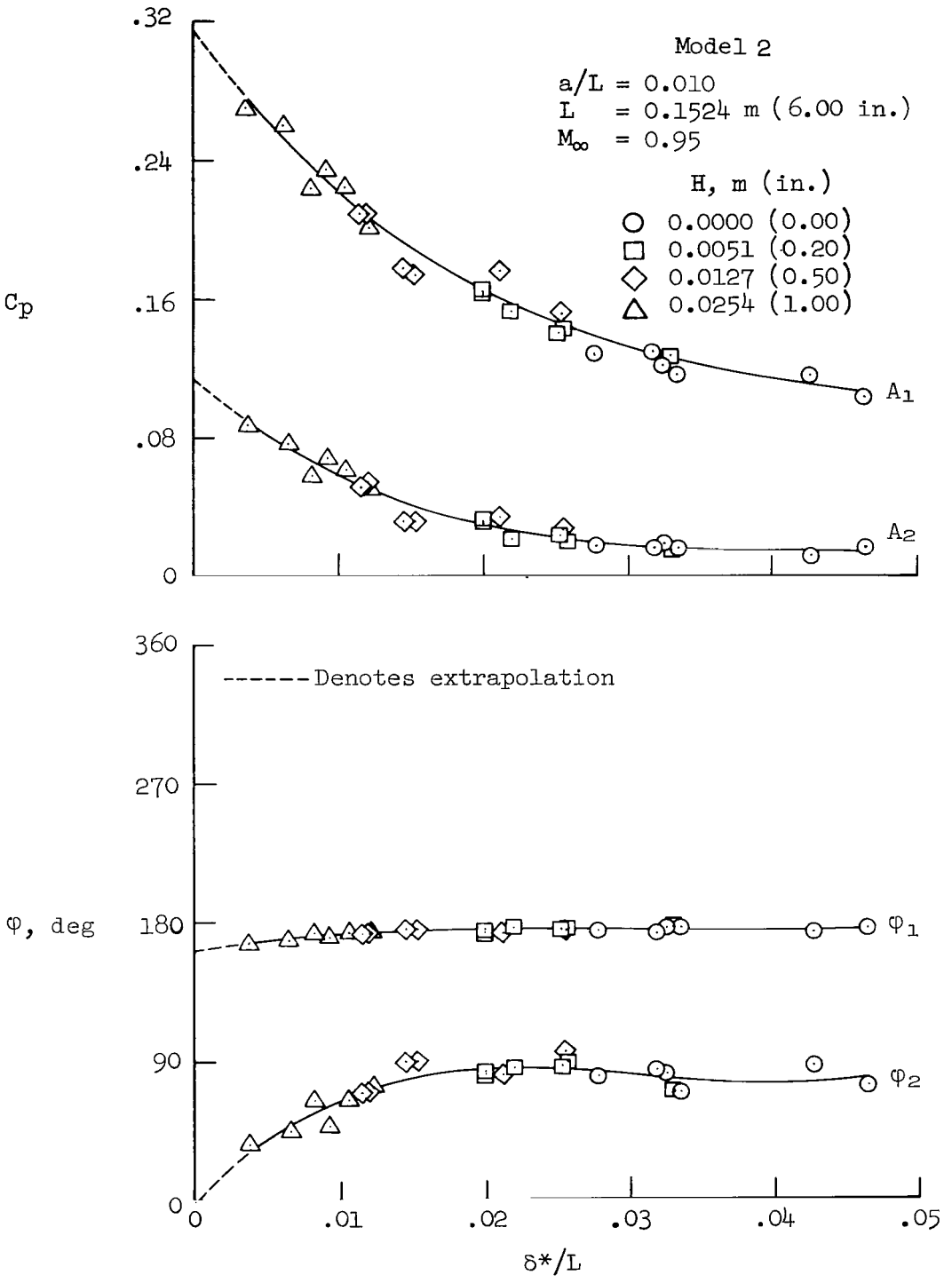

(c) $M_\infty = 0.95$

Figure 7.- Continued.

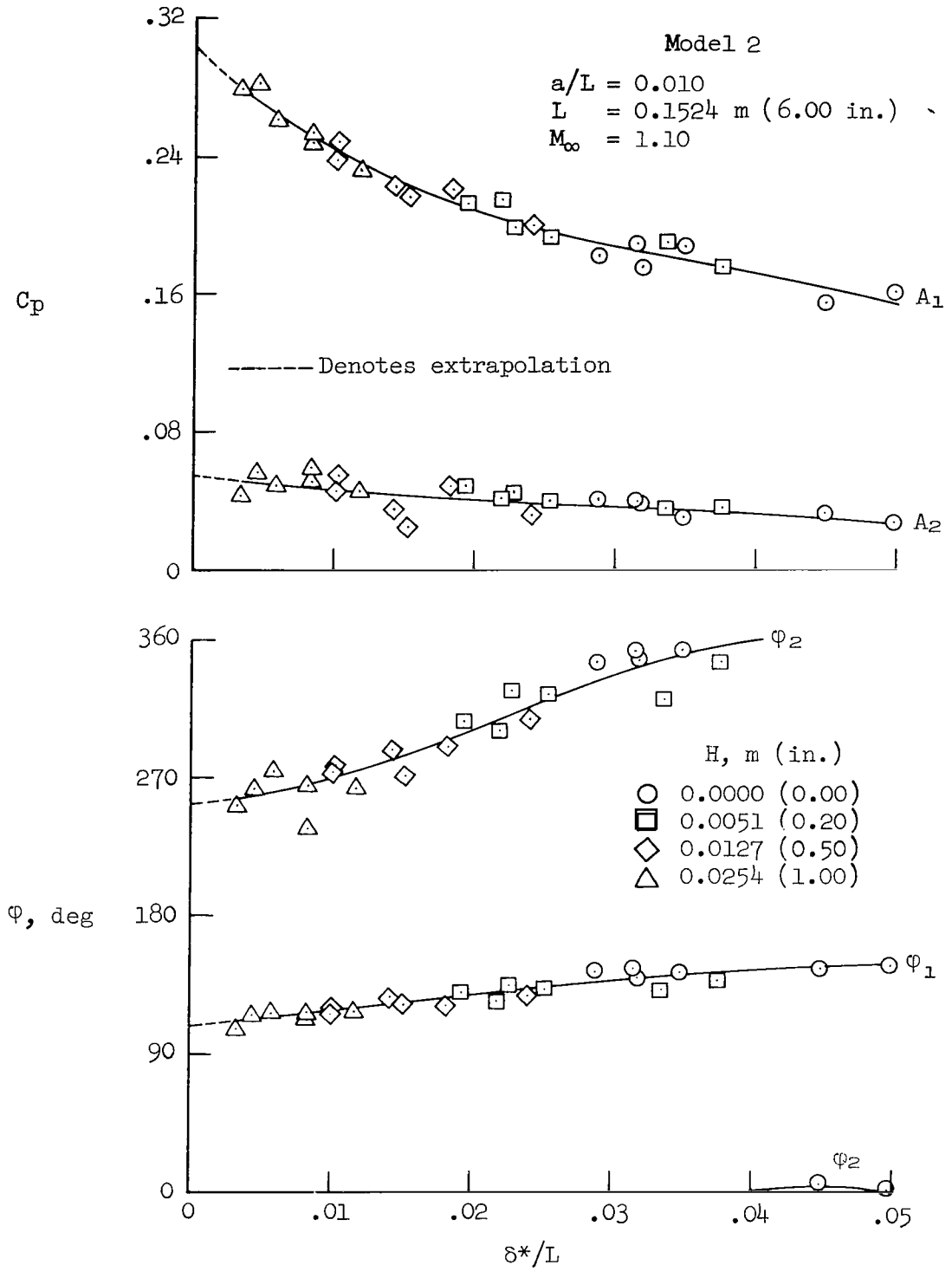

(d) $M_\infty = 1.10$

Figure 7.- Continued.

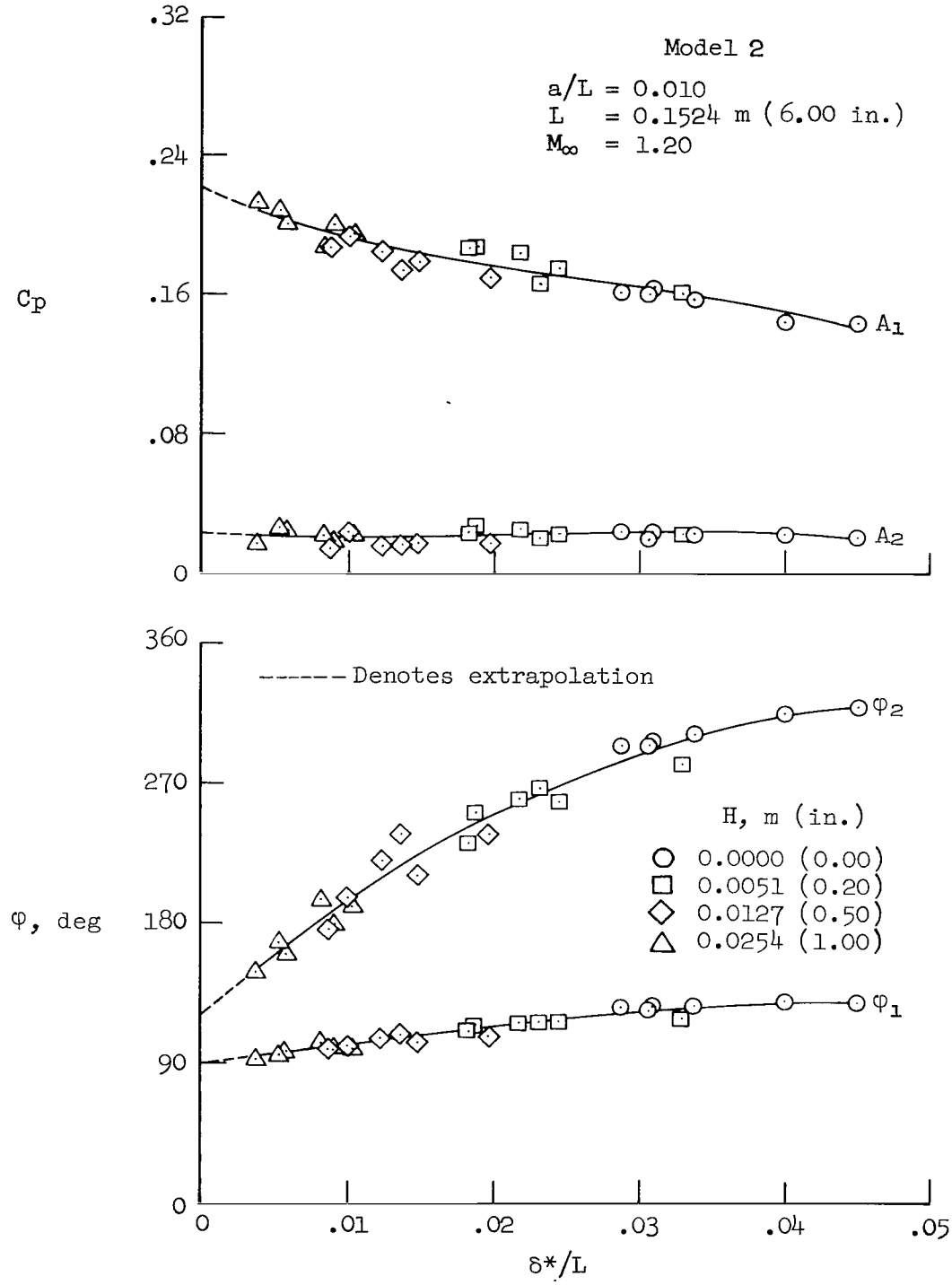

(e) $M_\infty = 1.20$

Figure 7.- Continued.

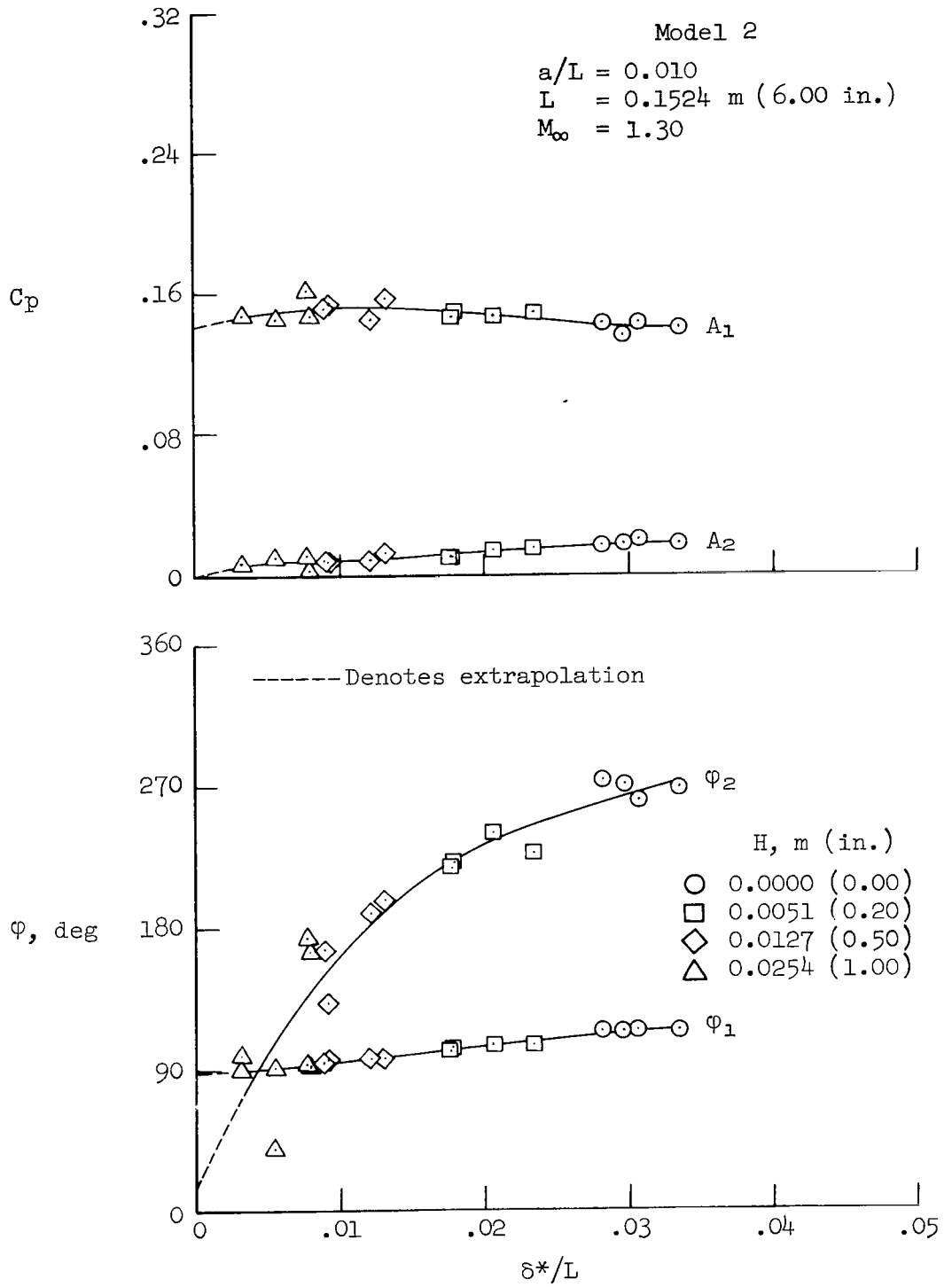

(f) $M_\infty = 1.30$

Figure 7.- Continued.

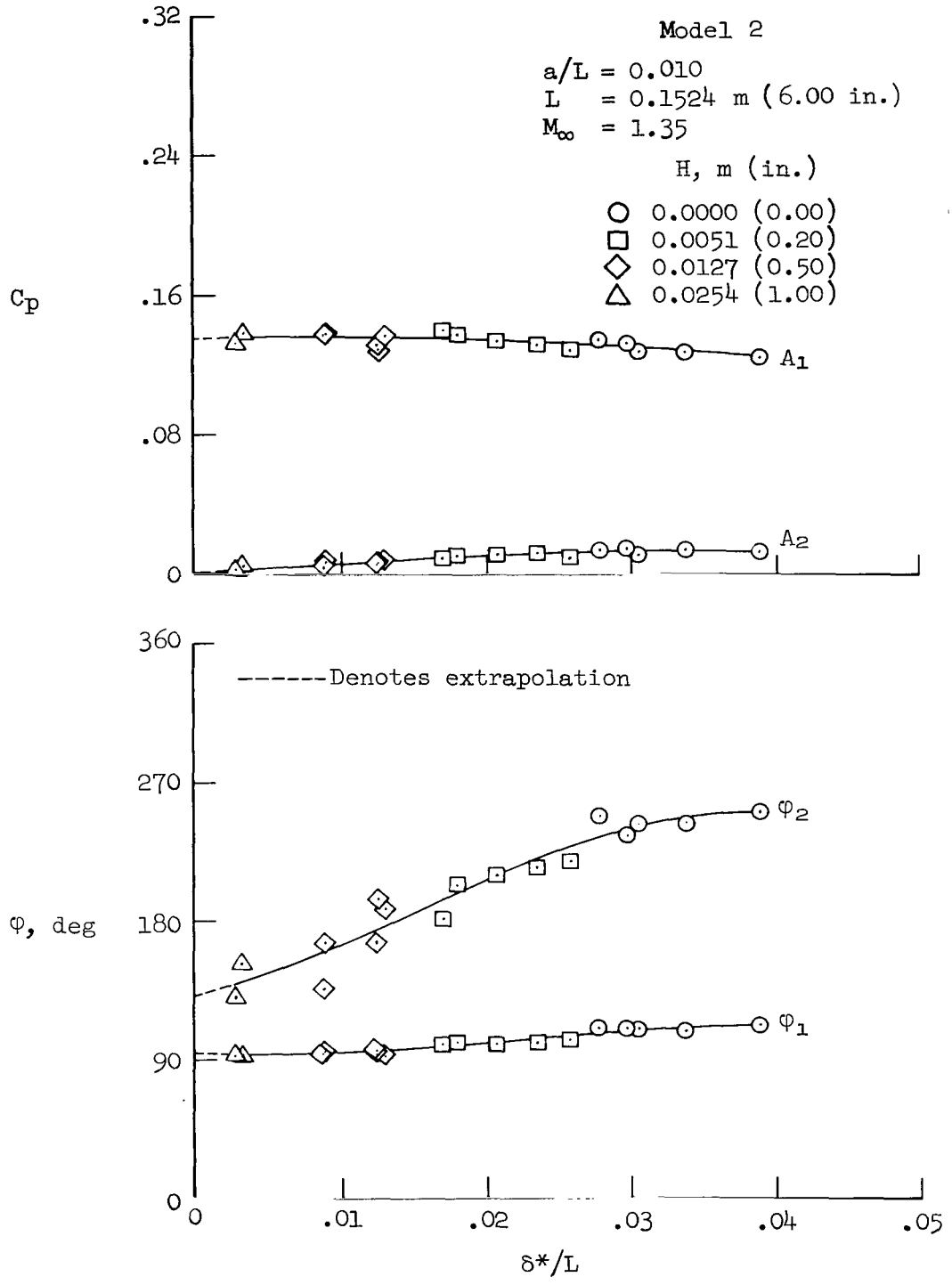

(g) M_∞ = 1.35

Figure 7.- Concluded.

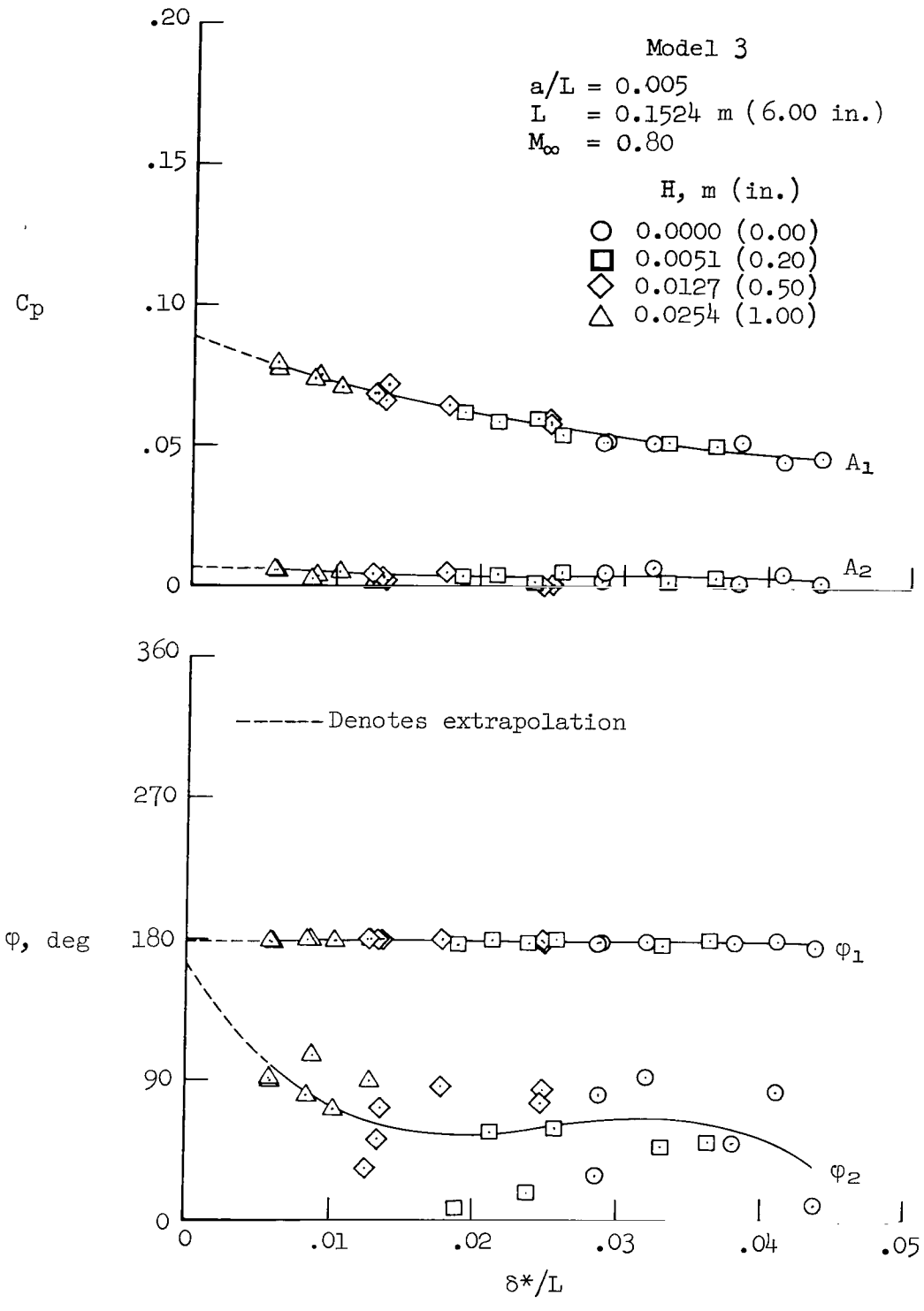

(a) $M_\infty = 0.80$

Figure 8.- Fourier components of the pressure coefficient on wavy-wall model 3 as a function of the dimensionless boundary-layer displacement thickness; a/L = 0.005, L = 0.15240 m (6.00 in.).

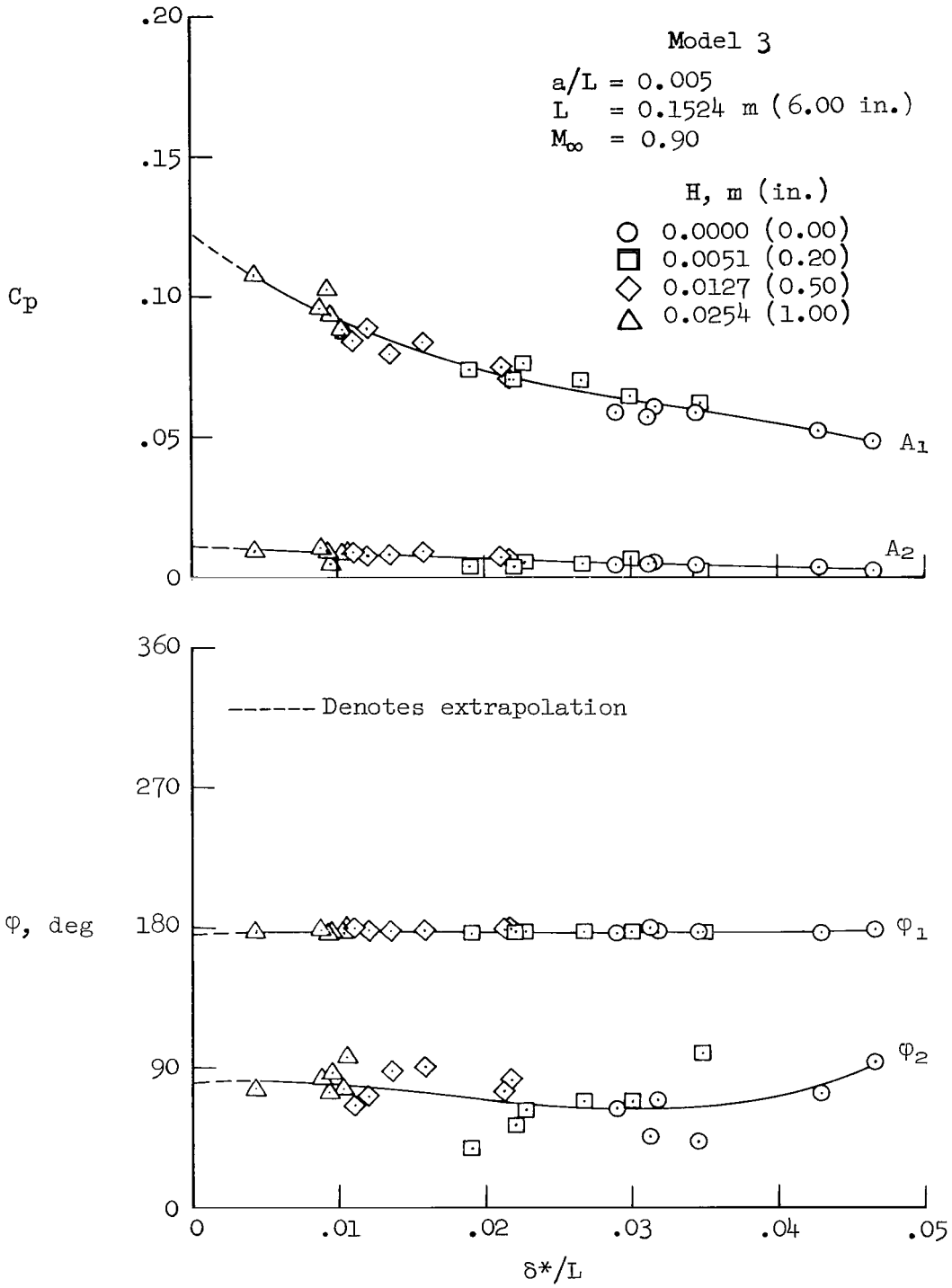

(b) $M_\infty = 0.90$

Figure 8.- Continued.

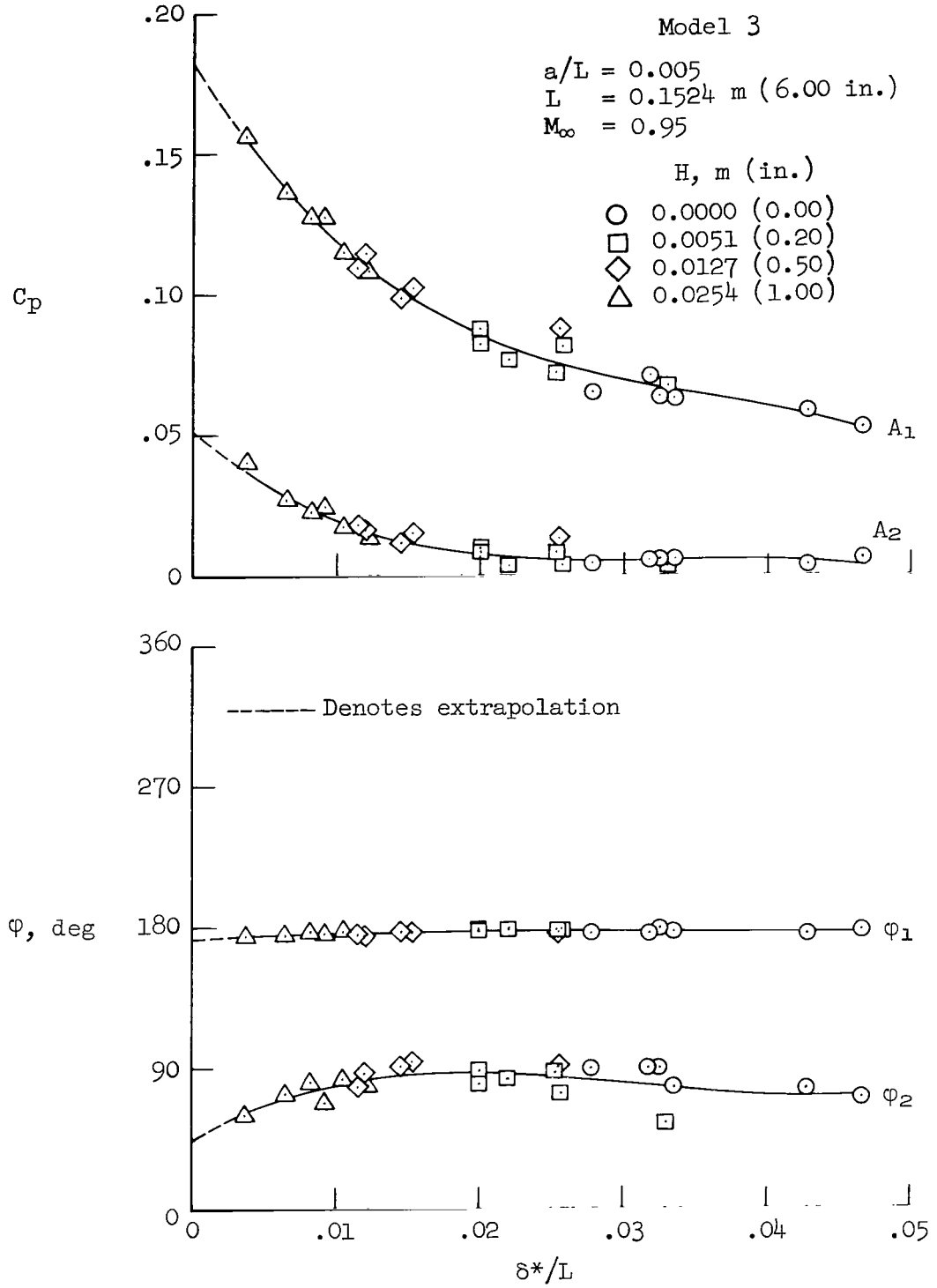

(c) $M_\infty = 0.95$

Figure 8.- Continued.

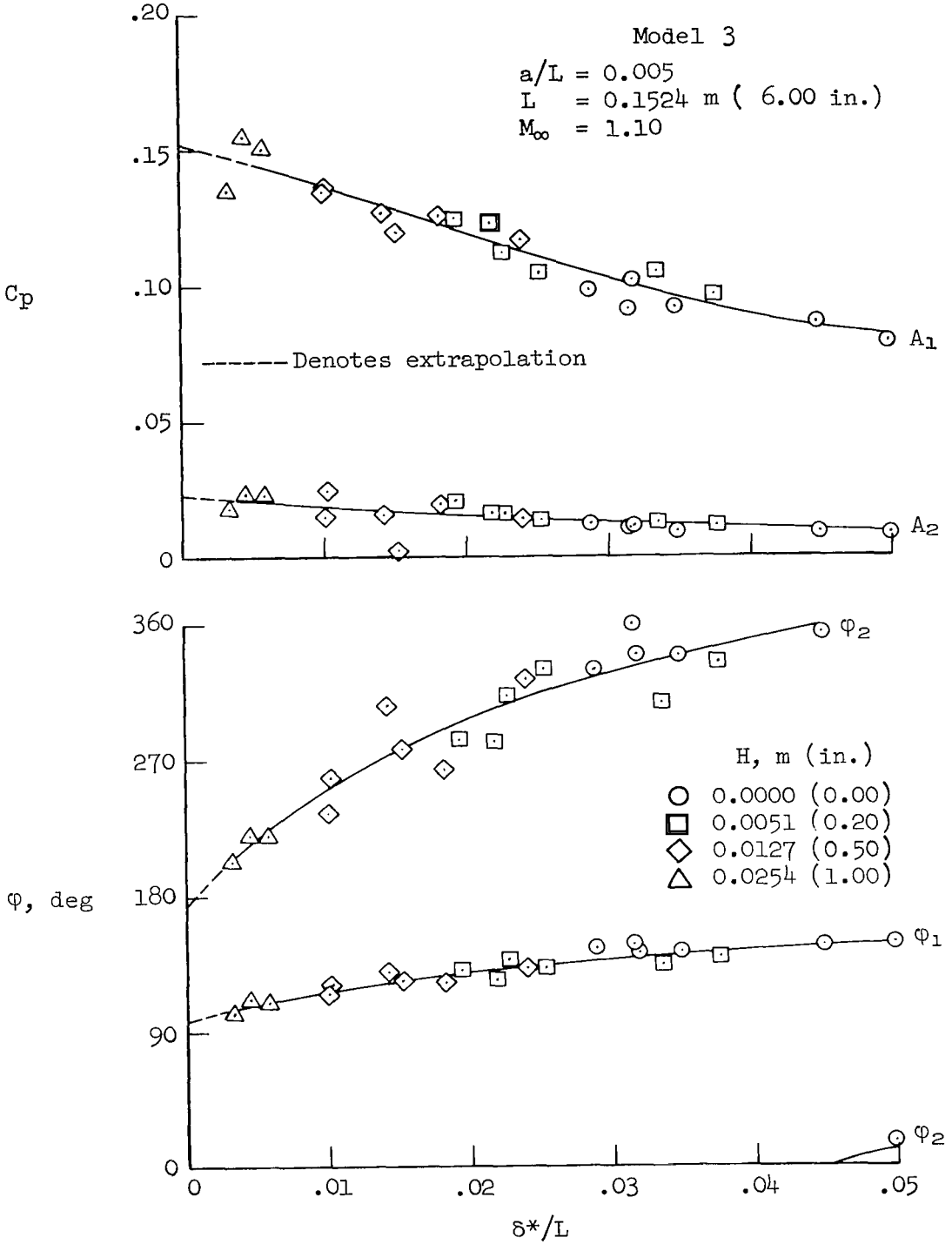

(d) $M_\infty = 1.10$

Figure 8.- Continued.

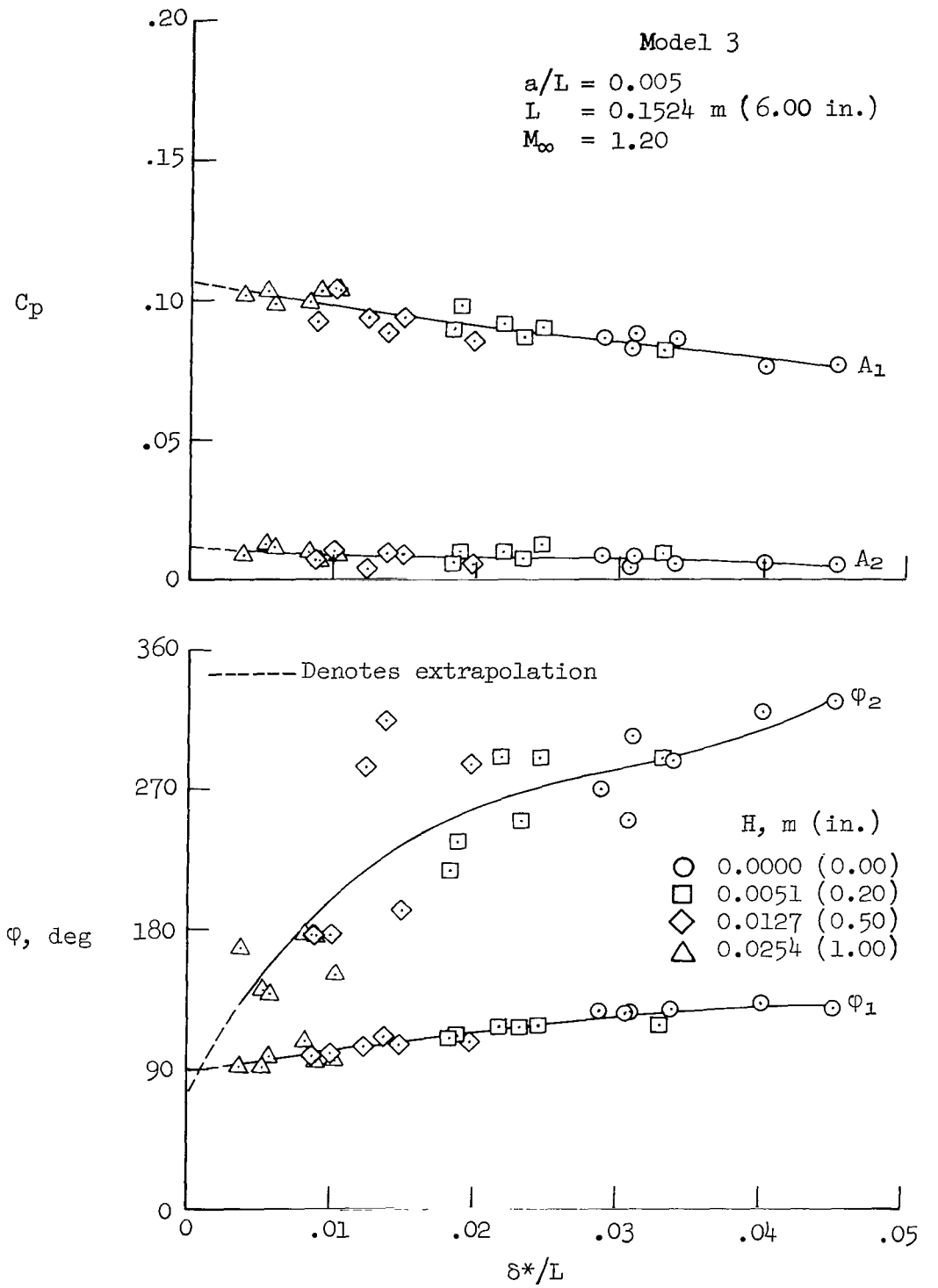

(e) $M_\infty = 1.20$

Figure 8.- Continued.

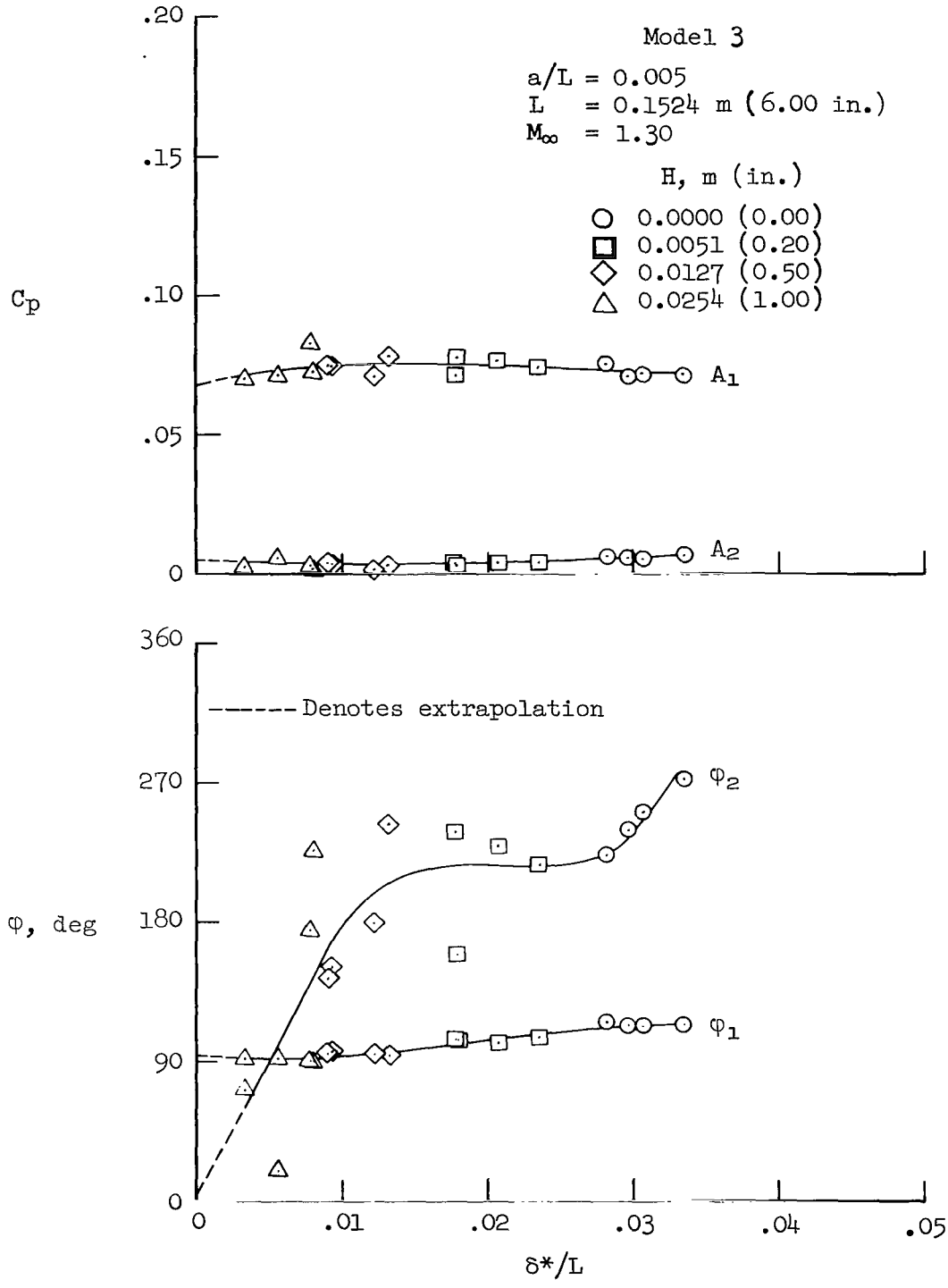

(f) $M_\infty = 1.30$

Figure 8.- Continued.

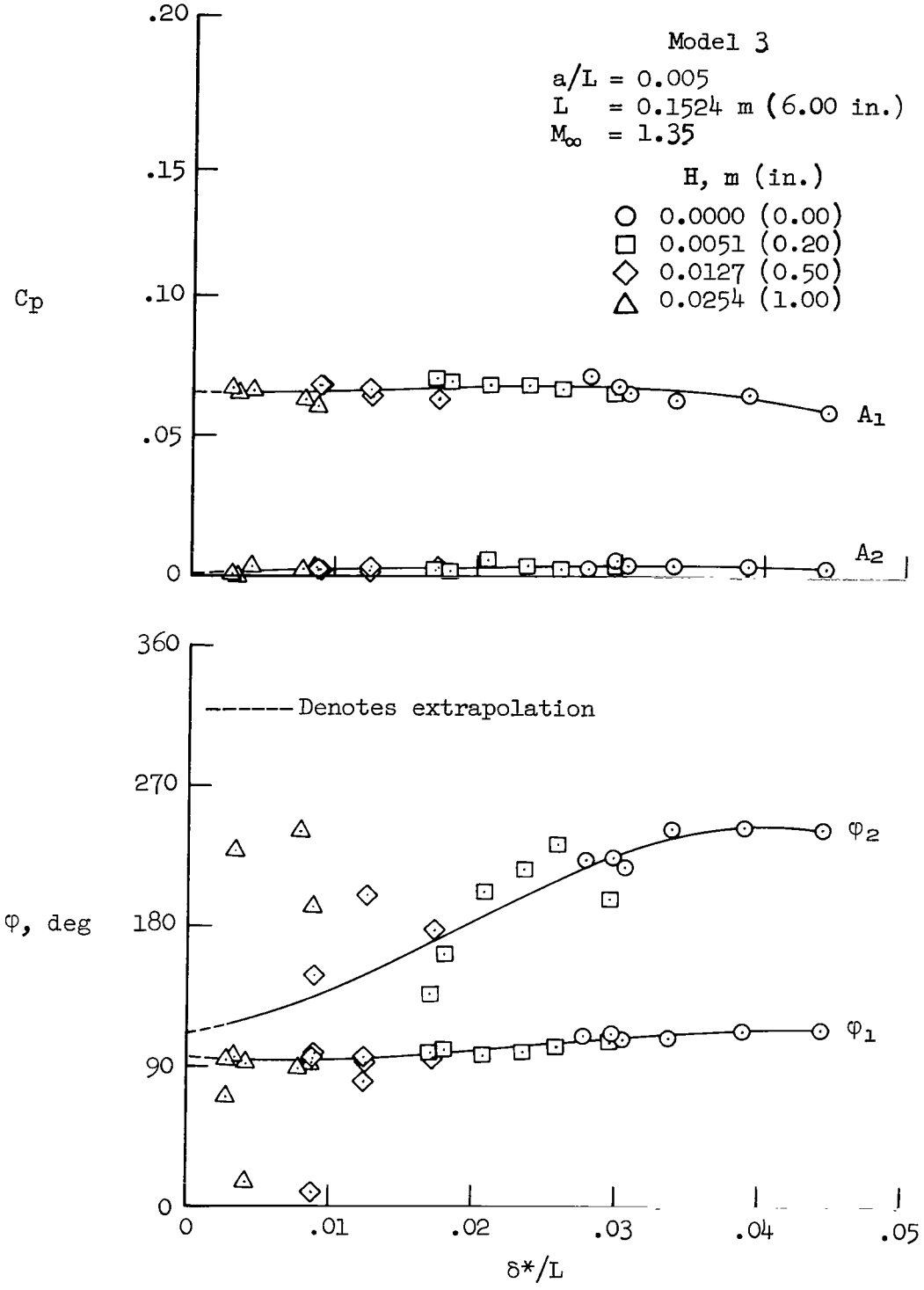

(g) $M_\infty = 1.35$

Figure 8.- Concluded.

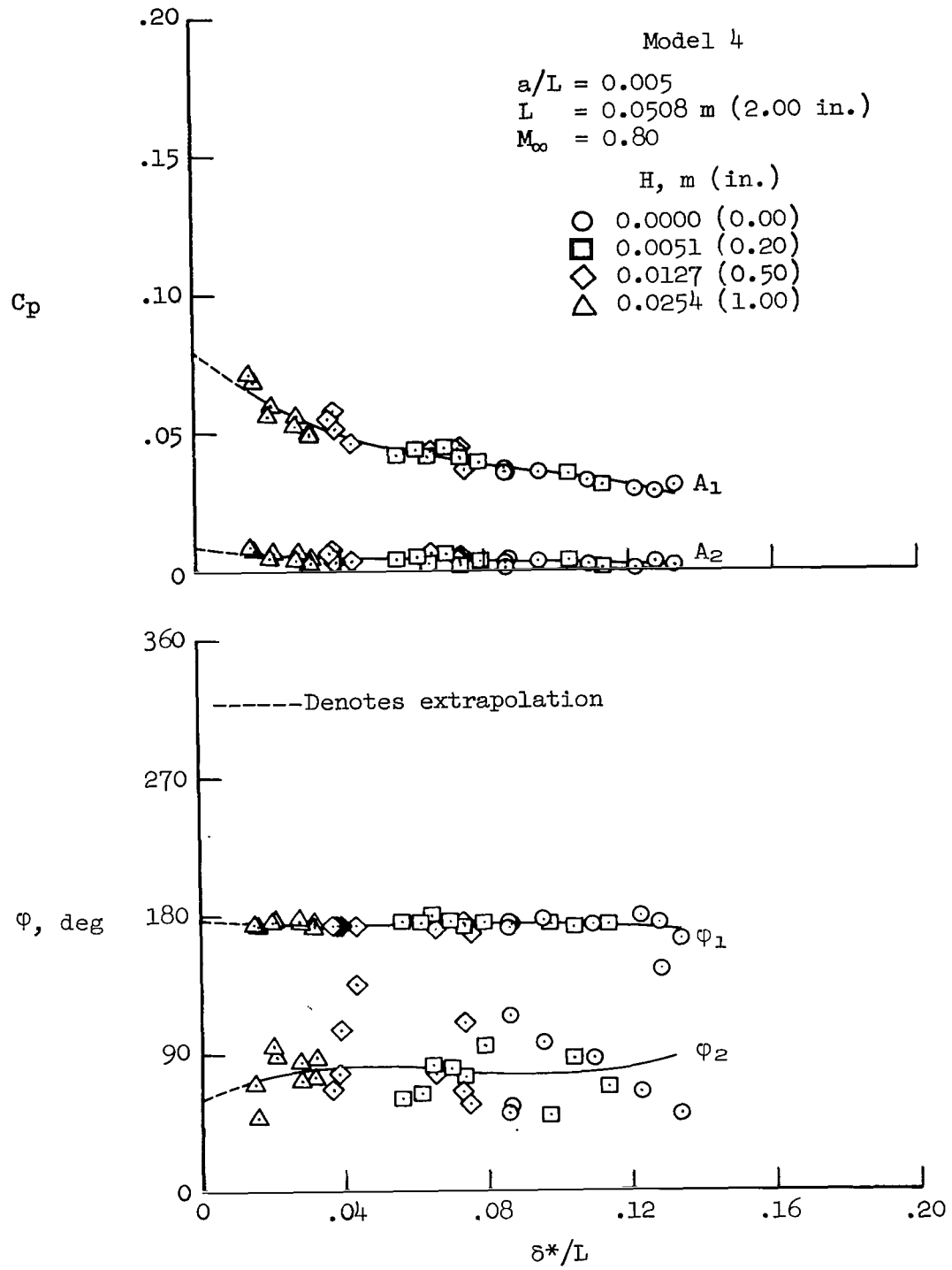

(a) $M_\infty = 0.80$

Figure 9.- Fourier components of the pressure coefficient on wavy-wall model 4 as a function of the dimensionless boundary-layer displacement thickness; a/L = 0.005, L = 0.05080 m (2.00 in.).

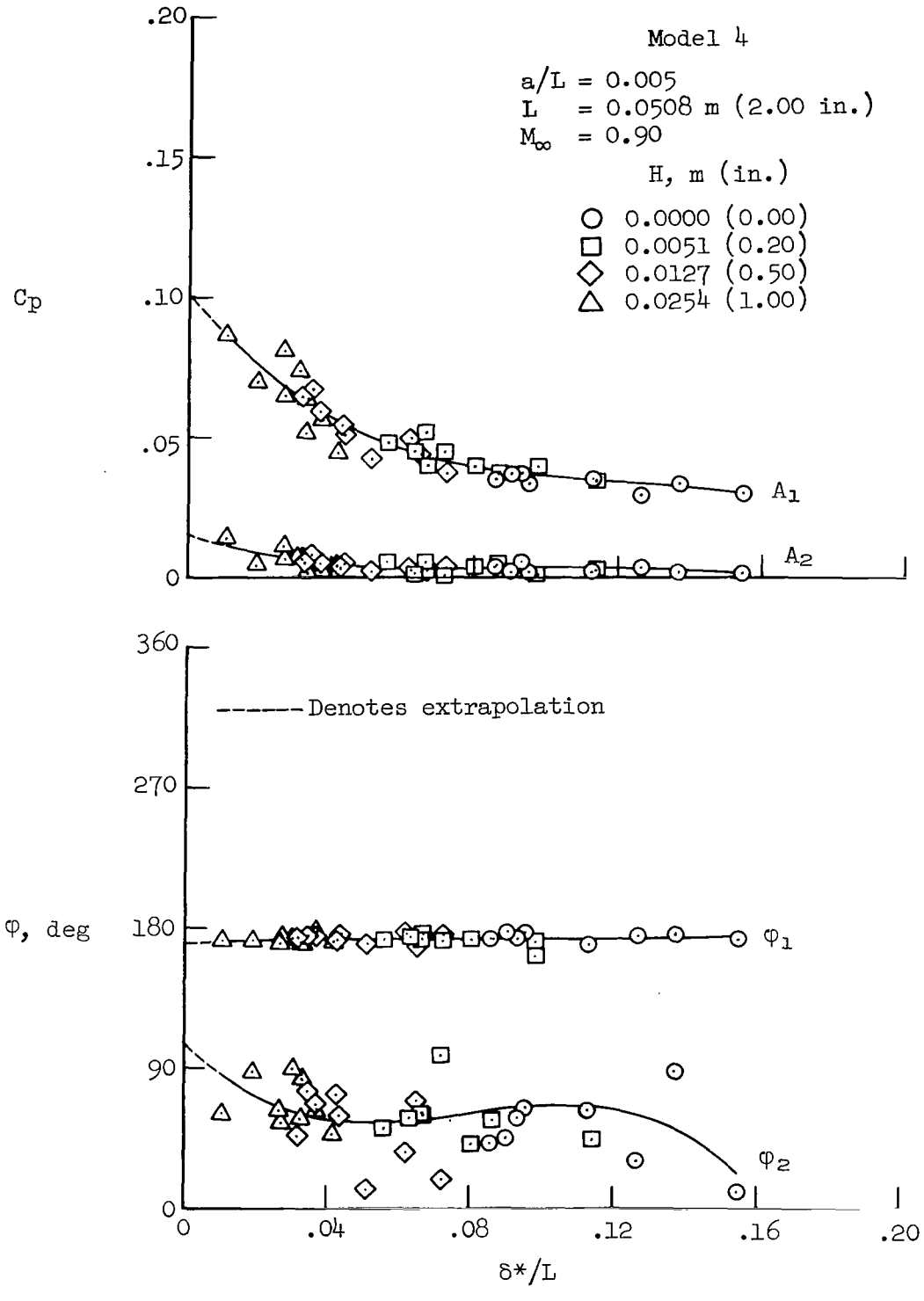

(b) M_∞ = 0.90

Figure 9.- Continued.

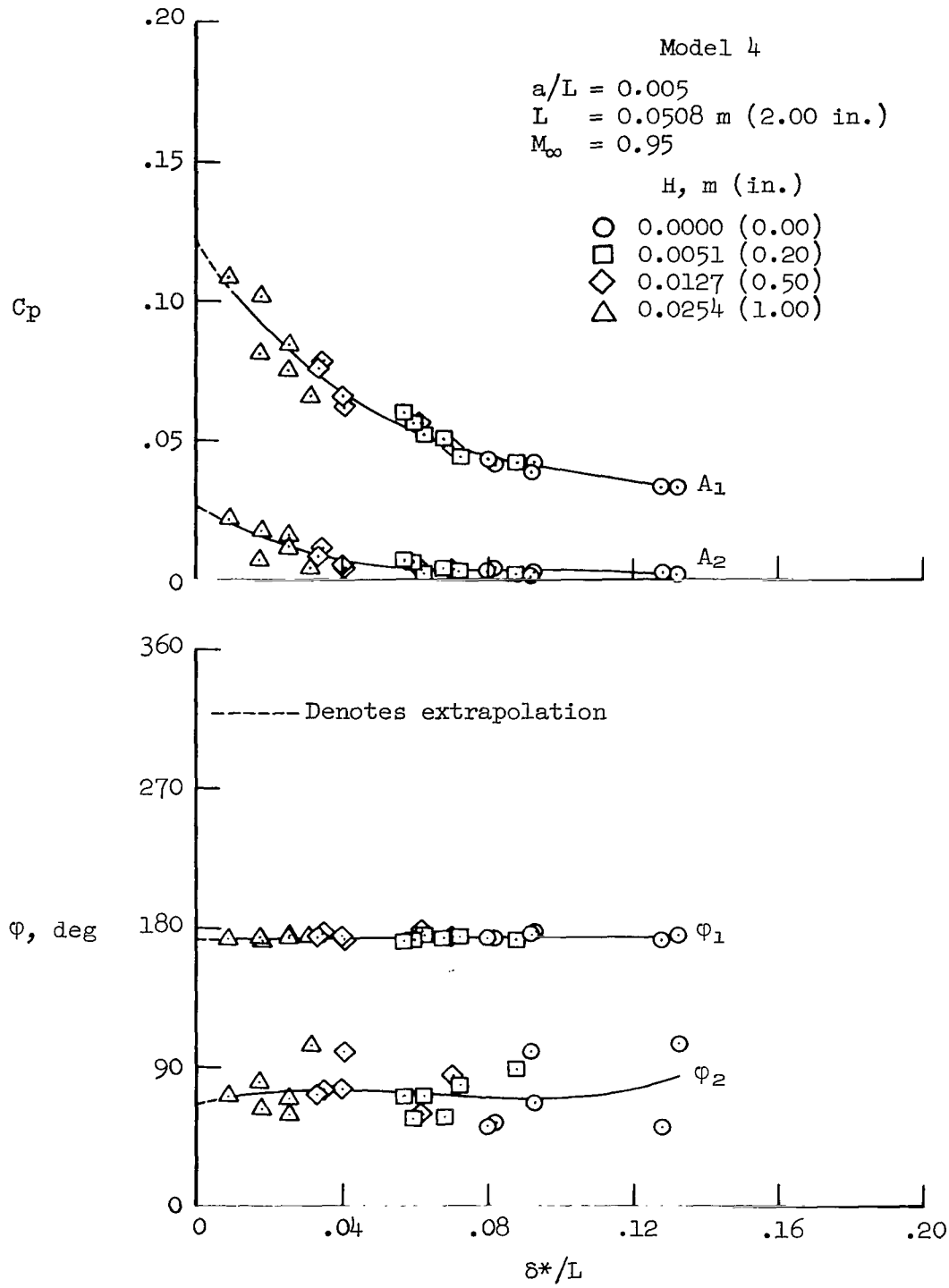

(c) M_∞ = 0.95

Figure 9.- Continued.

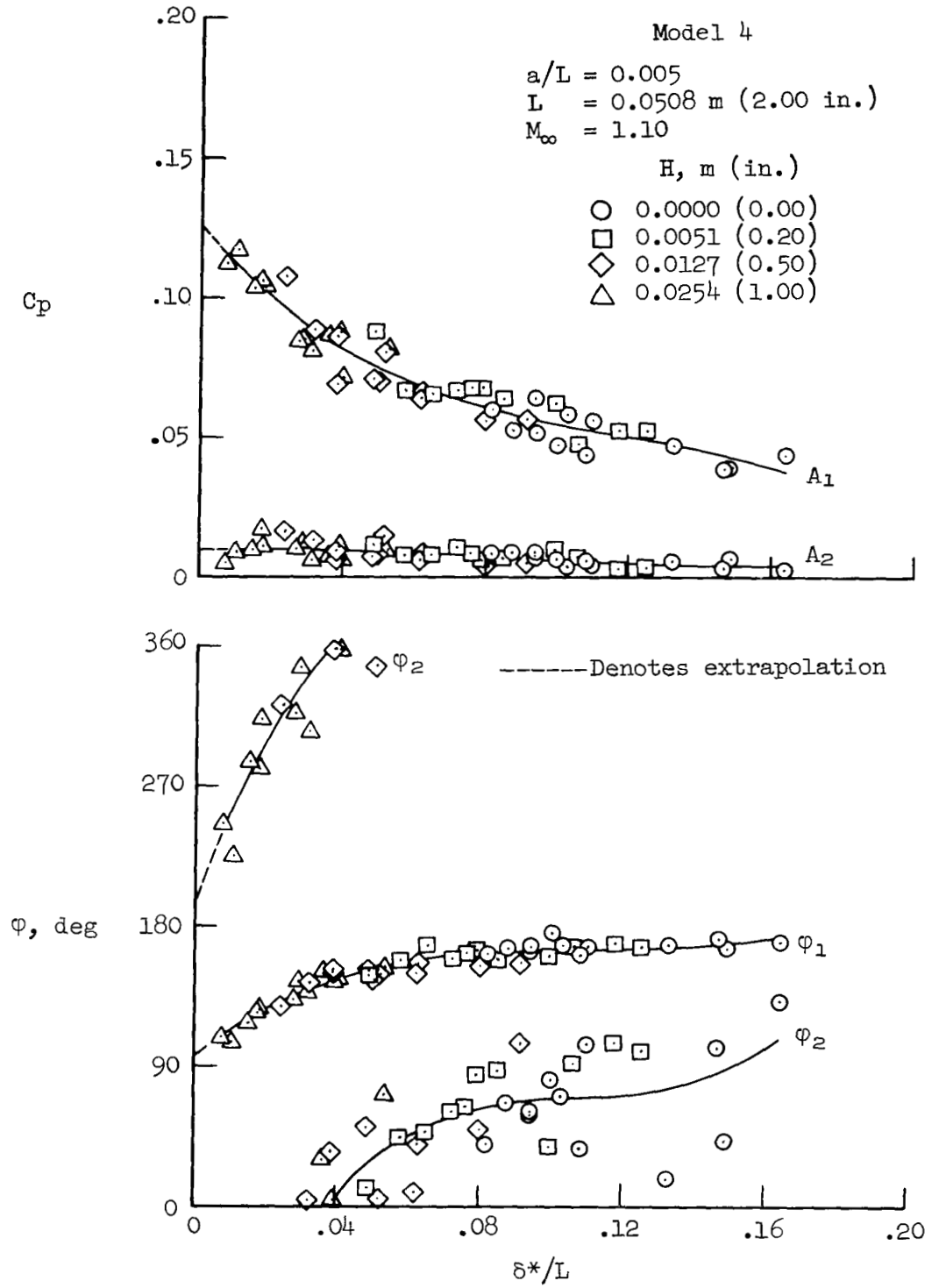

(d) $M_\infty = 1.10$

Figure 9.- Continued.

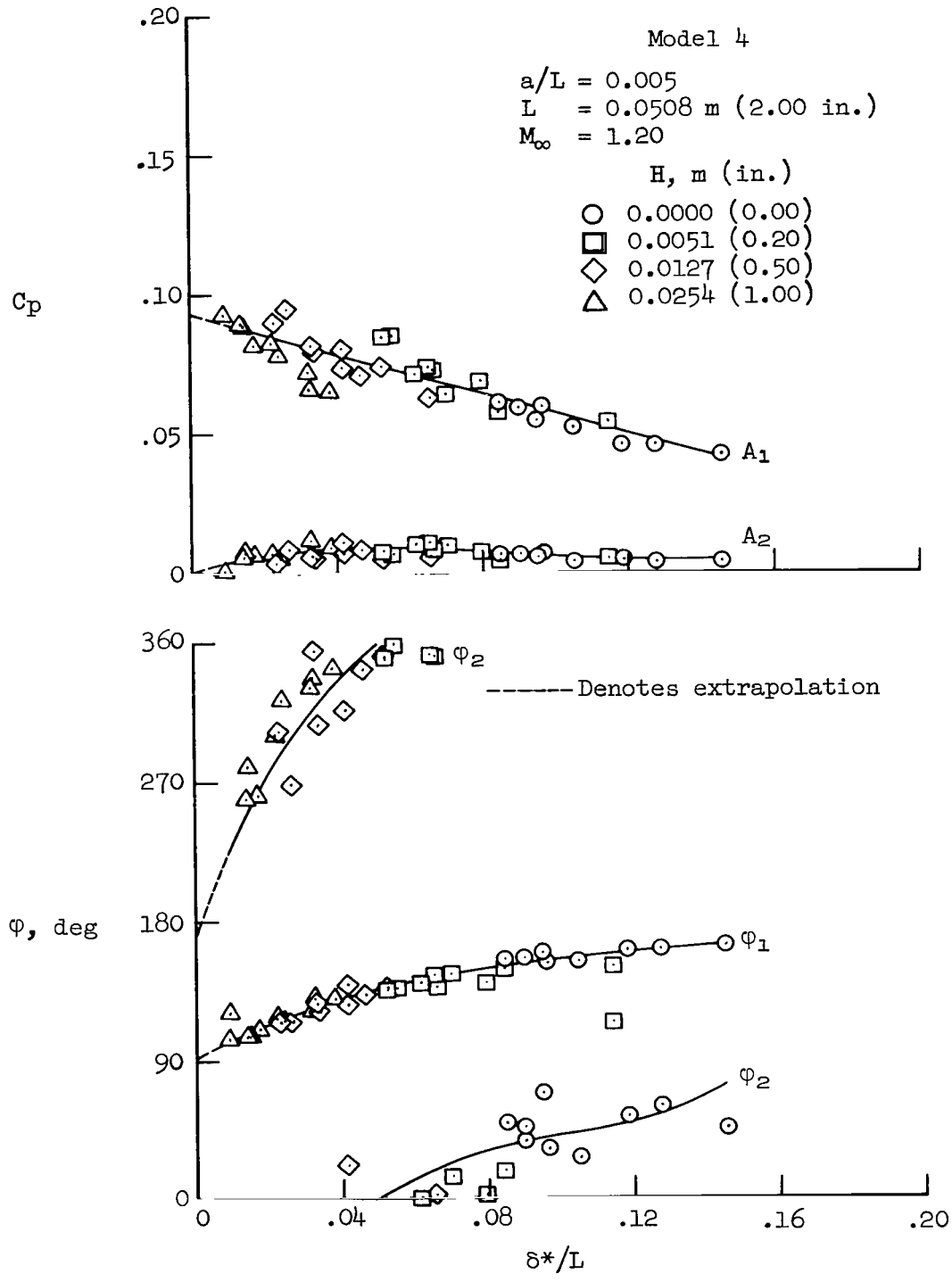

(e) M_∞ = 1.20

Figure 9.- Continued.

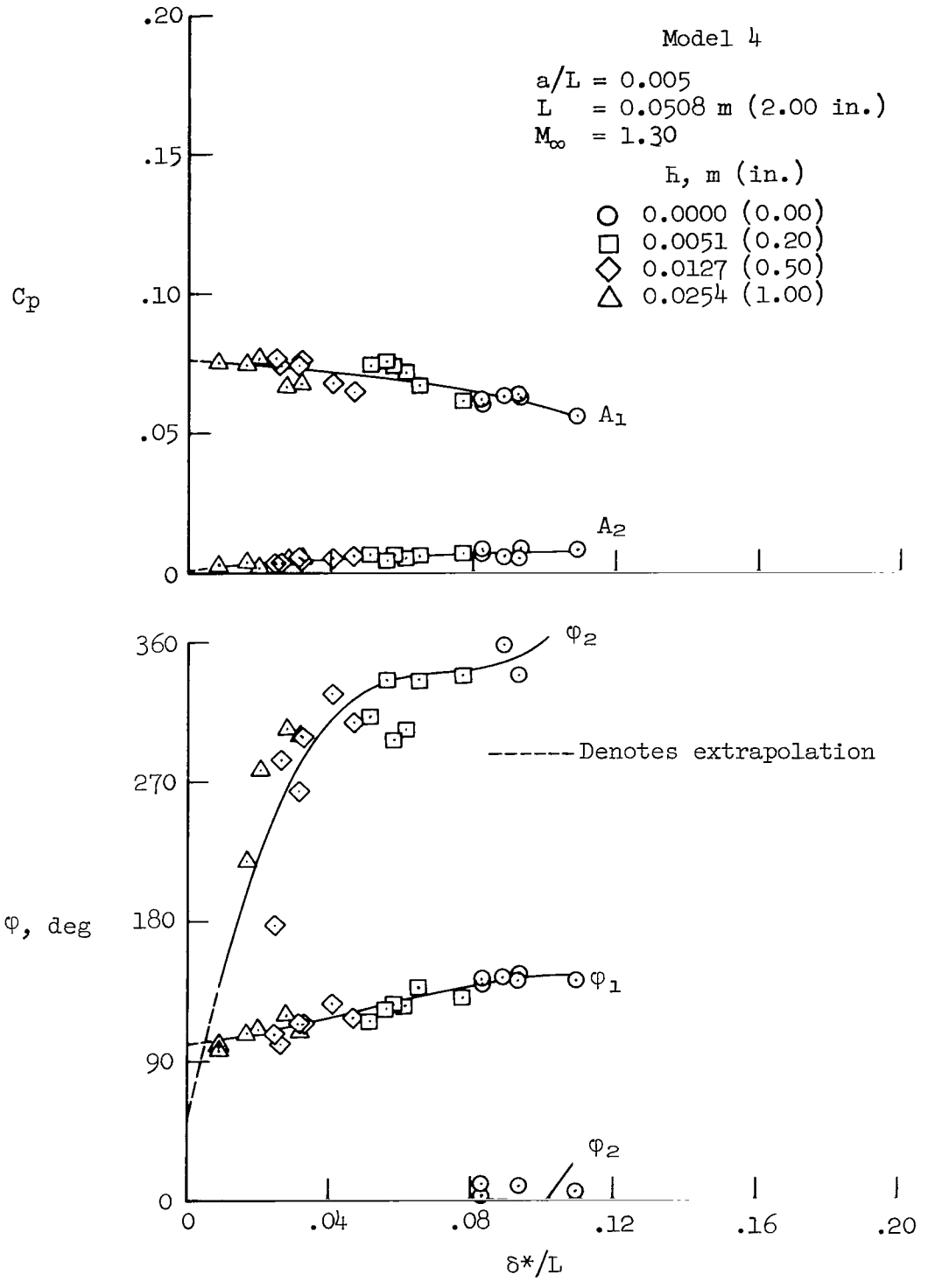

(f) $M_\infty = 1.30$

Figure 9.- Continued.

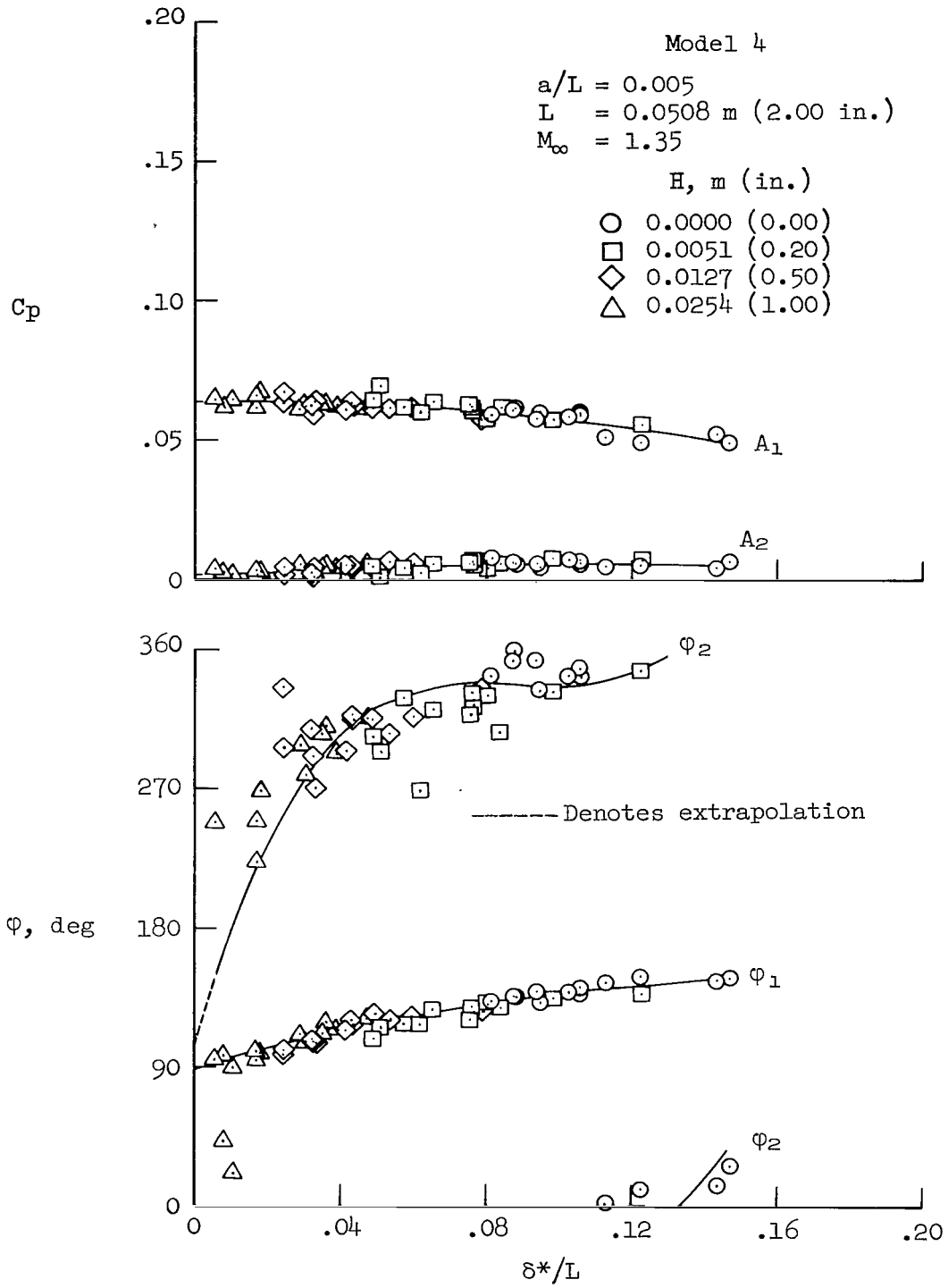

(g) $M_\infty = 1.35$

Figure 9.- Concluded.

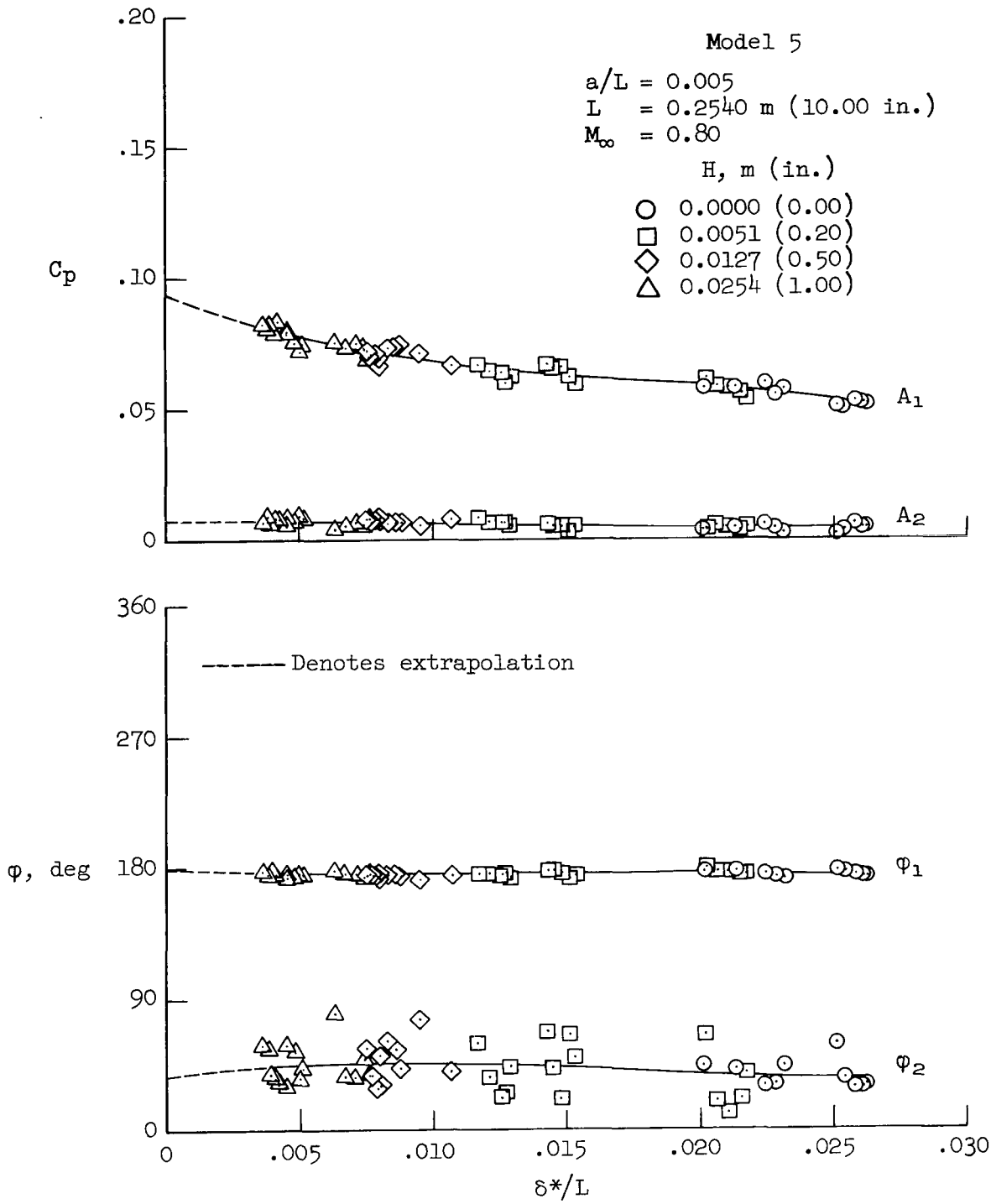

(a) M_∞ = 0.80

Figure 10.- Fourier components of the pressure coefficient on wavy-wall model 5 as a function of the dimensionless boundary-layer displacement thickness; a/L = 0.005, L = 0.25400 m (10.00 in.).

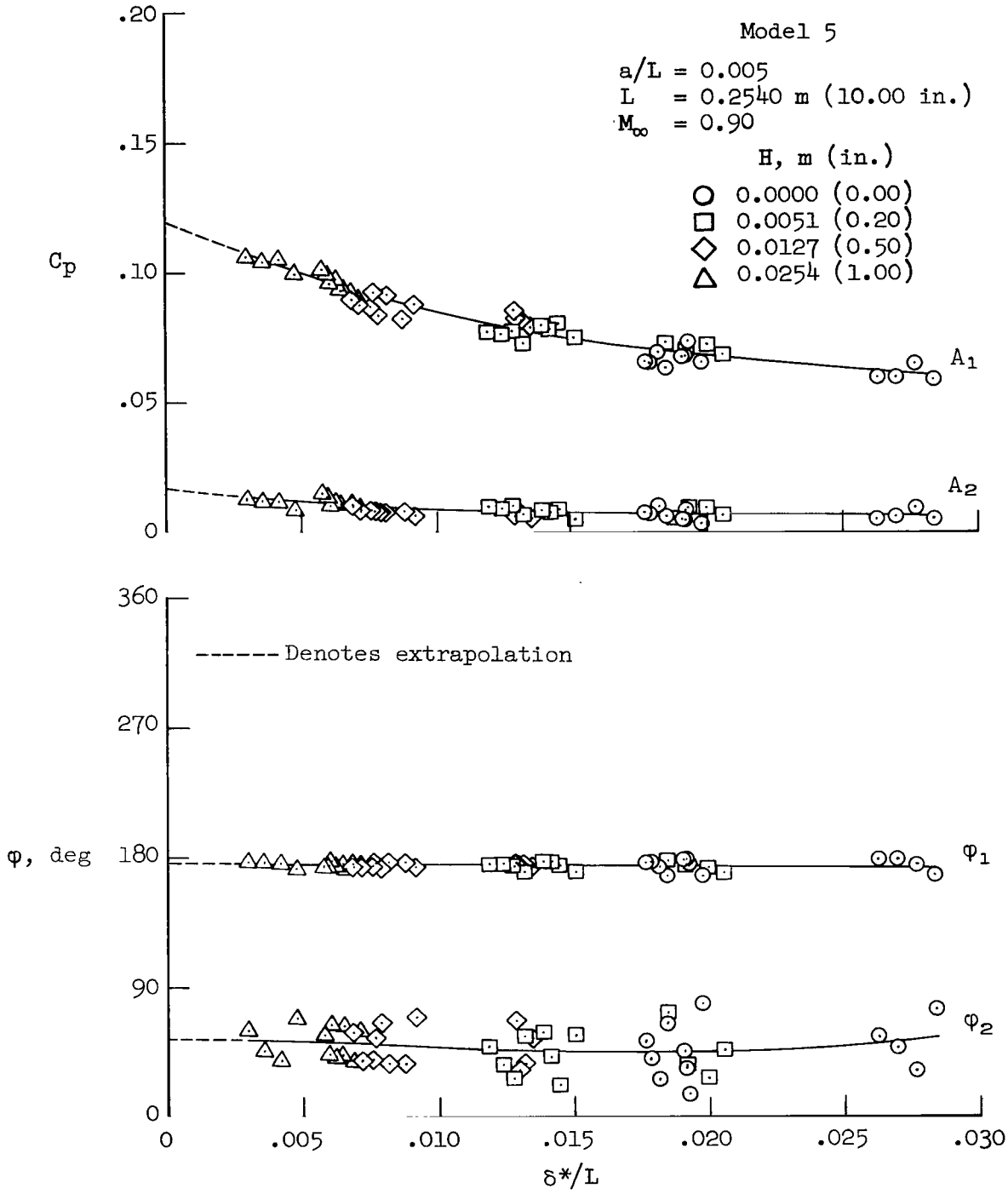

(b) $M_\infty = 0.90$

Figure 10.- Continued.

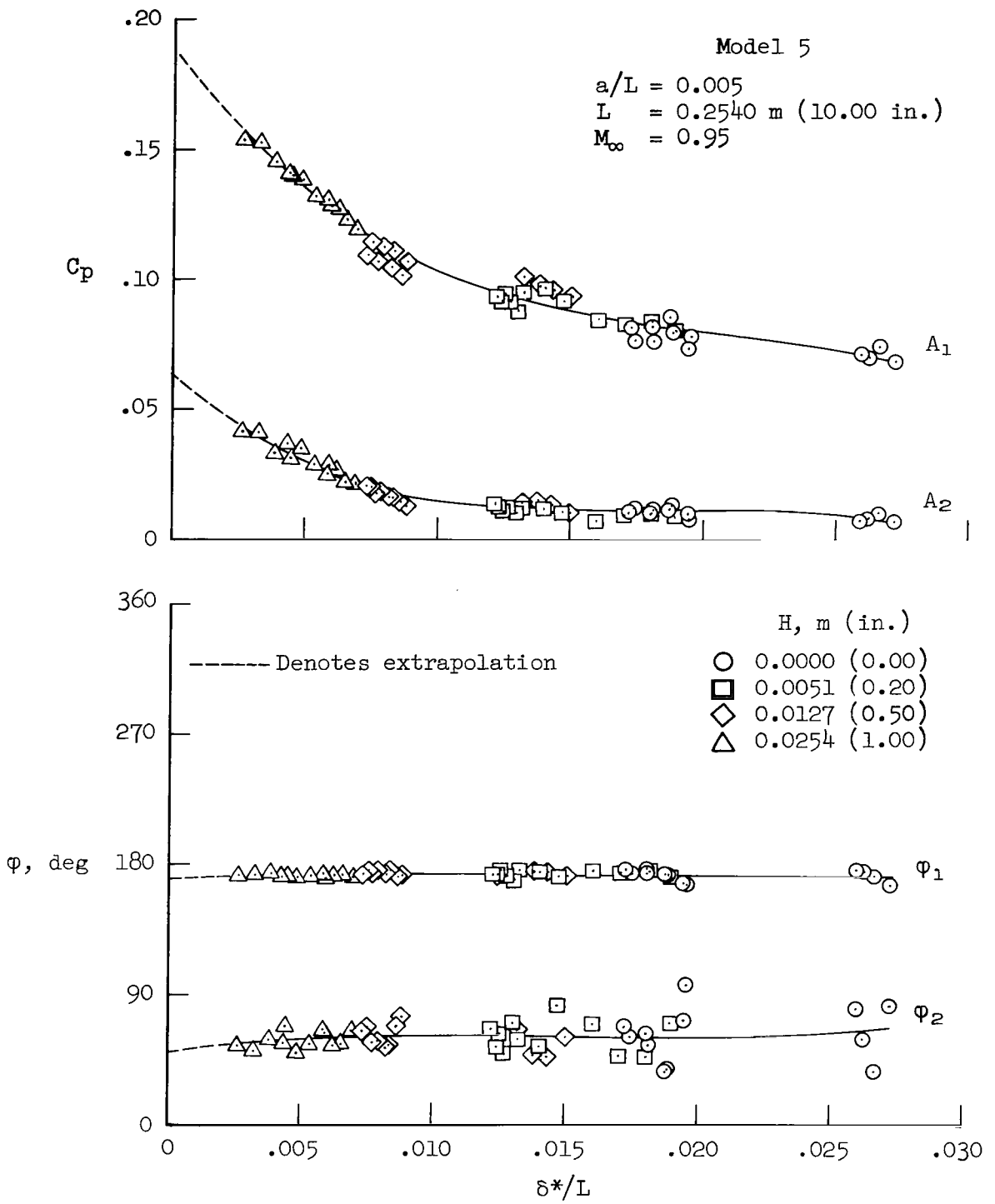

(c) M_∞ = 0.95

Figure 10.- Continued.

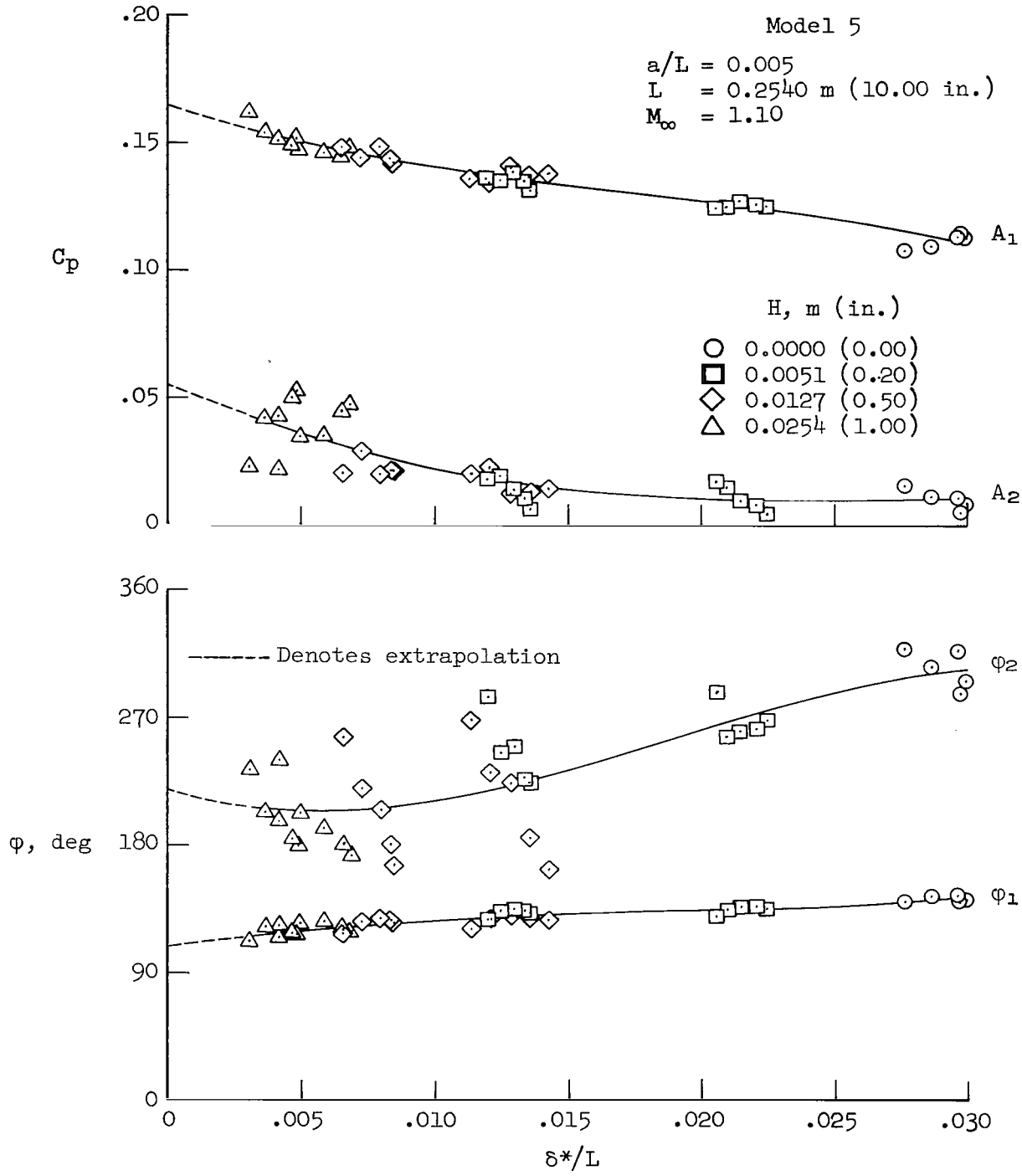

(d) $M_\infty = 1.10$

Figure 10.- Continued.

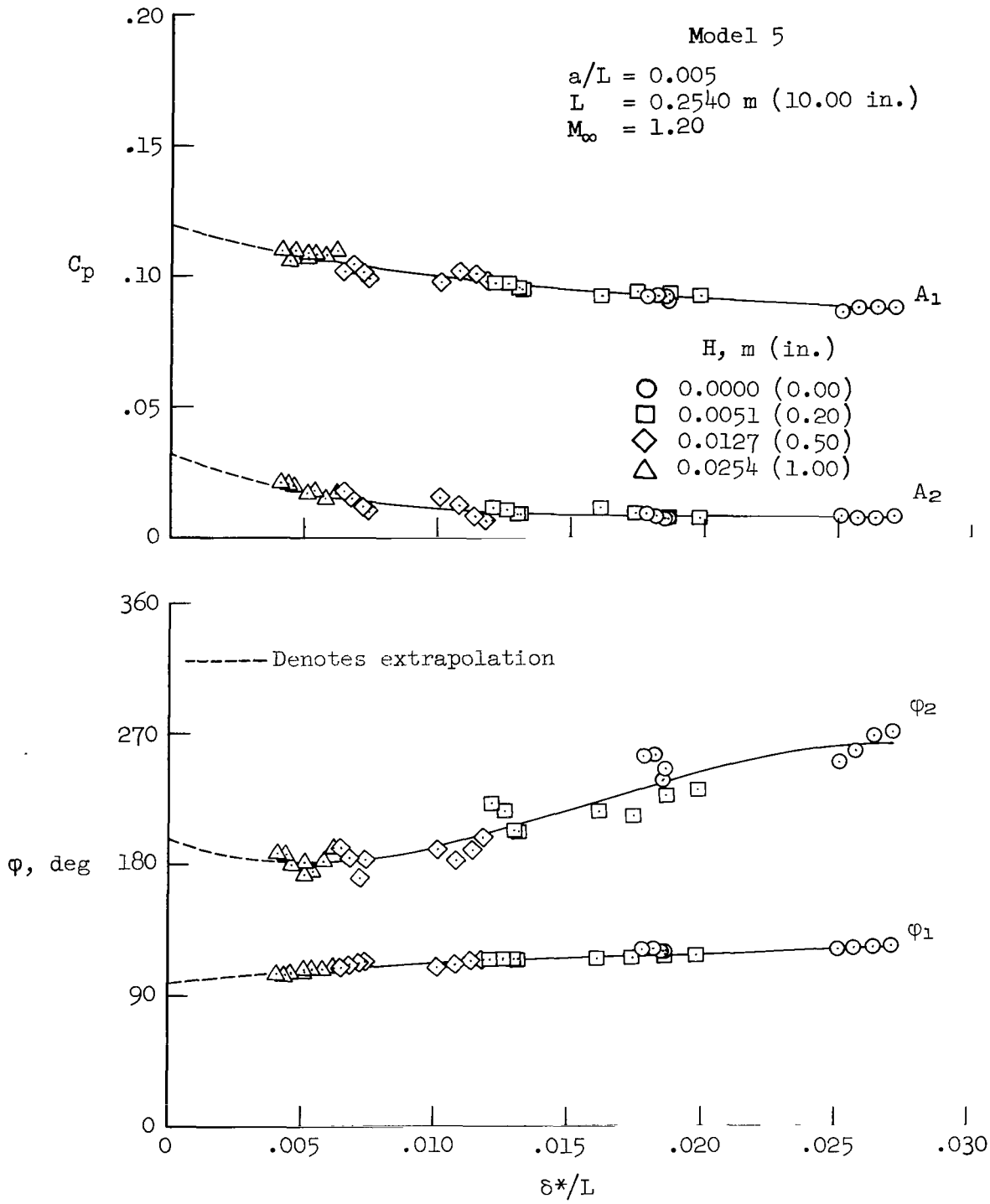

(e) $M_\infty = 1.20$

Figure 10.- Continued.

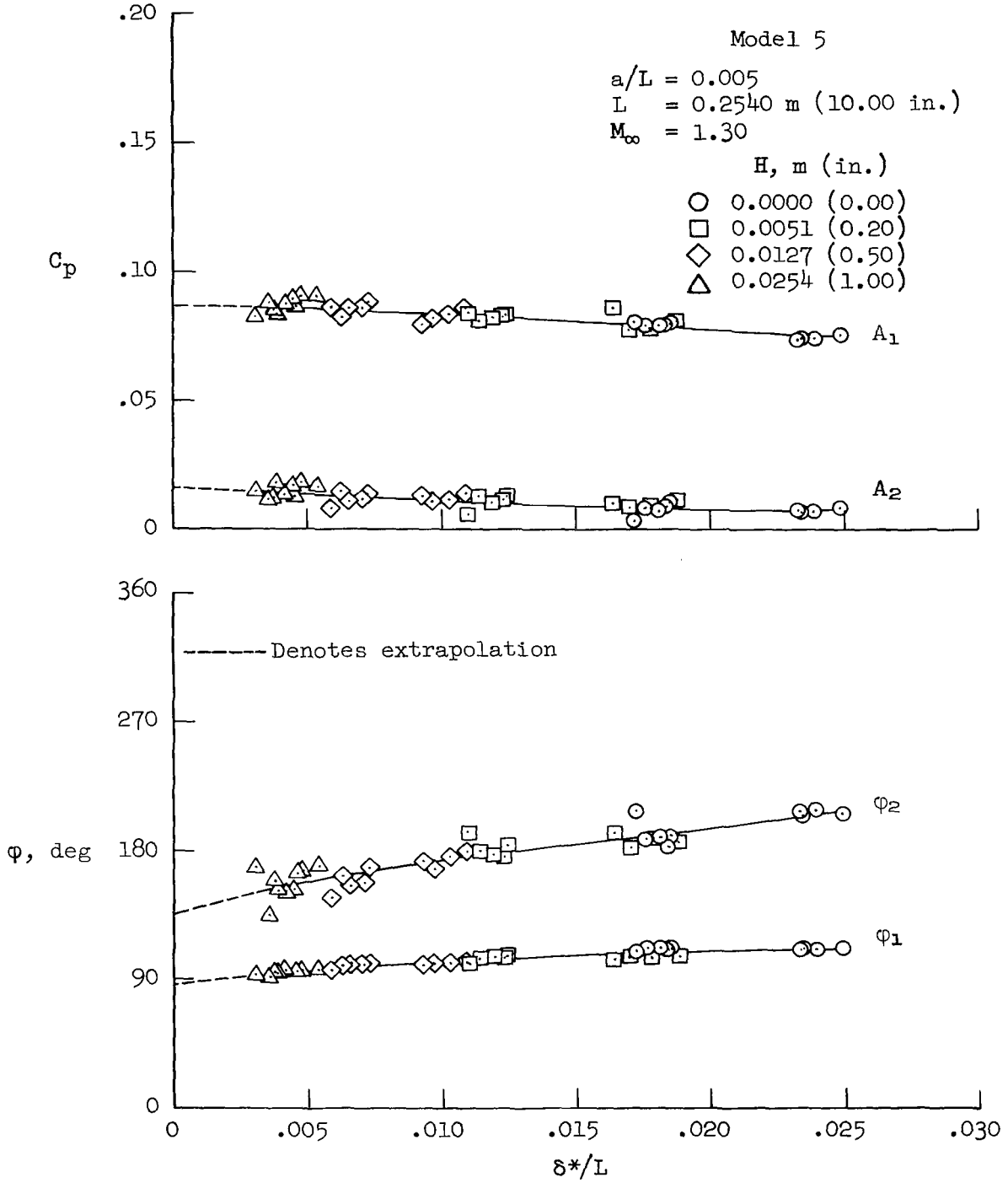

(f) M_∞ = 1.30

Figure 10.- Continued.

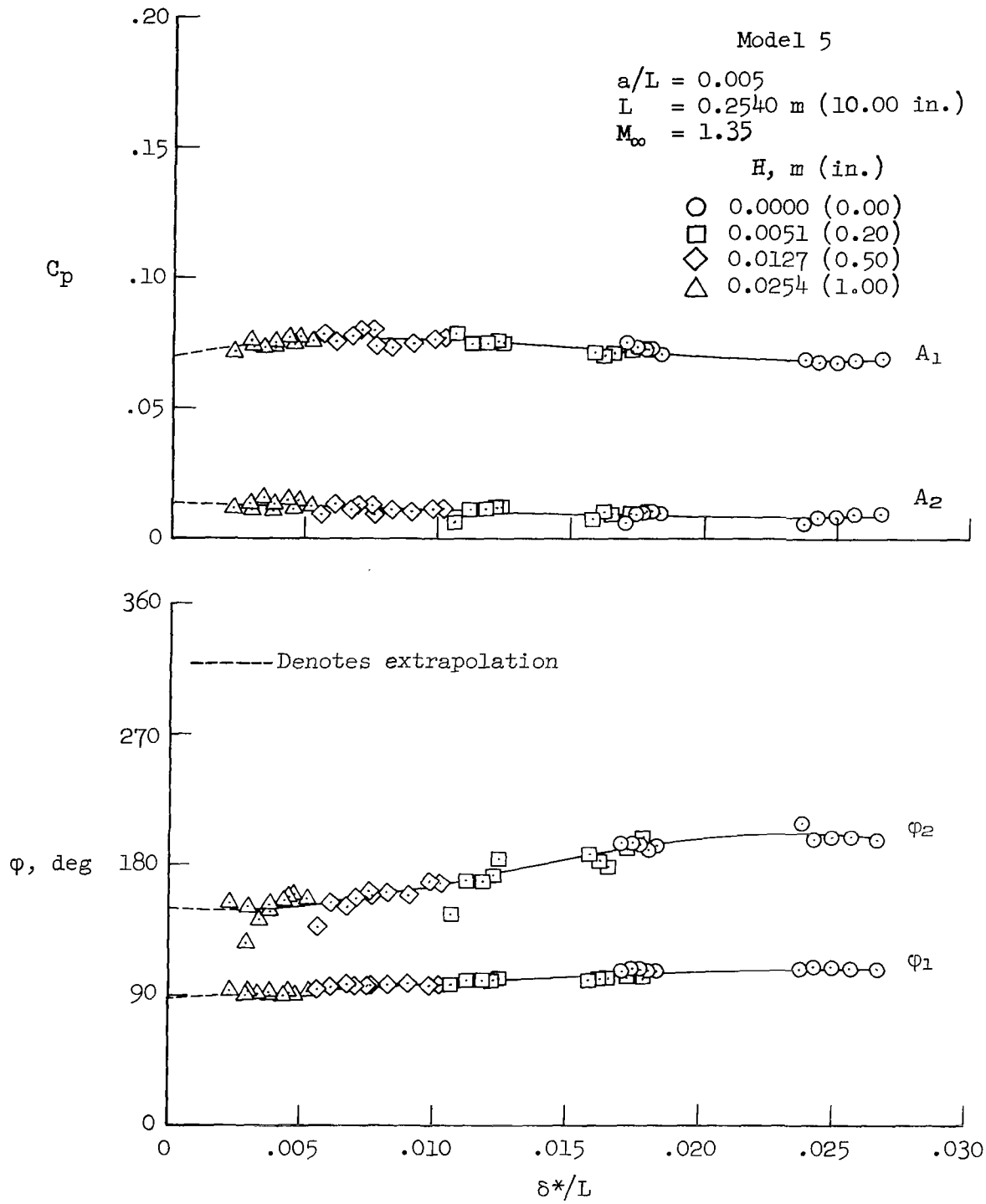

(g) M_∞ = 1.35

Figure 10.- Concluded.

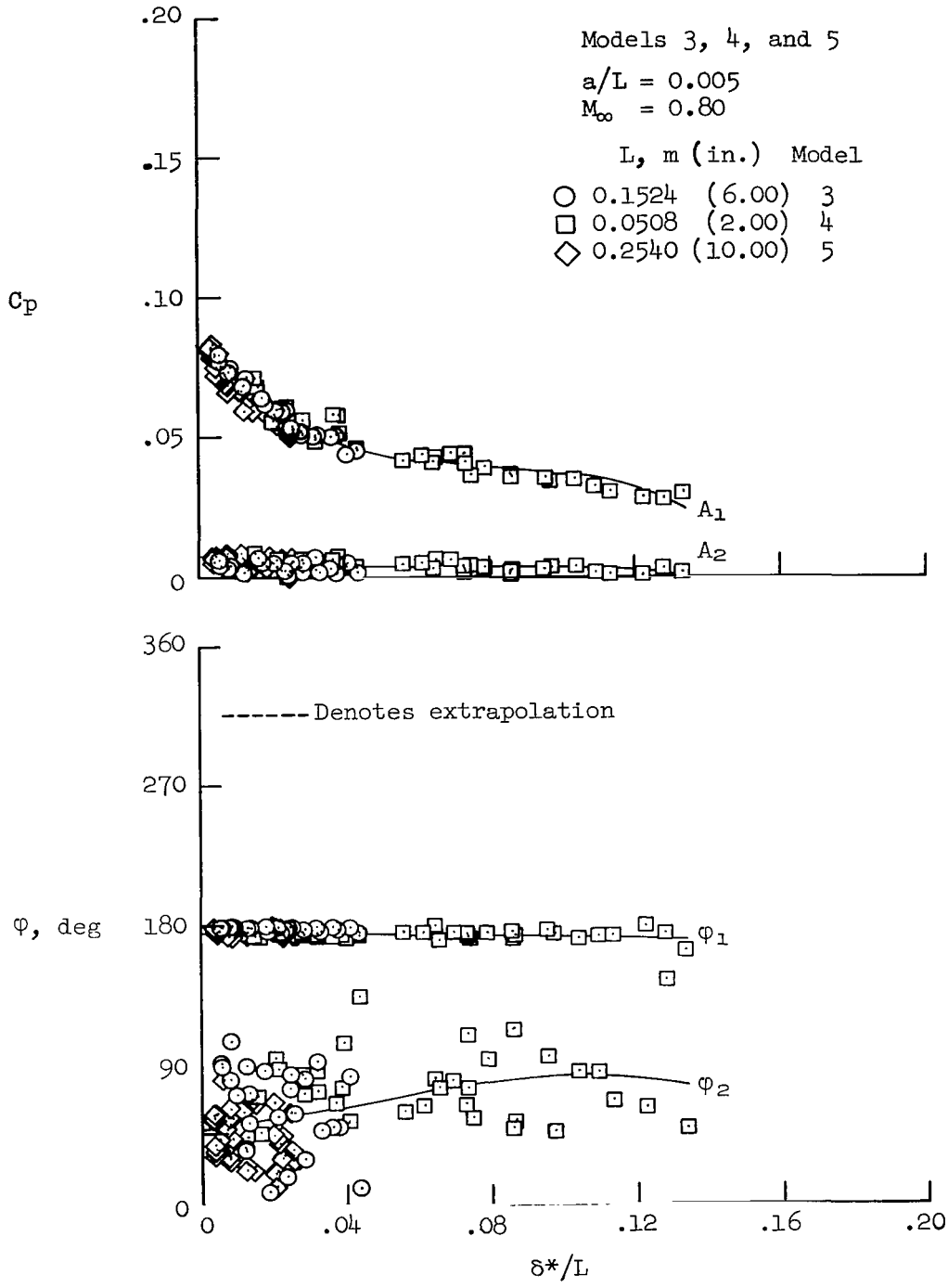

(a) M_∞ = 0.80

Figure 11.- Fourier components of the pressure coefficients on wavy-wall models 3, 4, and 5 as a function of the dimensionless boundary-layer displacement thickness; a/L = 0.005, L = 0.15240 m (6.00 in.), 0.05080 m (2.00 in.) and 0.25400 m (10.00 in.).

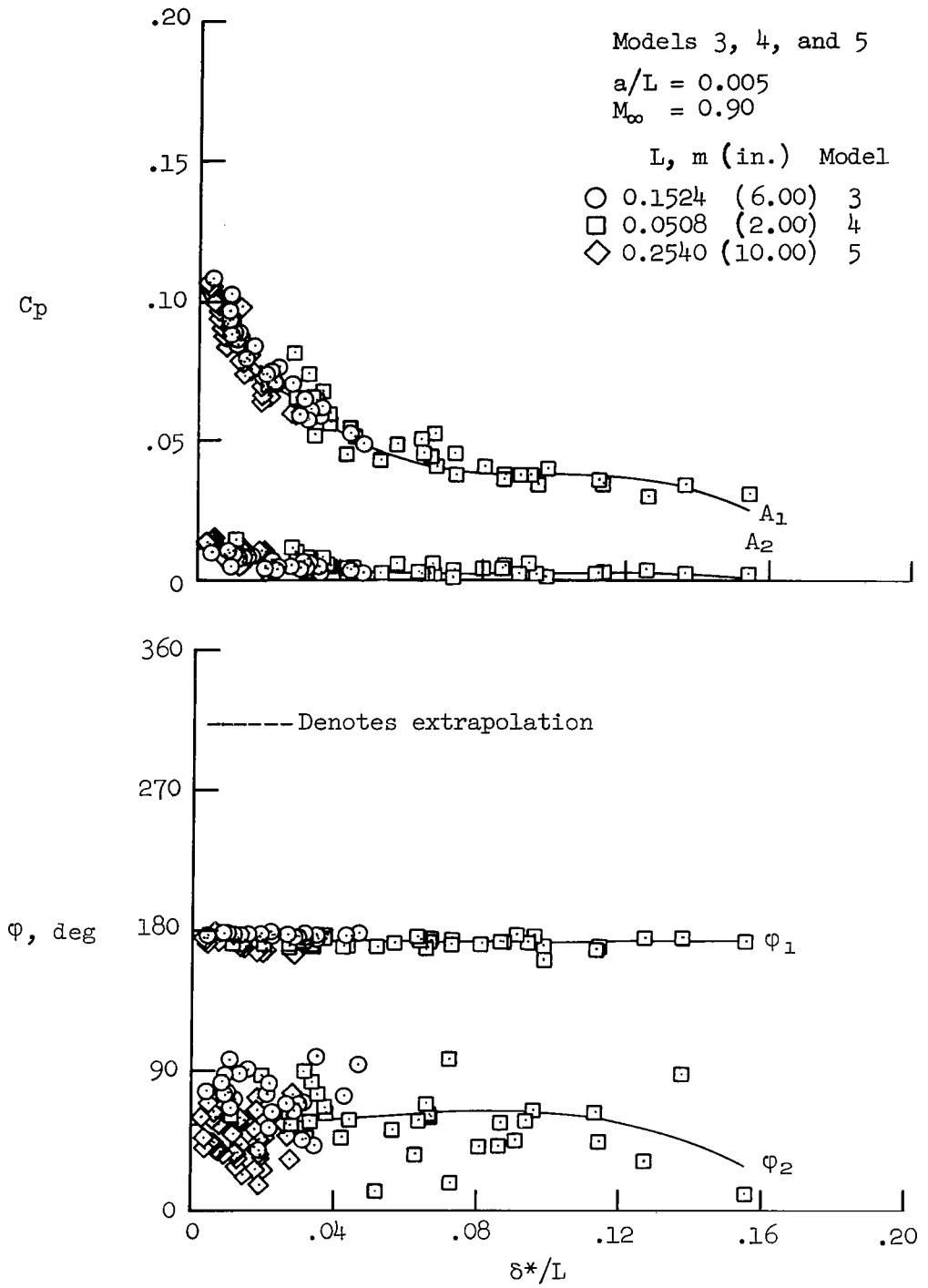

(b) M_∞ = 0.90

Figure 11.- Continued.

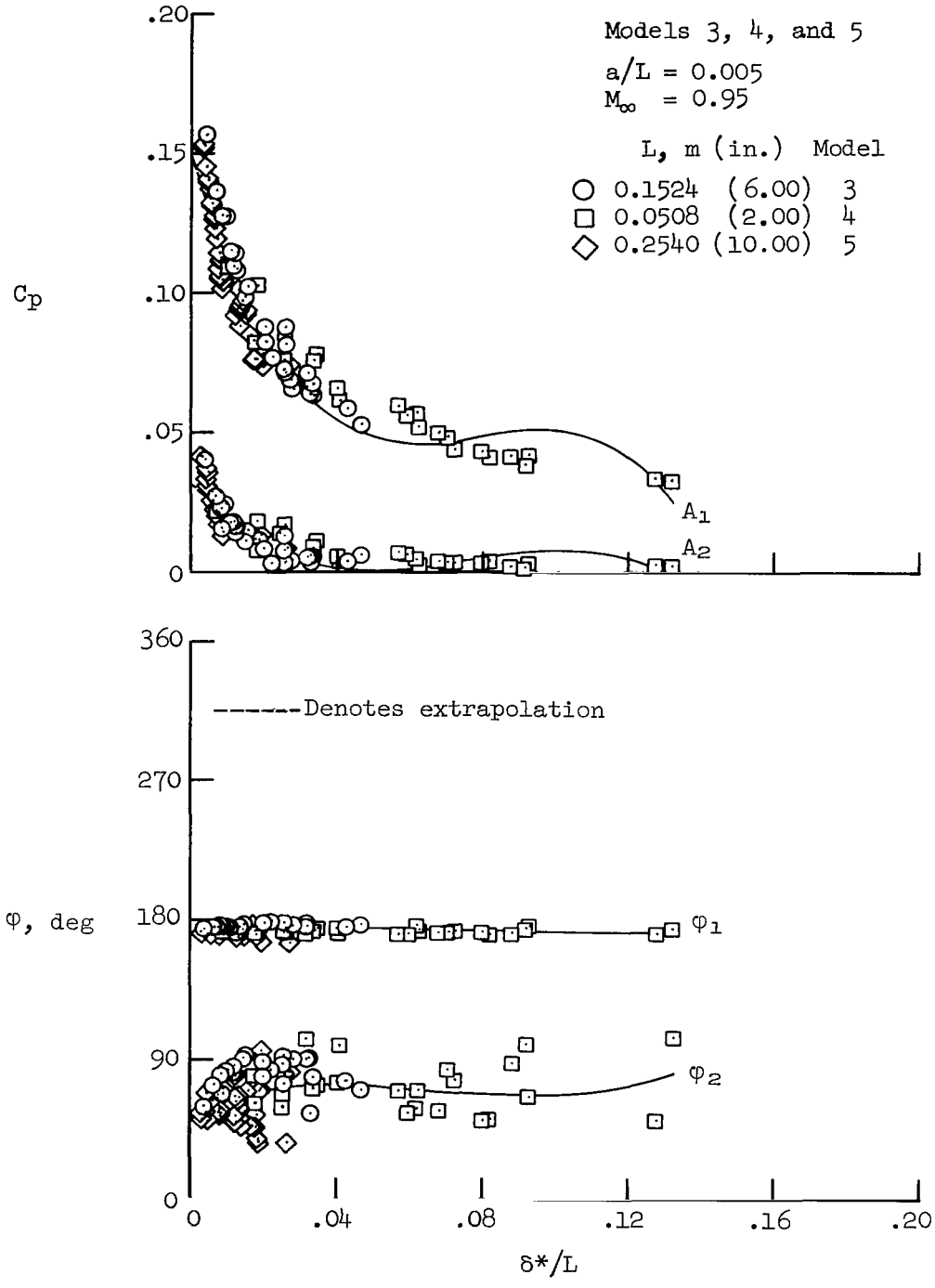

(c) M_∞ = 0.95

Figure 11.- Continued.

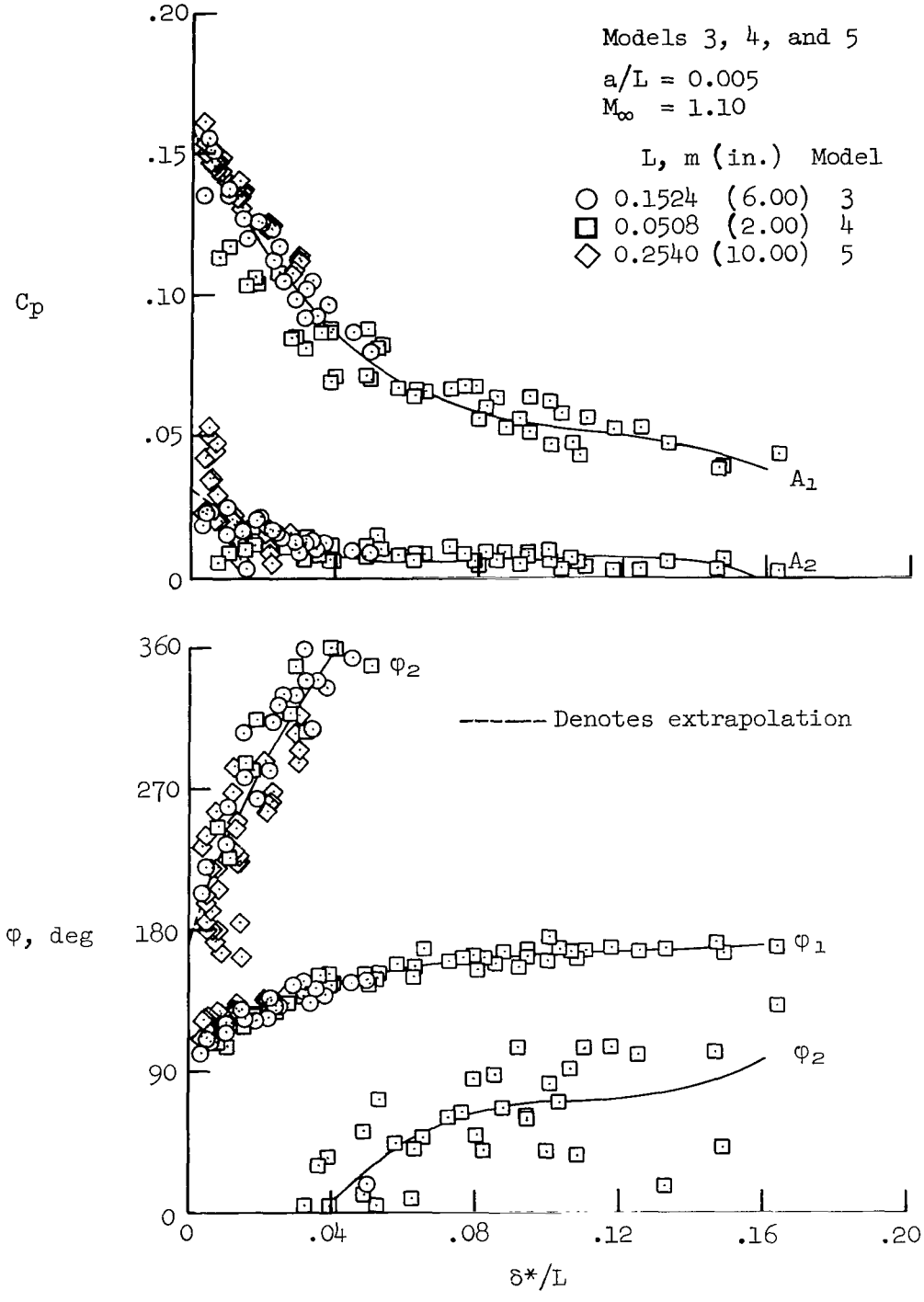

(d) M_∞ = 1.10

Figure 11.- Continued.

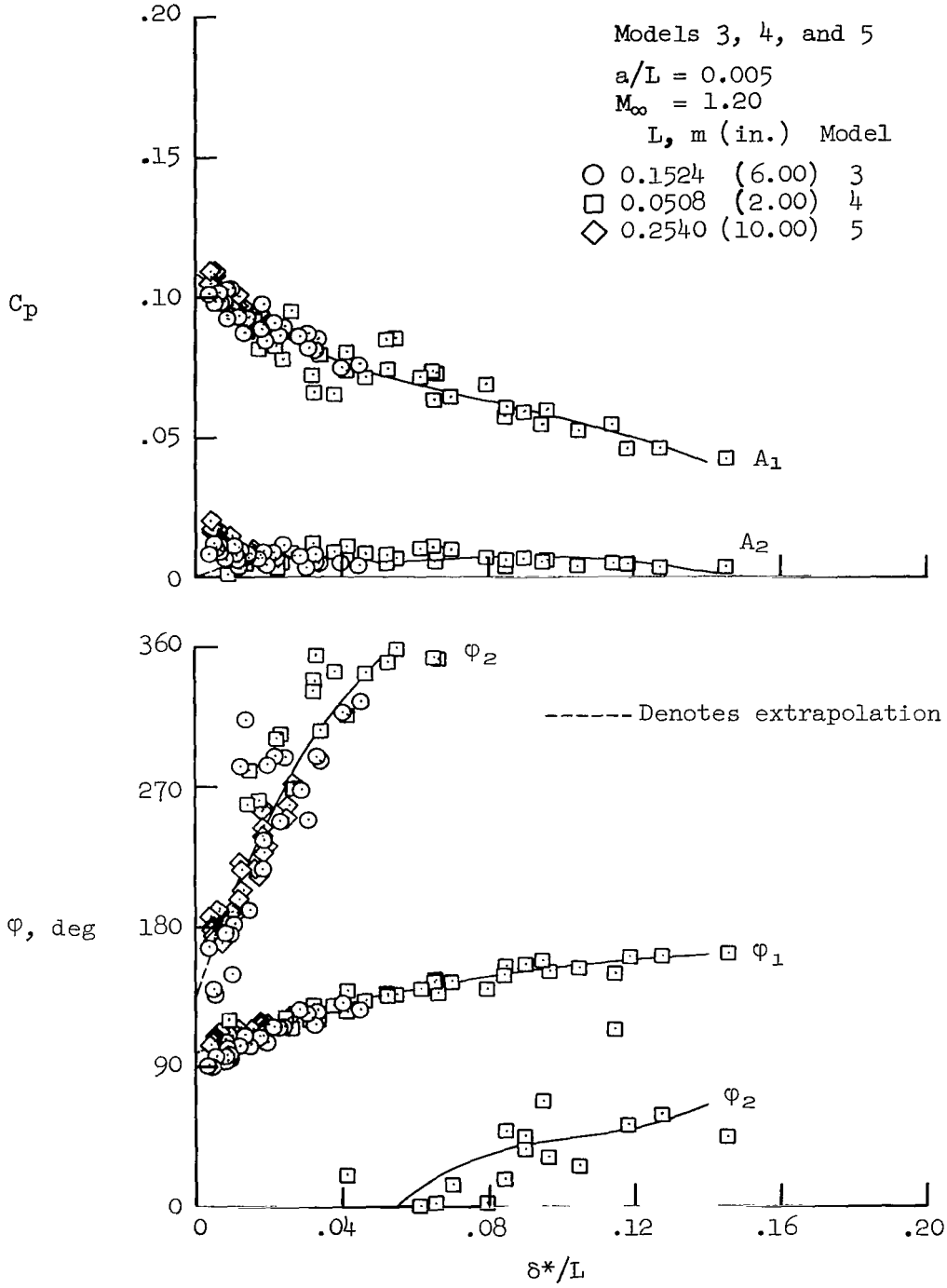

(e) M_∞ = 1.20

Figure 11.- Continued.

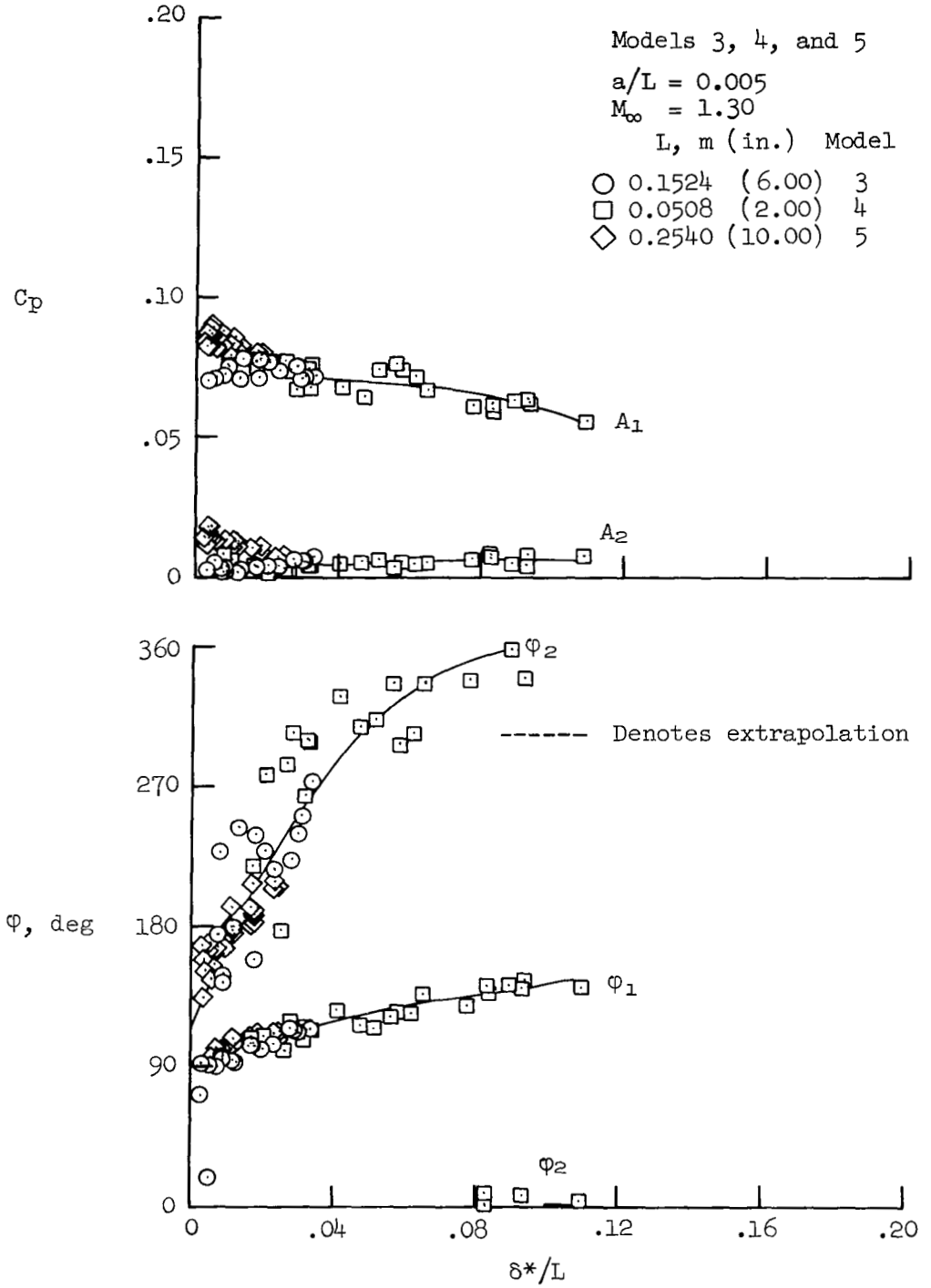

(f) M_∞ = 1.30

Figure 11.- Continued.

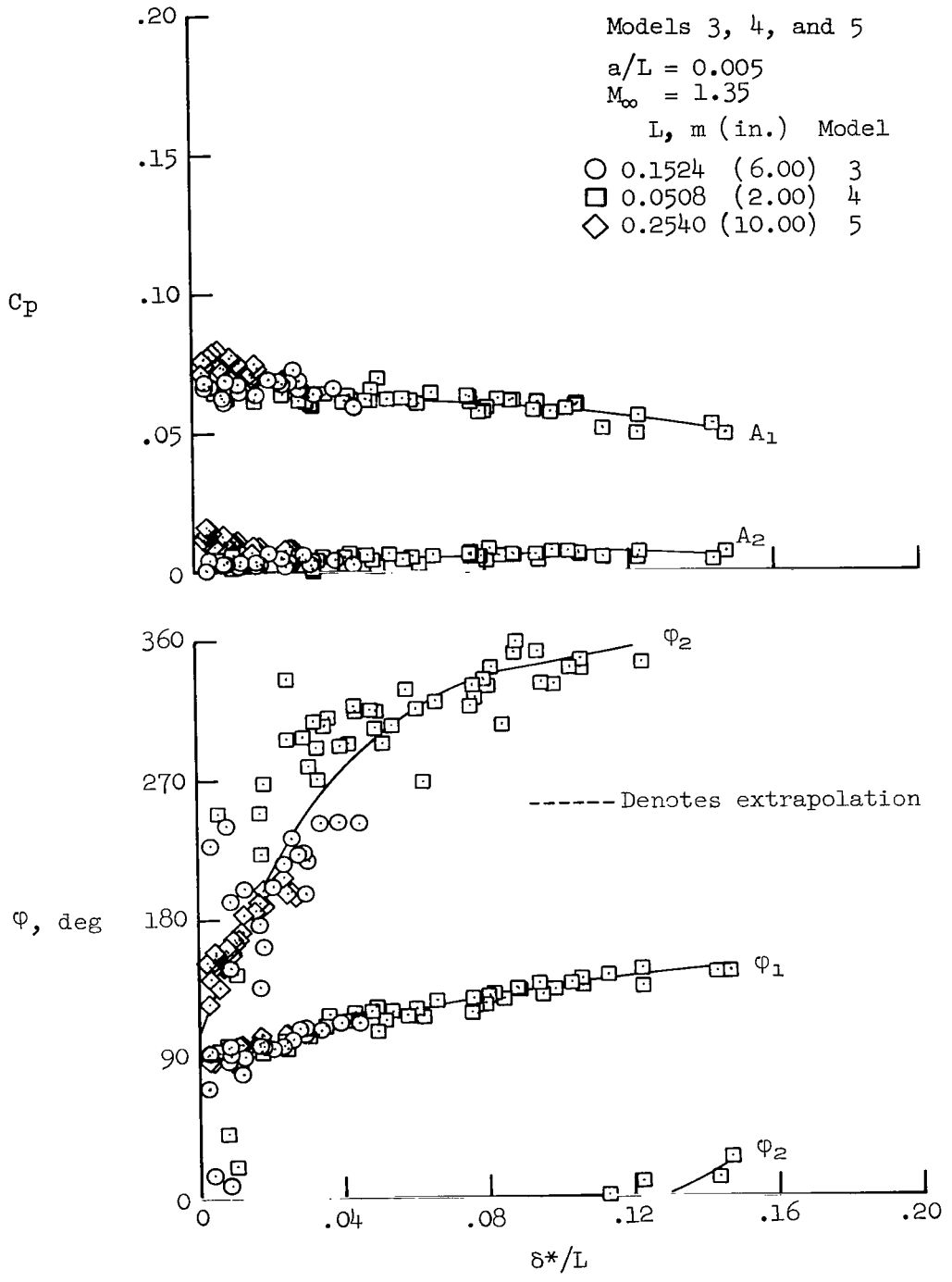

(g) M_∞ = 1.35

Figure 11.- Concluded.

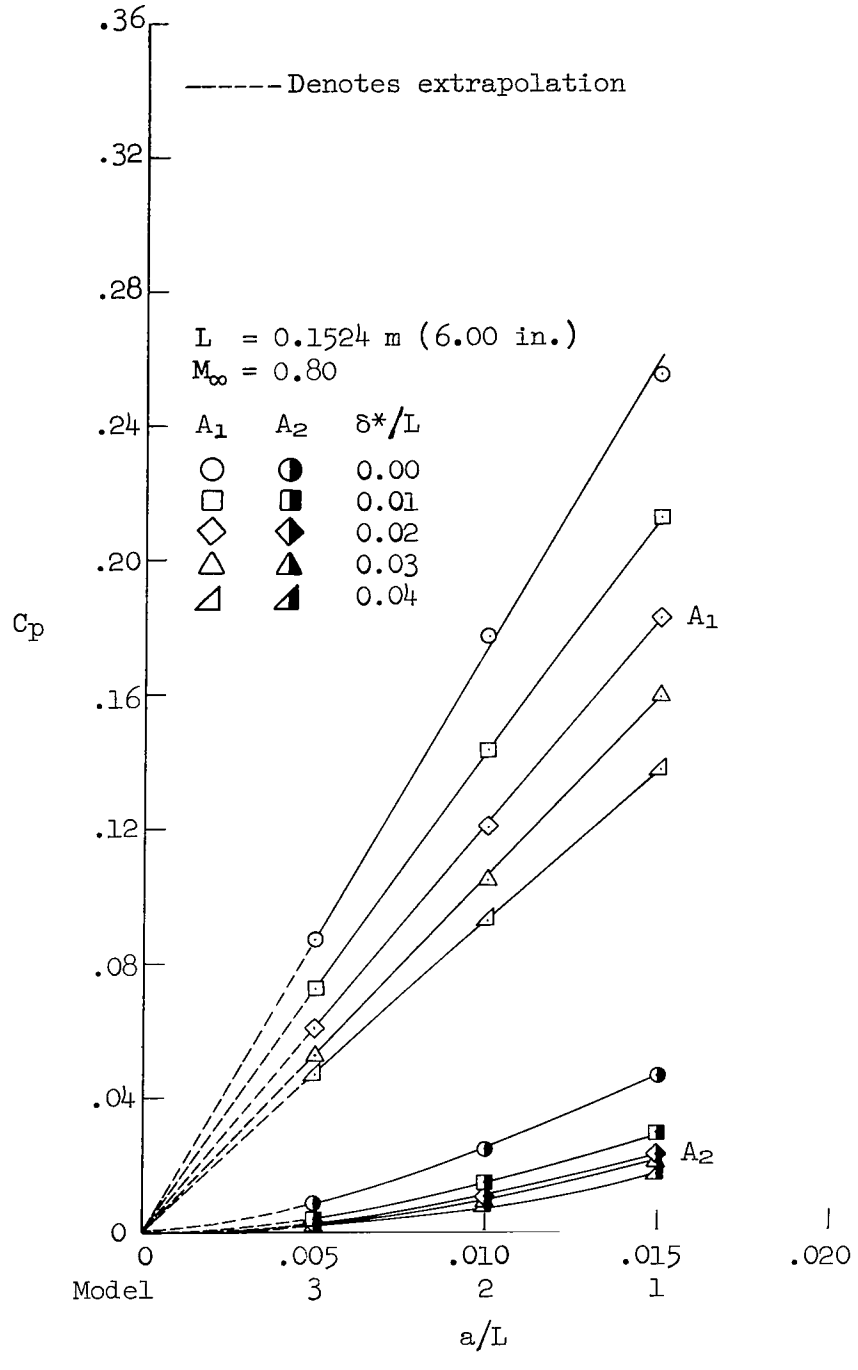

(a) $M_\infty = 0.80$

Figure 12.- Fourier components of the pressure coefficients as a function of amplitude-to-wavelength ratio.

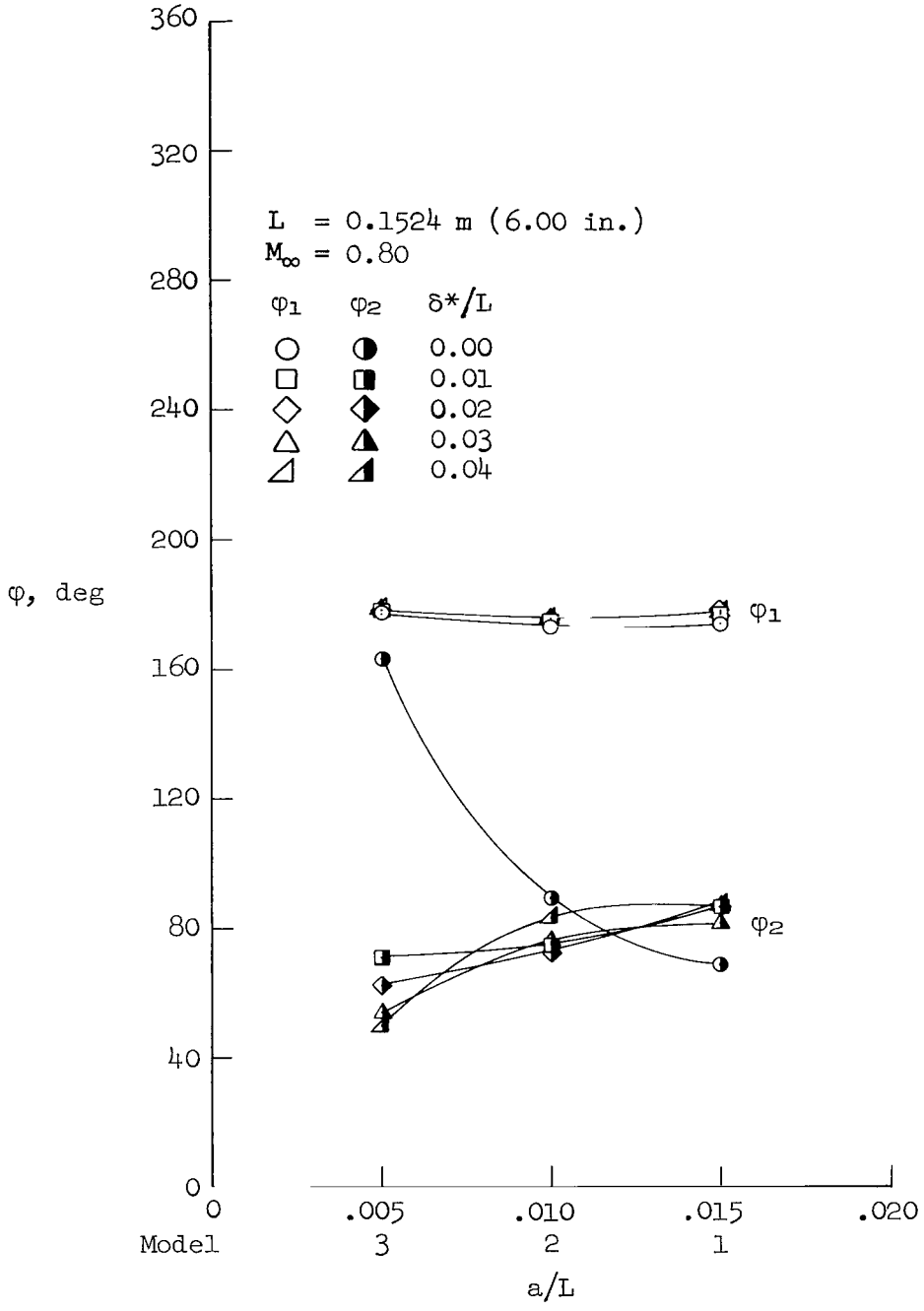

(a) $M_\infty = 0.80$ (concluded)

Figure 12.- Continued.

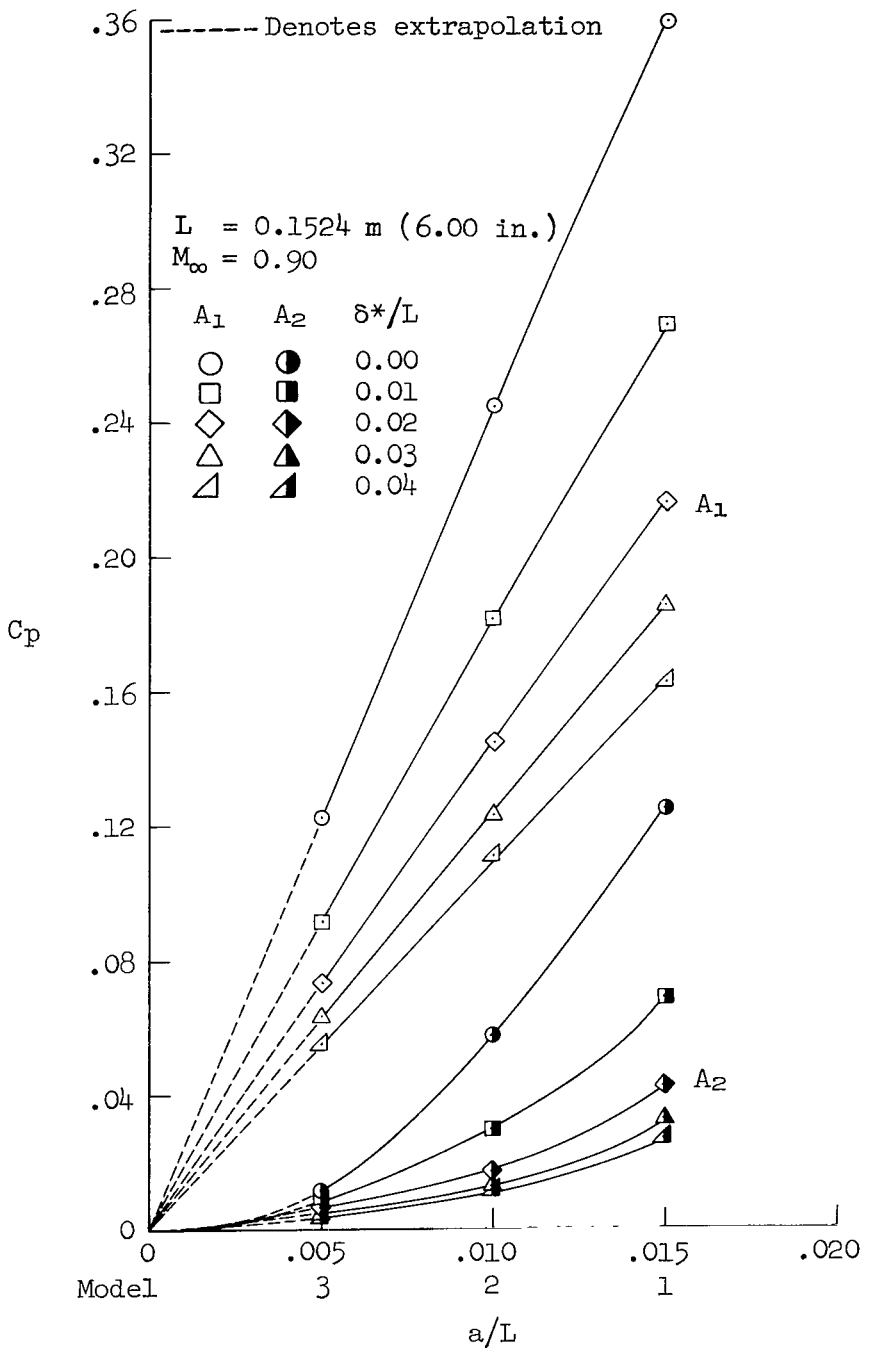

(b) $M_\infty = 0.90$

Figure 12.- Continued.

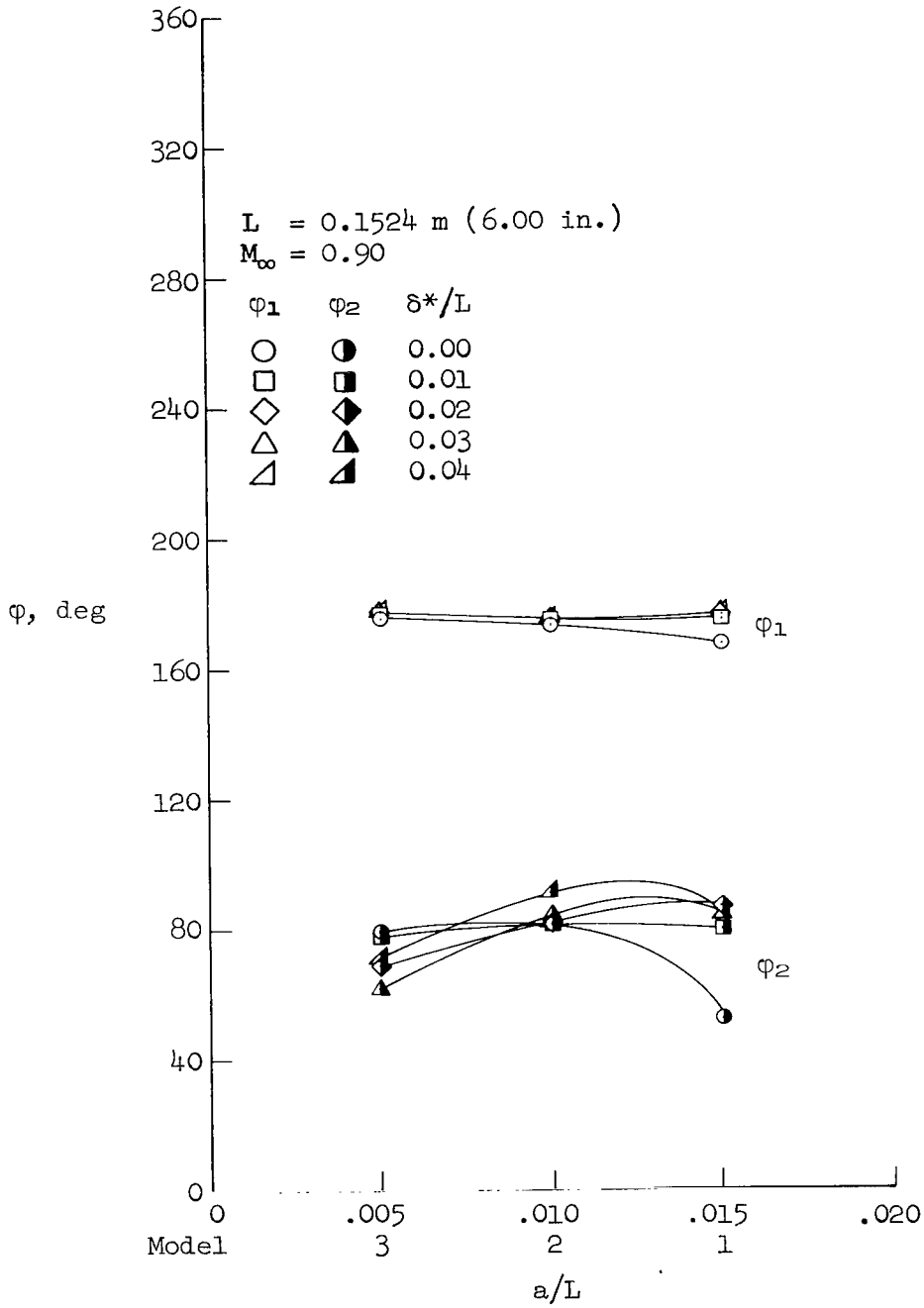

(b) $M_\infty = 0.90$ (concluded)

Figure 12.- Continued.

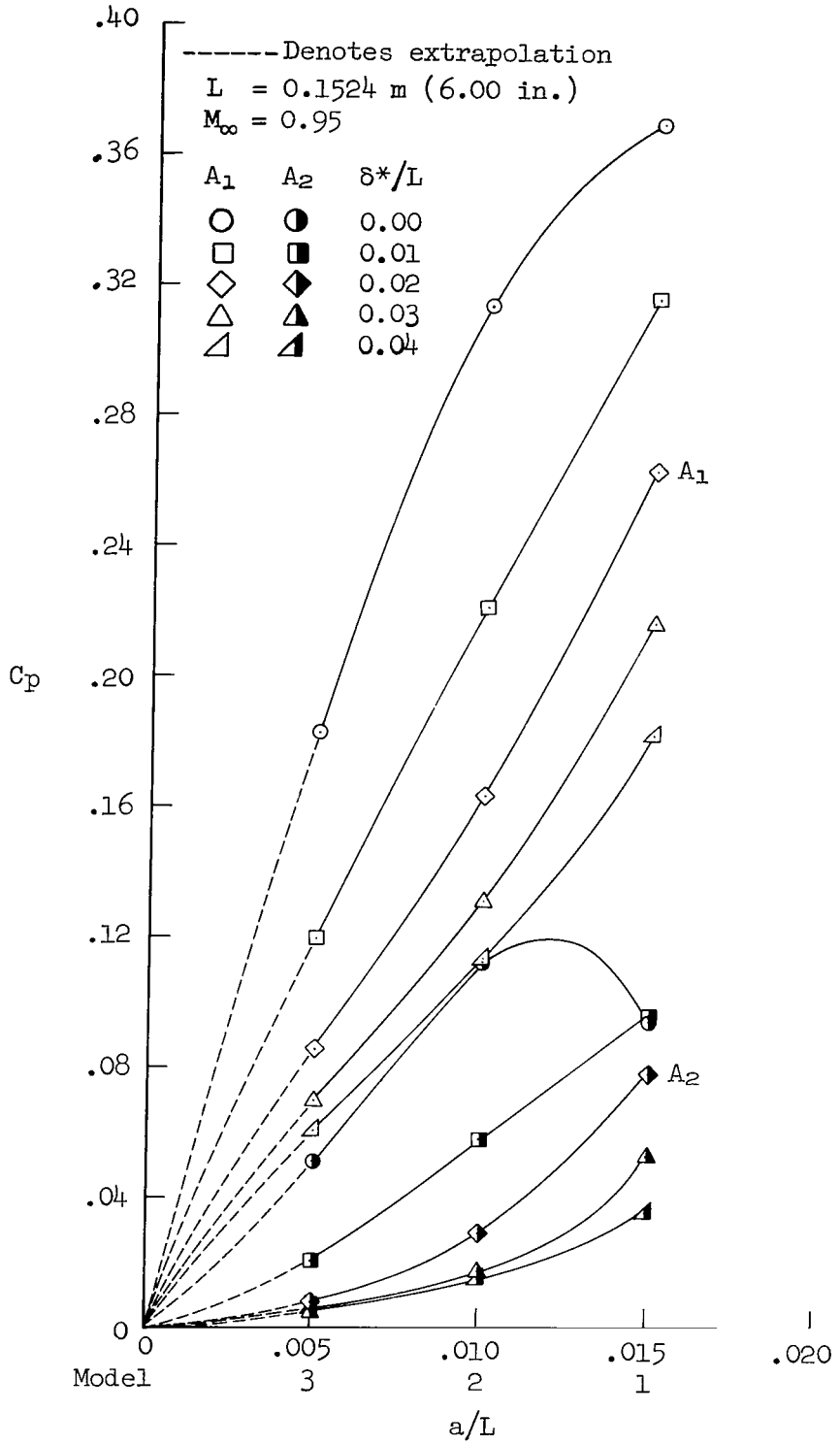

(c) M_∞ = 0.95

Figure 12.- Continued.

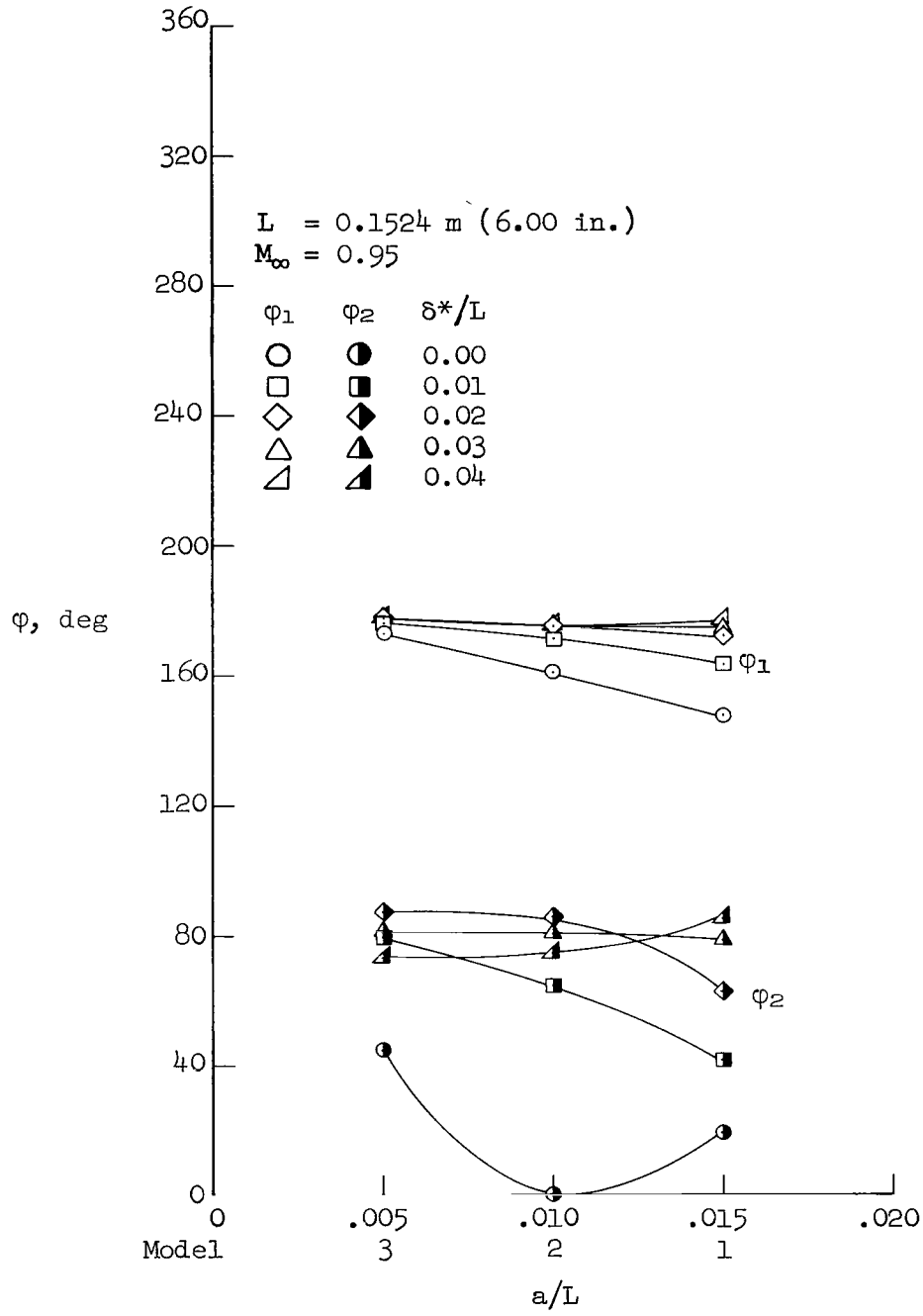

(c) M_∞ = 0.95 (concluded)

Figure 12.- Continued.

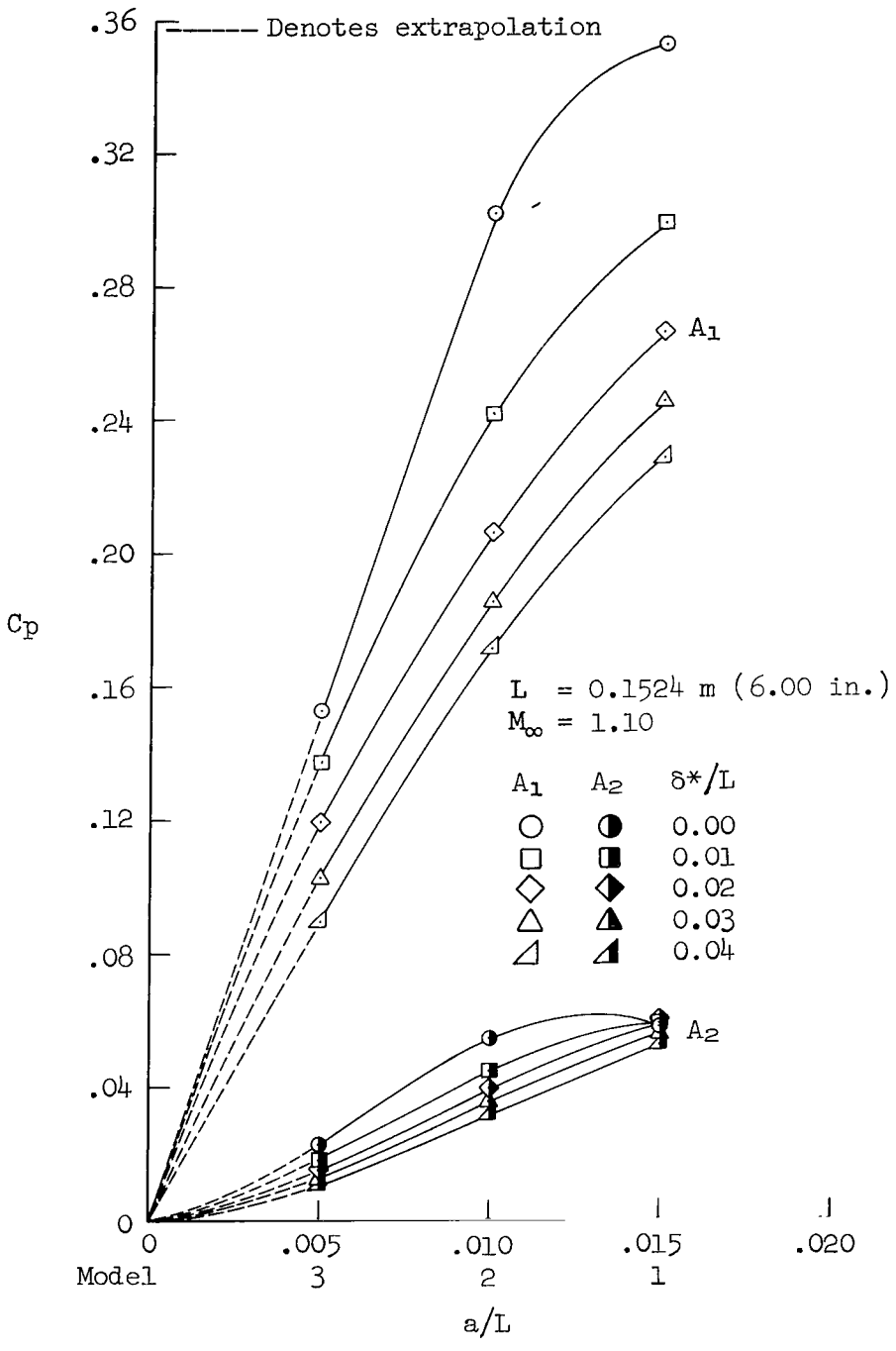

(d) $M_\infty = 1.10$

Figure 12.- Continued.

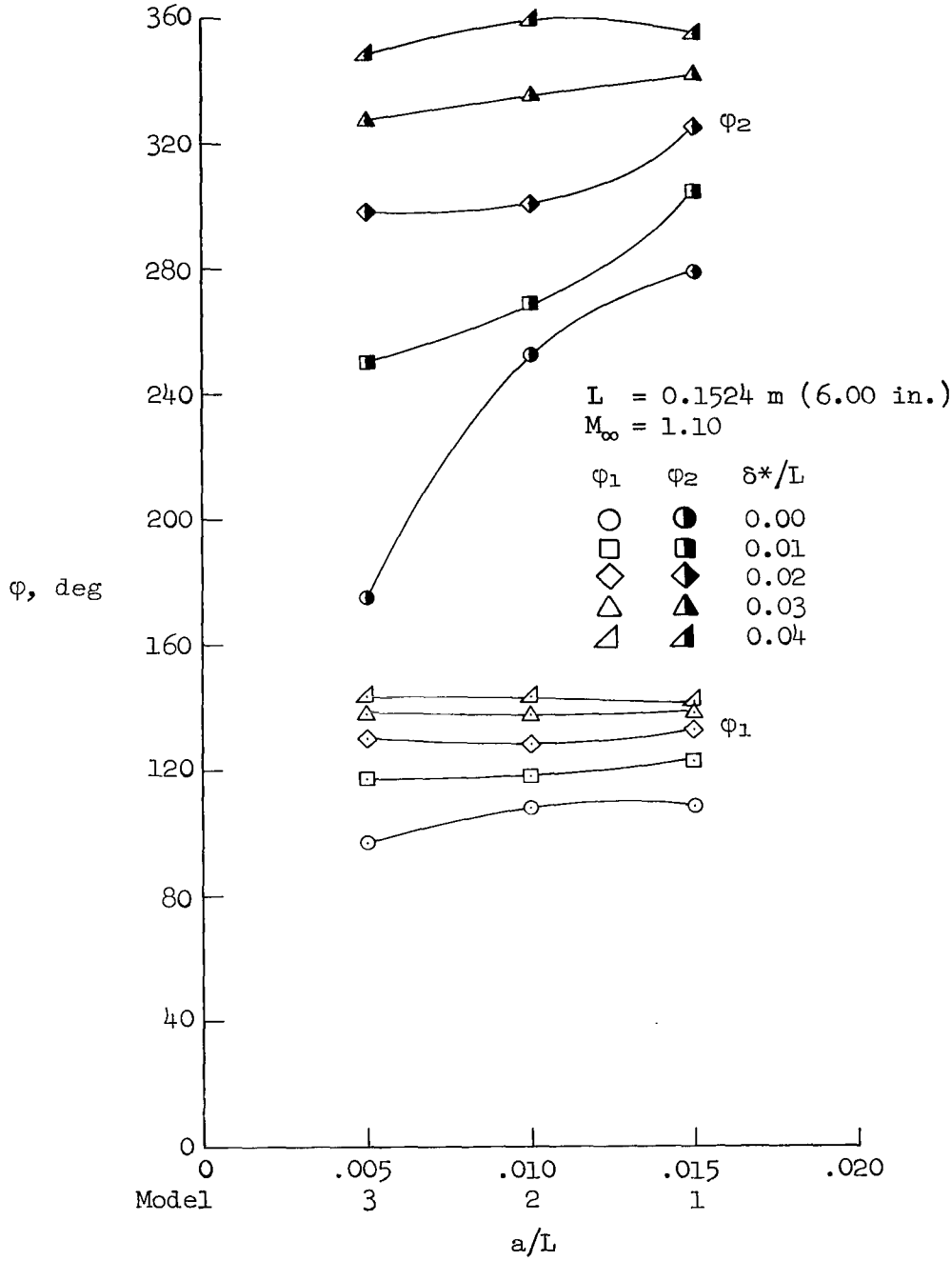

(d) $M_\infty = 1.10$ (concluded)

Figure 12.- Continued.

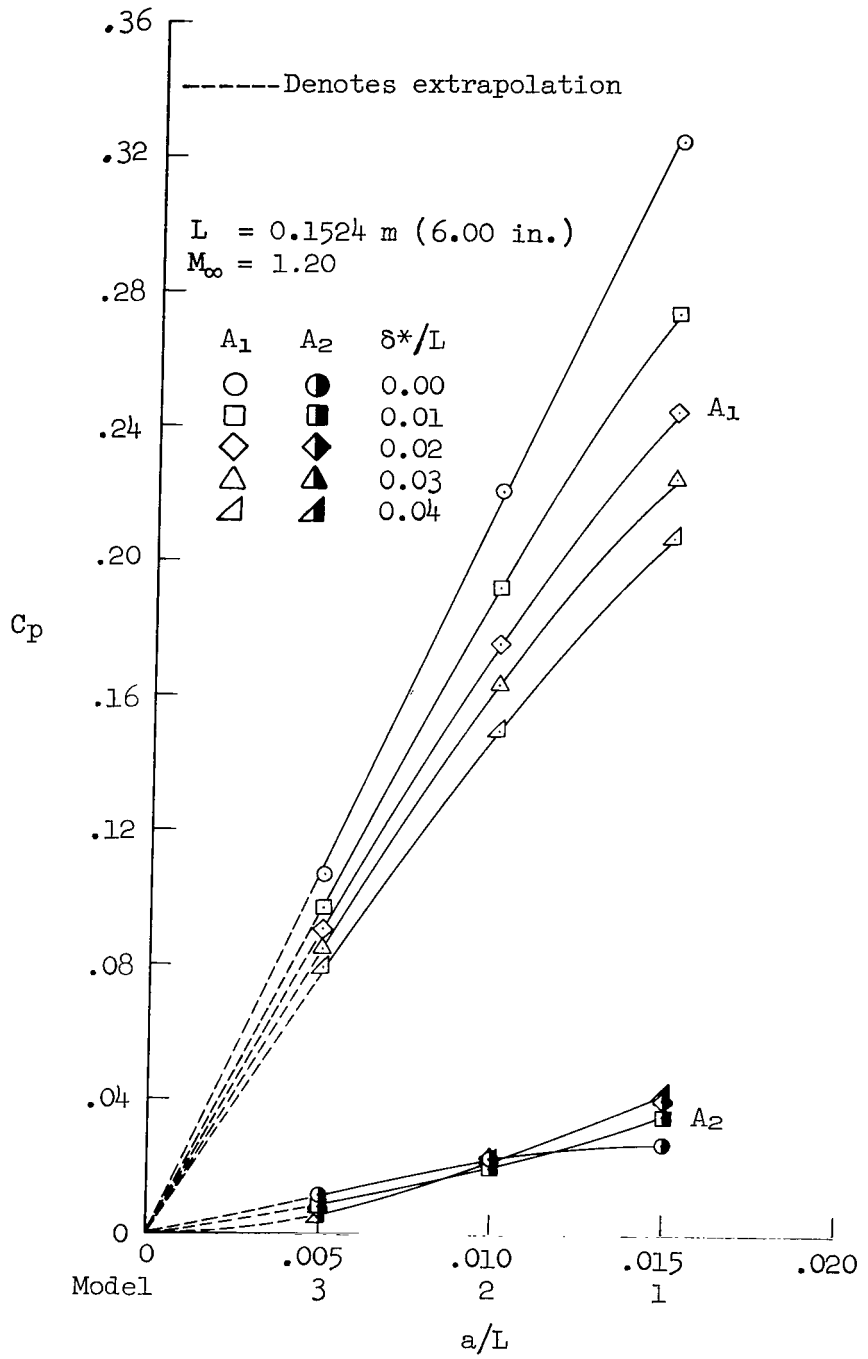

(e) $M_\infty = 1.20$

Figure 12.- Continued.

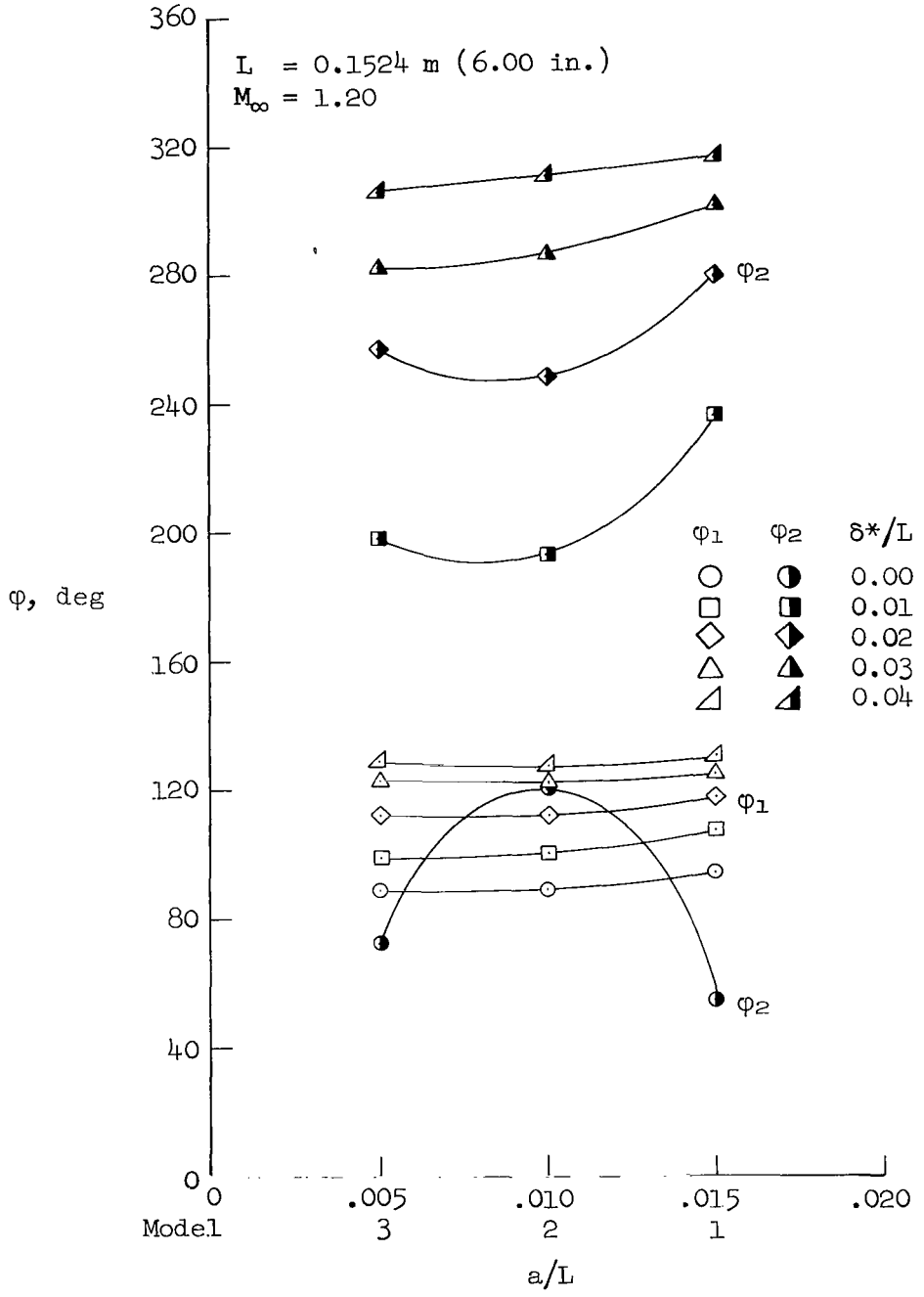

(e) M_∞ = 1.20 (concluded)

Figure 12.- Continued.

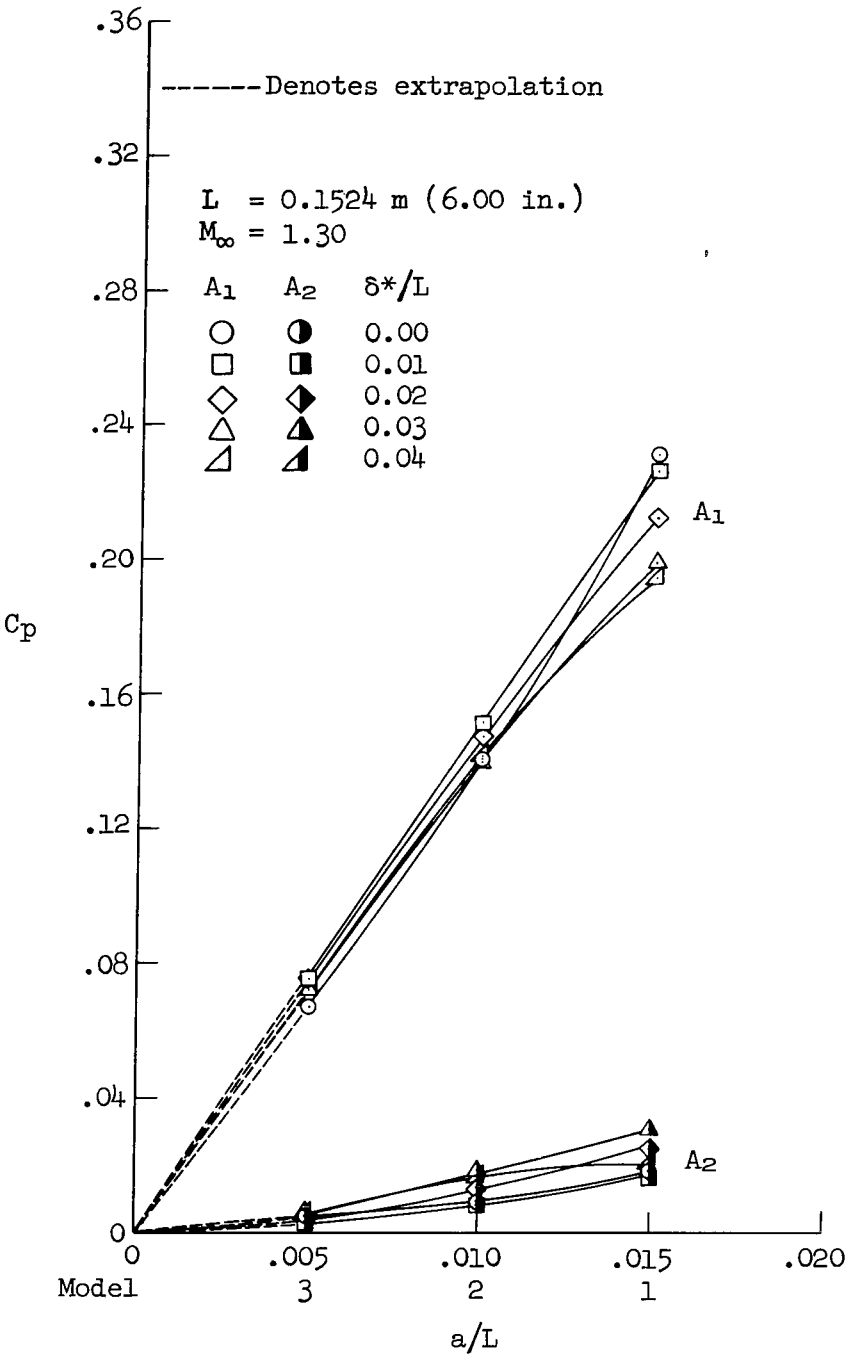

(f) M_∞ = 1.30

Figure 12.- Continued.

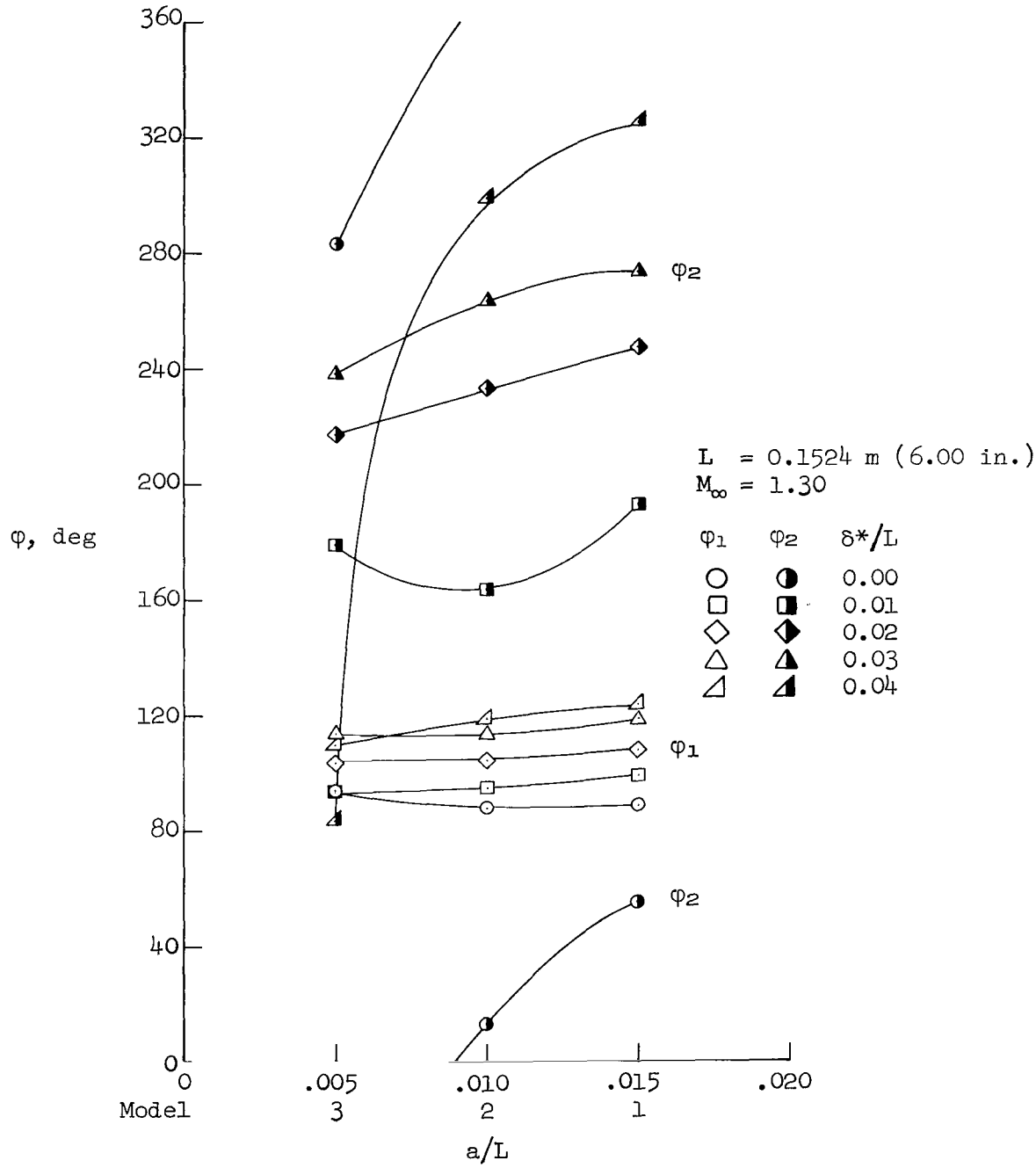

(f) M_∞ = 1.30 (concluded)

Figure 12.- Continued.

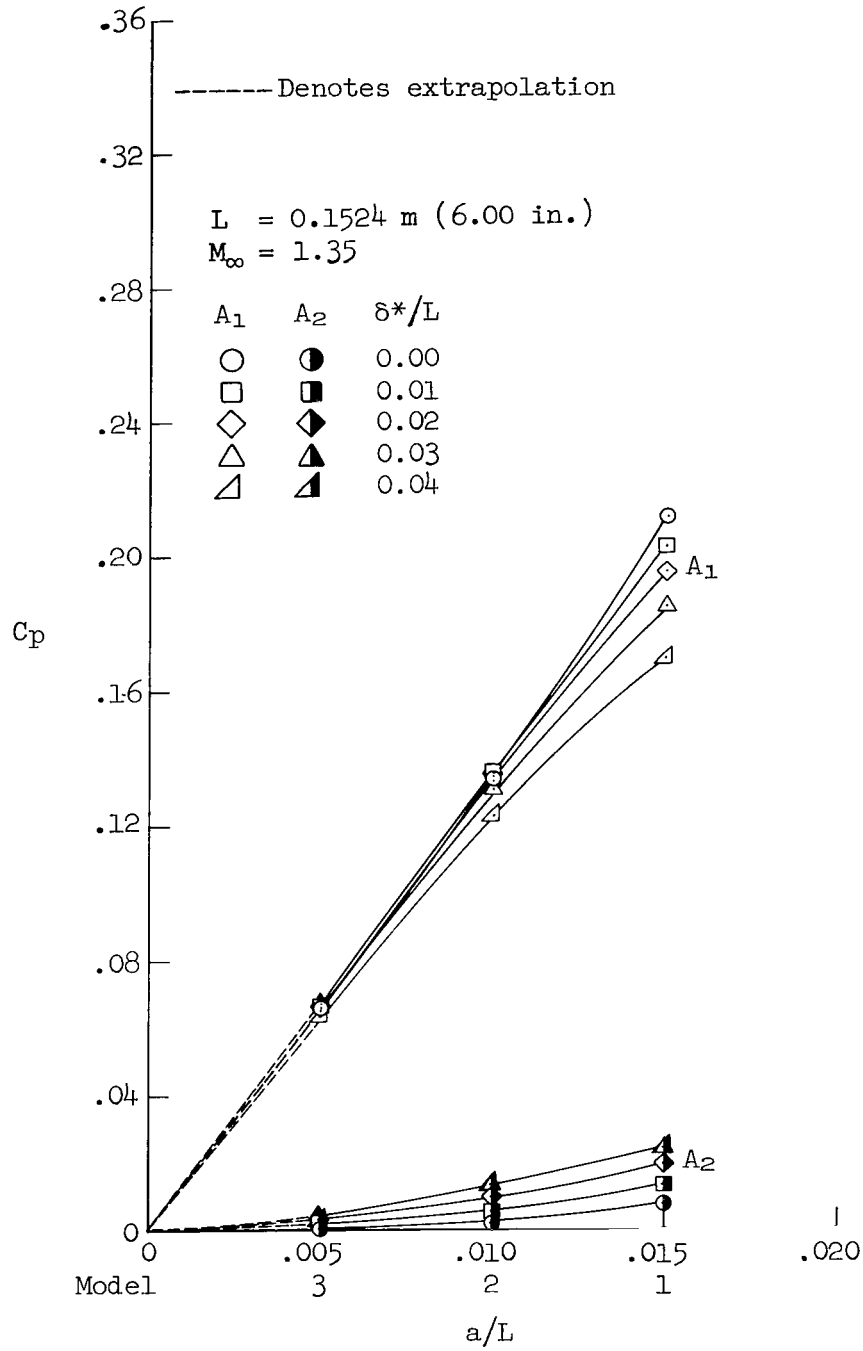

(g) M_∞ = 1.35

Figure 12.- Continued.

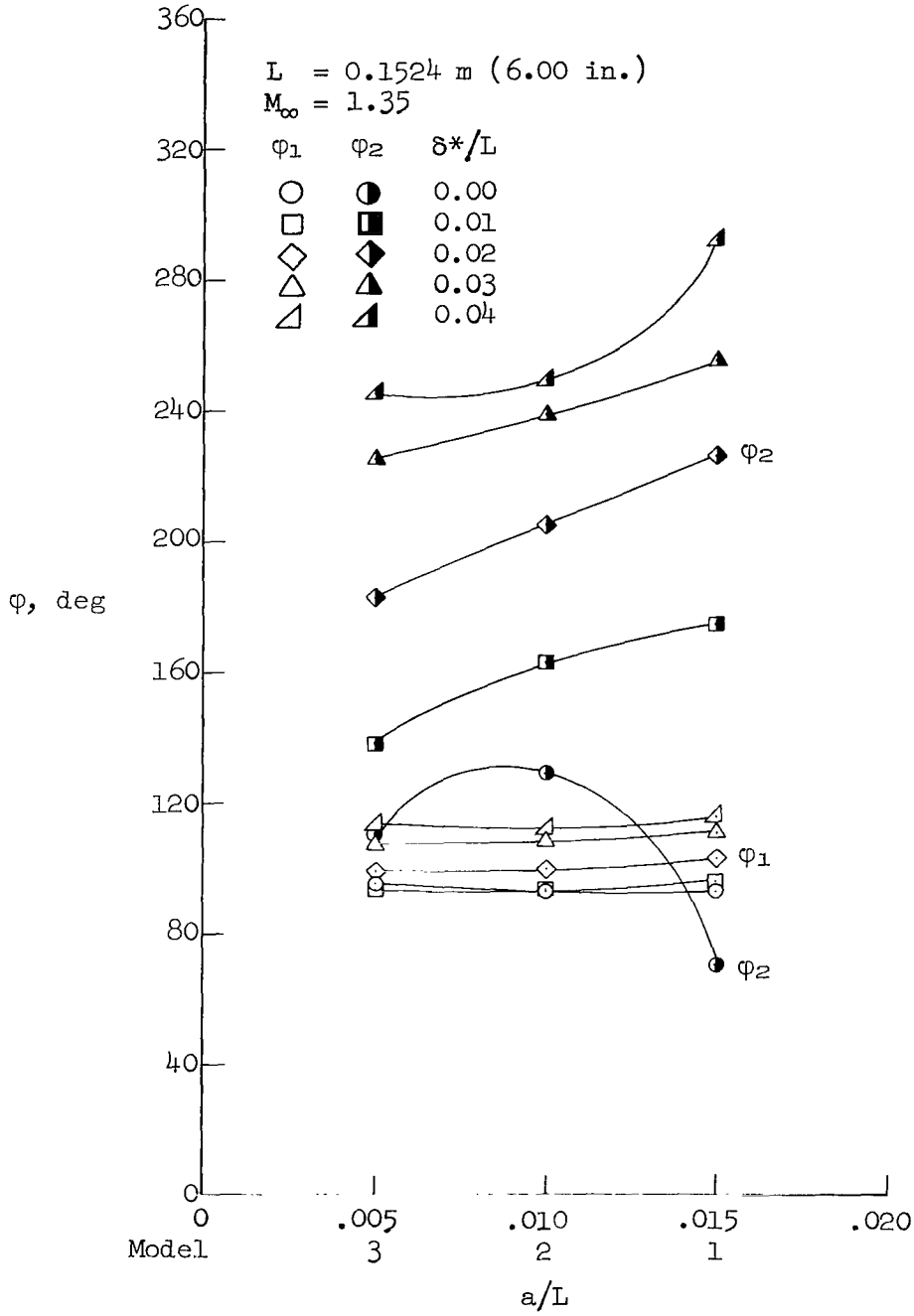

(g) M_∞ = 1.35 (concluded)

Figure 12.- Concluded.

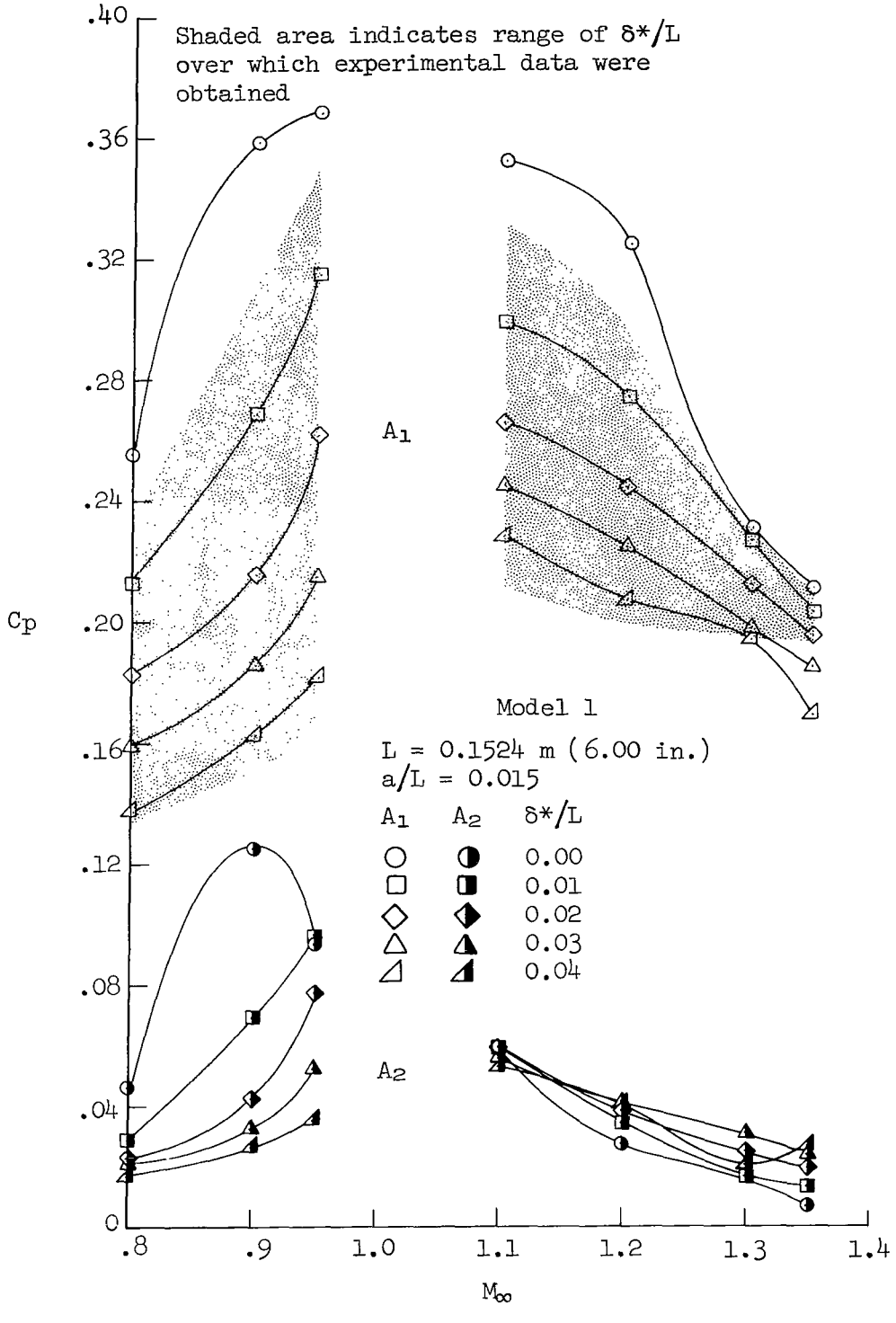

(a) Model 1; a/L = 0.015, L = 0.15240 m (6.00 in.)

Figure 13.- Fourier components of the pressure coefficients as a function of Mach number.

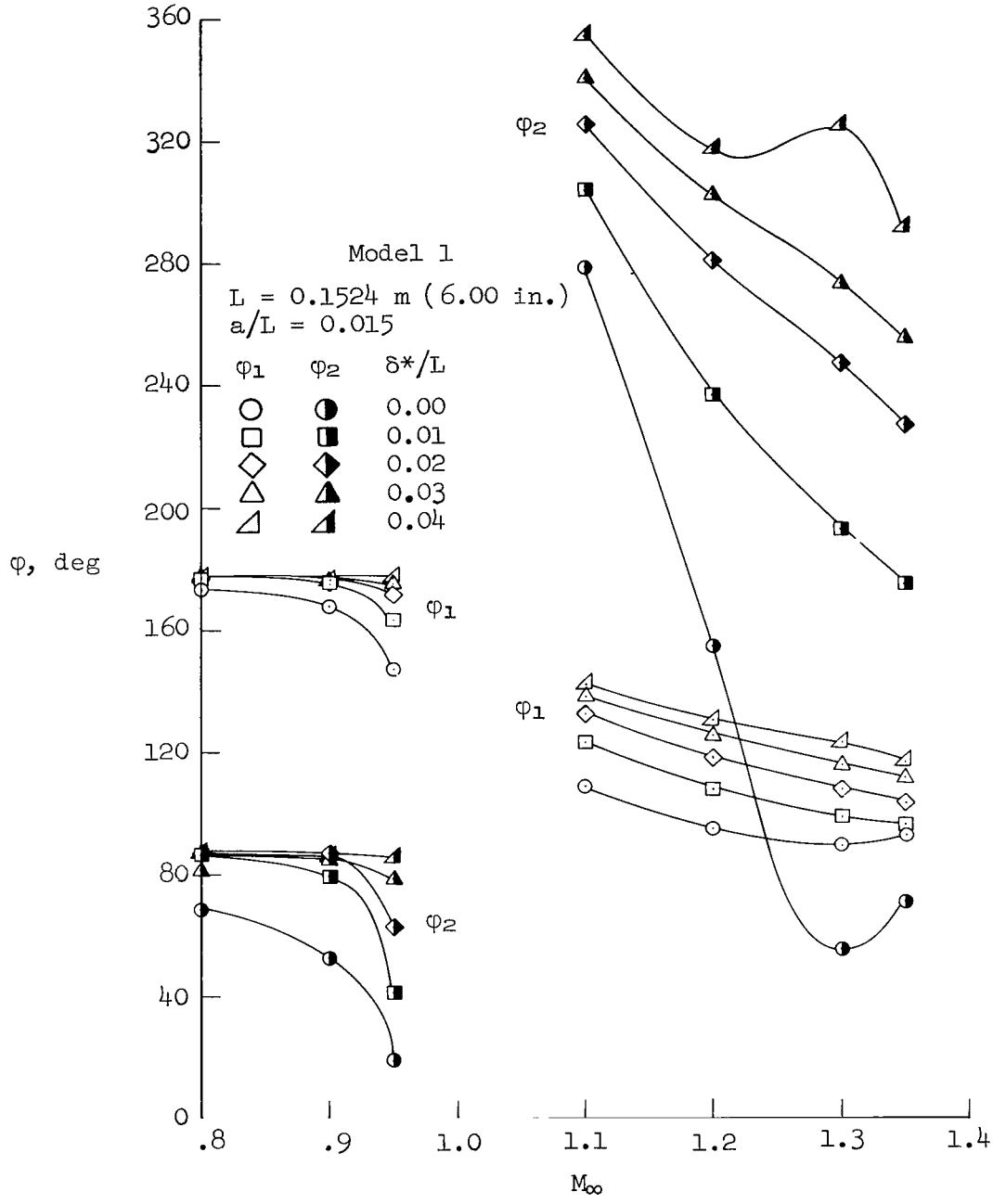

(a) Model 1; a/L = 0.015, L = 0.15240 m (6.00 in.) (concluded)

Figure 13.- Continued.

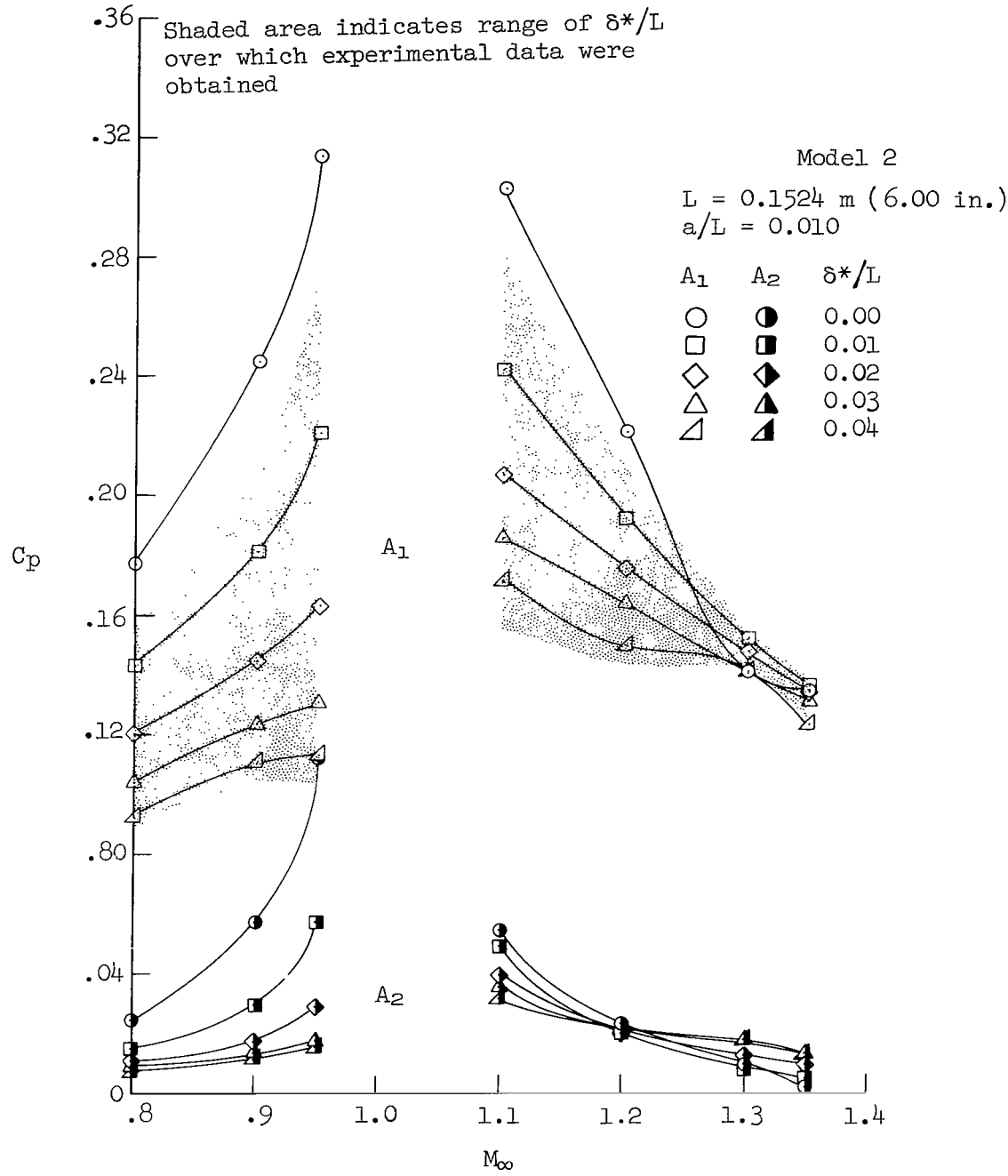

(b) Model 2; a/L = 0.010, L = 0.15240 m (6.00 in.)

Figure 13.- Continued.

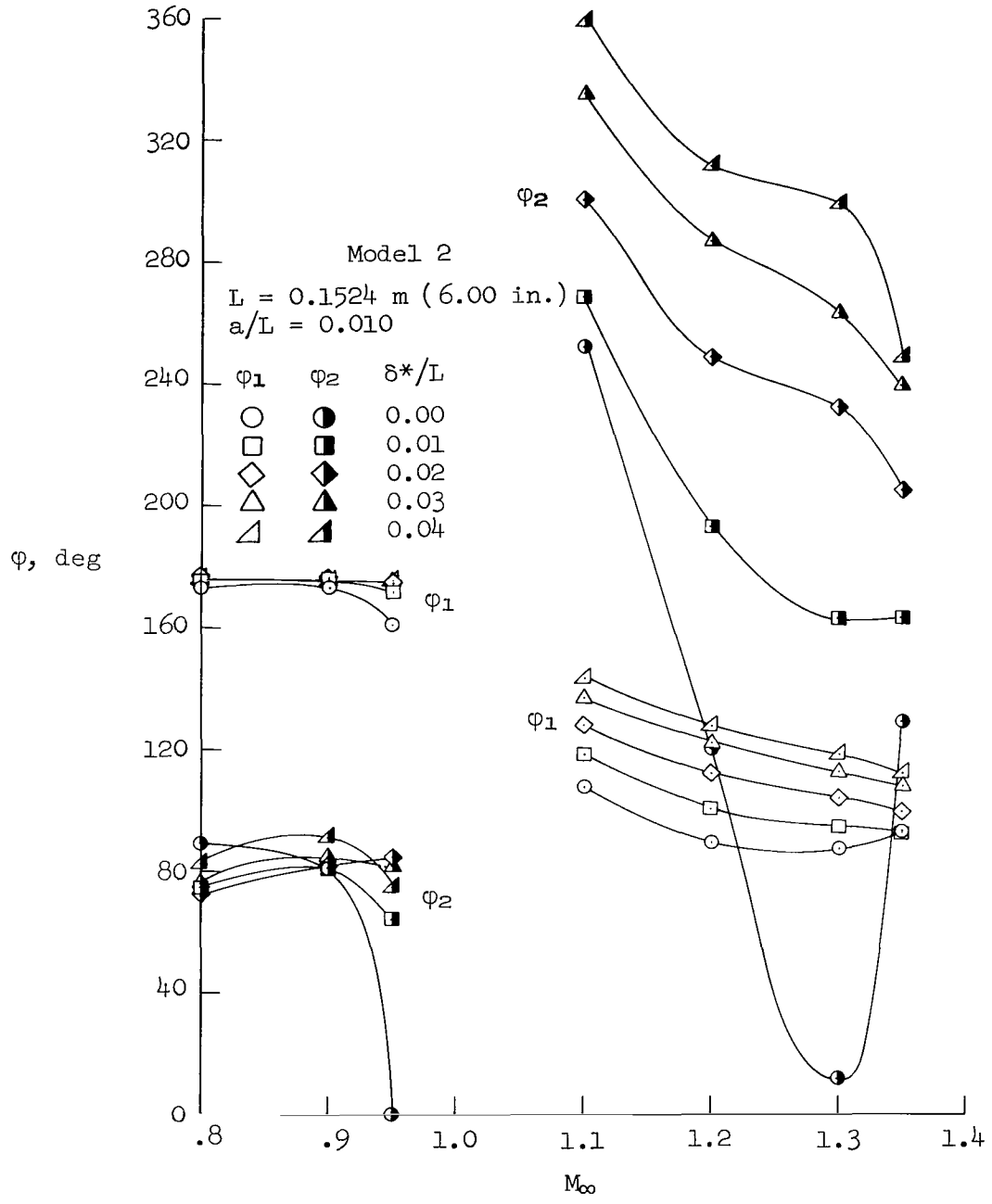

(b) Model 2; a/L = 0.010, L = 0.15240 m (6.00 in.) (concluded)

Figure 13.- Continued.

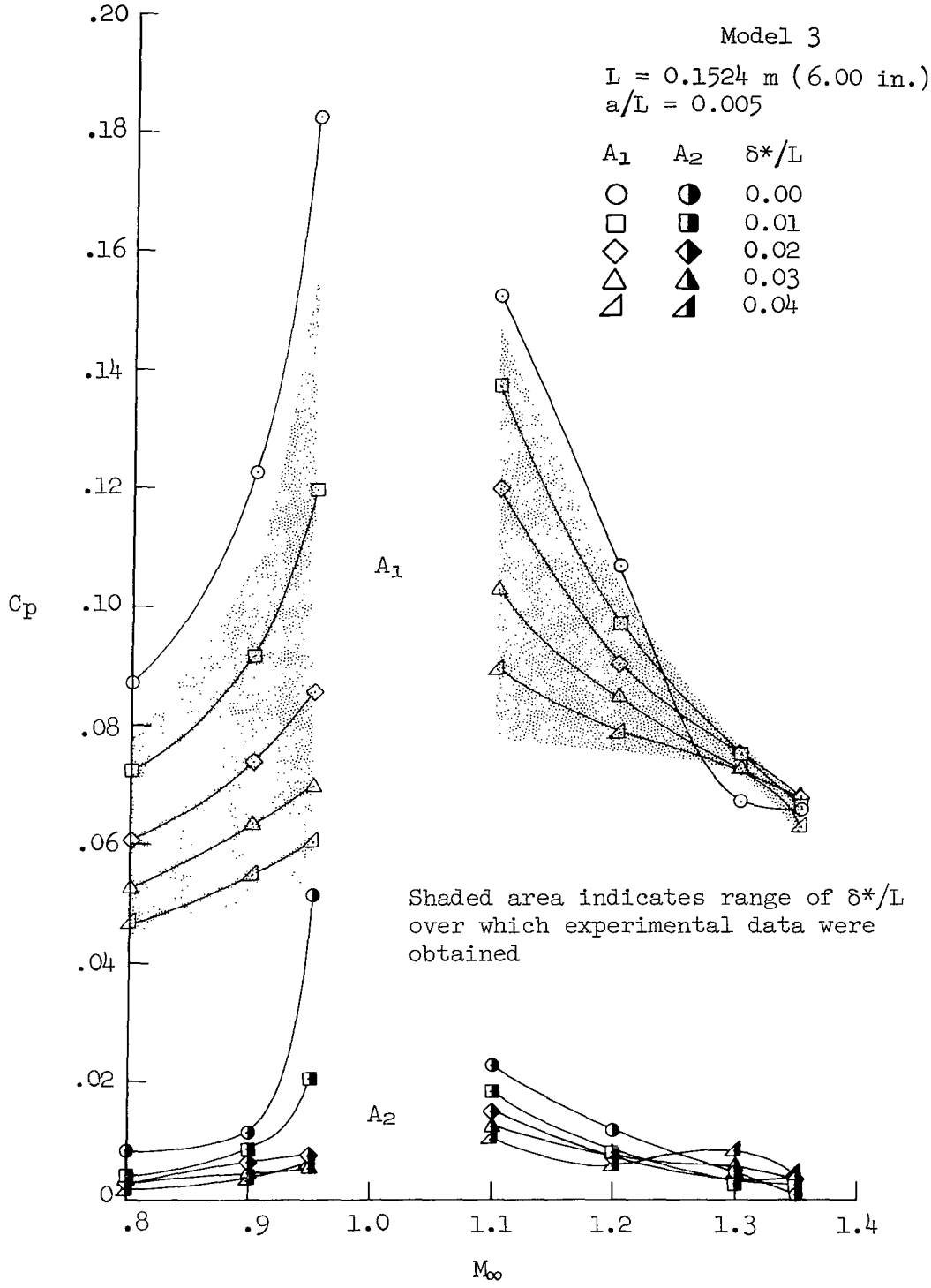

(c) Model 3; a/L = 0.005, L = 0.15240 m (6.00 in.)

Figure 13.- Continued.

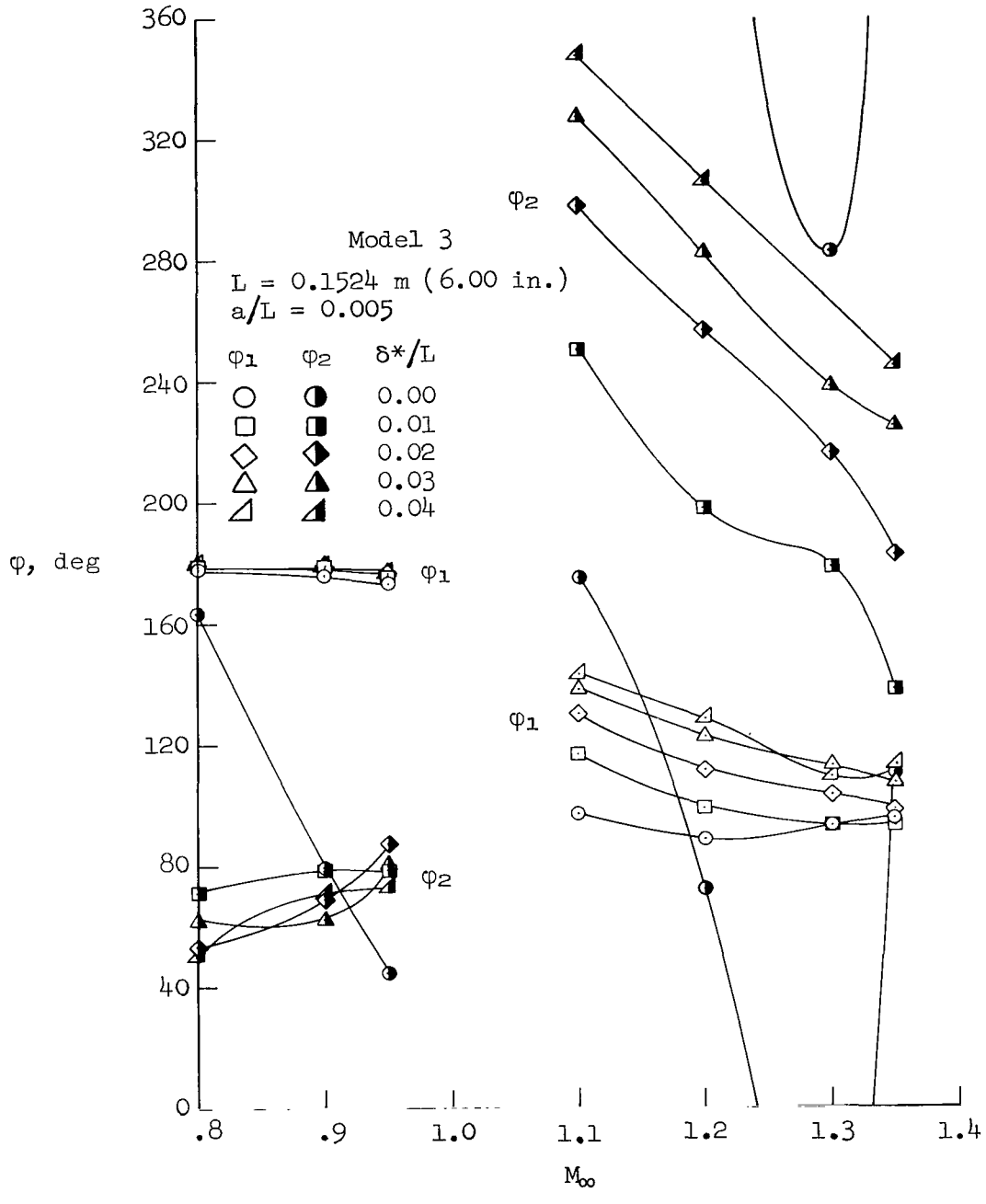

(c) Model 3; a/L = 0.005, L = 0.15240 m (6.00 in.) (concluded)

Figure 13.- Continued.

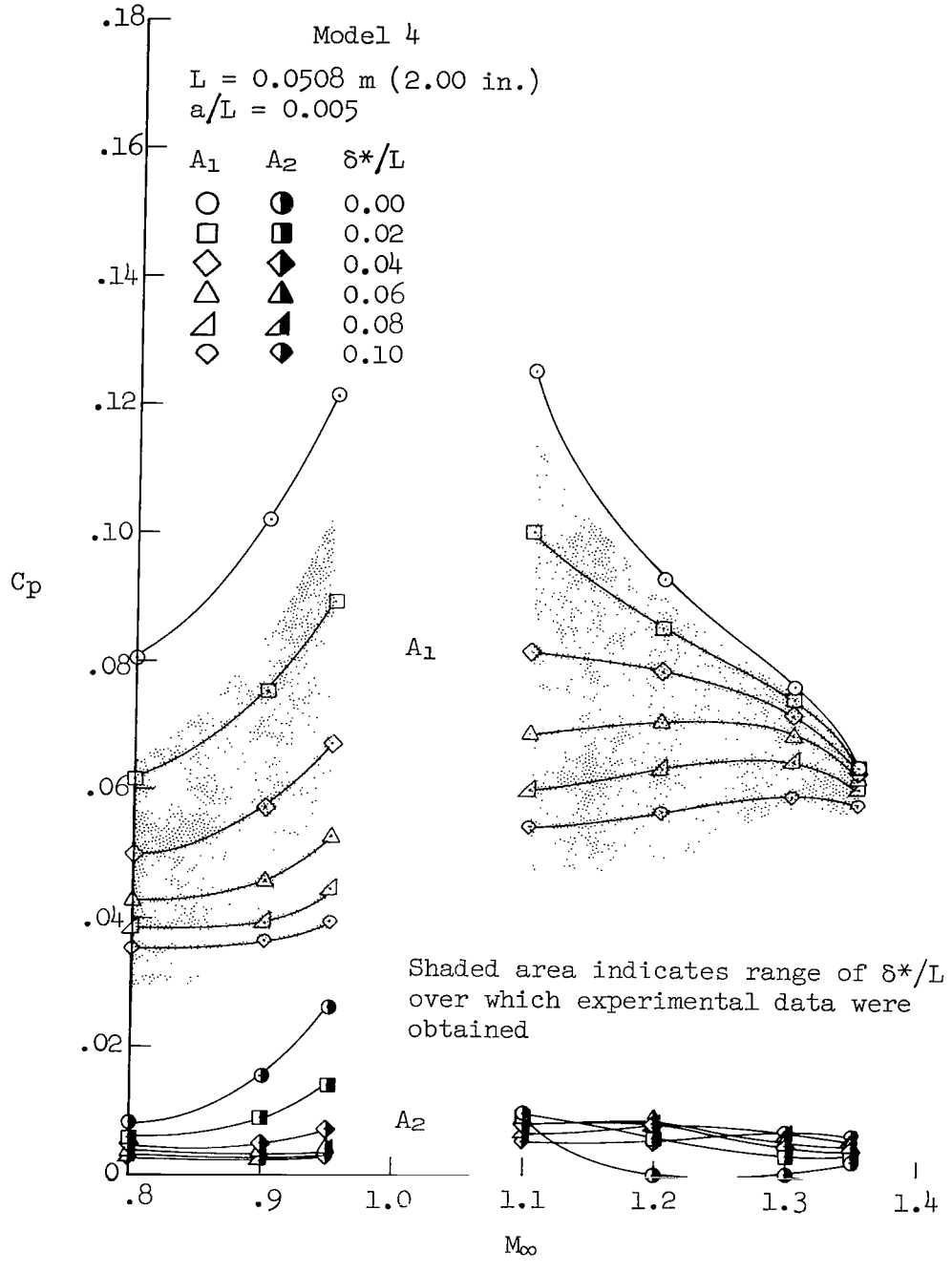

(d) Model 4; a/L = 0.005, L = 0.05080 m (2.00 in.)

Figure 13.- Continued.

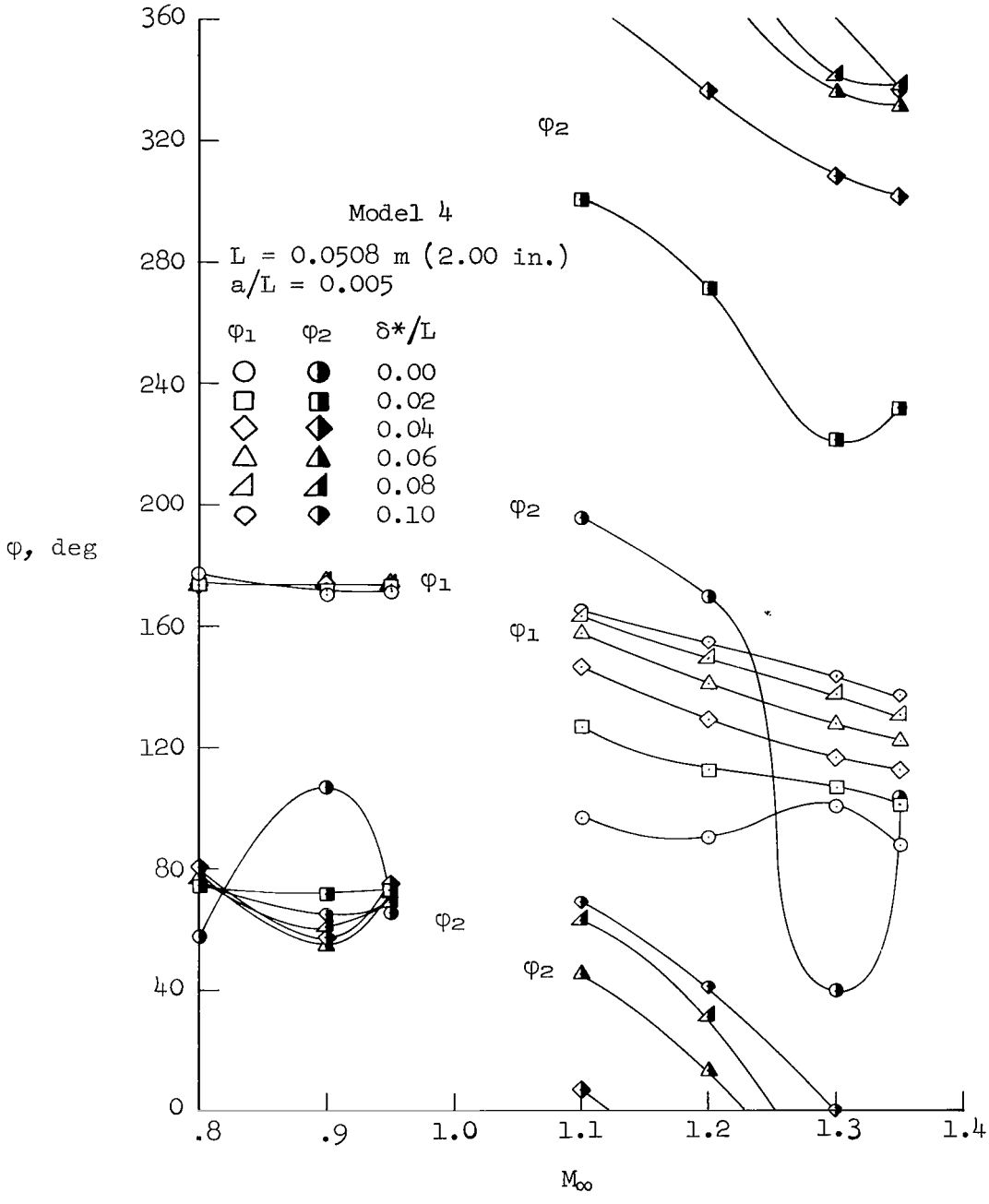

(d) Model 4; a/L = 0.005, L = 0.05080 (2.00 in.) (concluded)

Figure 13.- Continued.

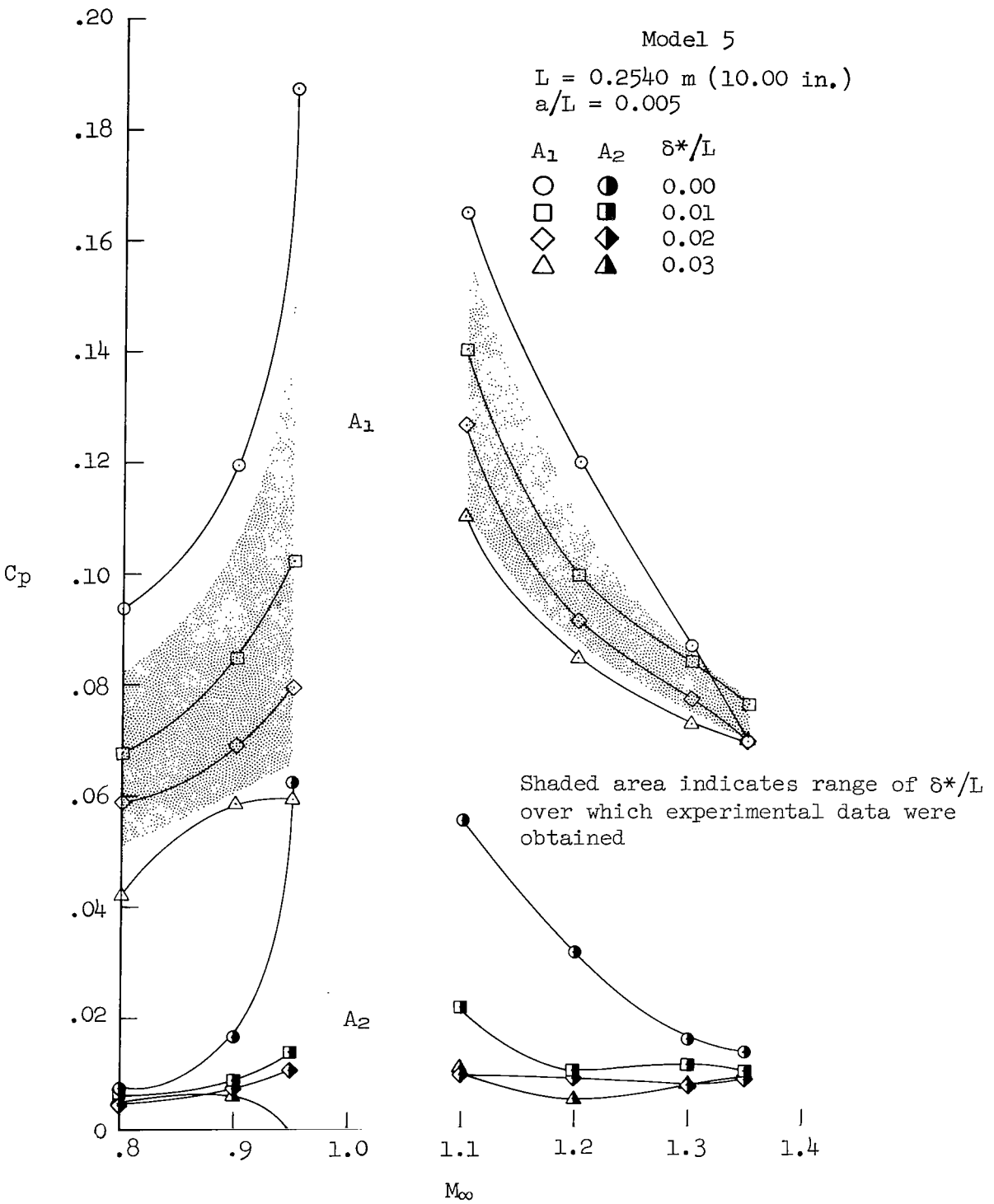

(e) Model 5; a/L = 0.005, L = 0.25400 m (10.00 in.)

Figure 13.- Continued.

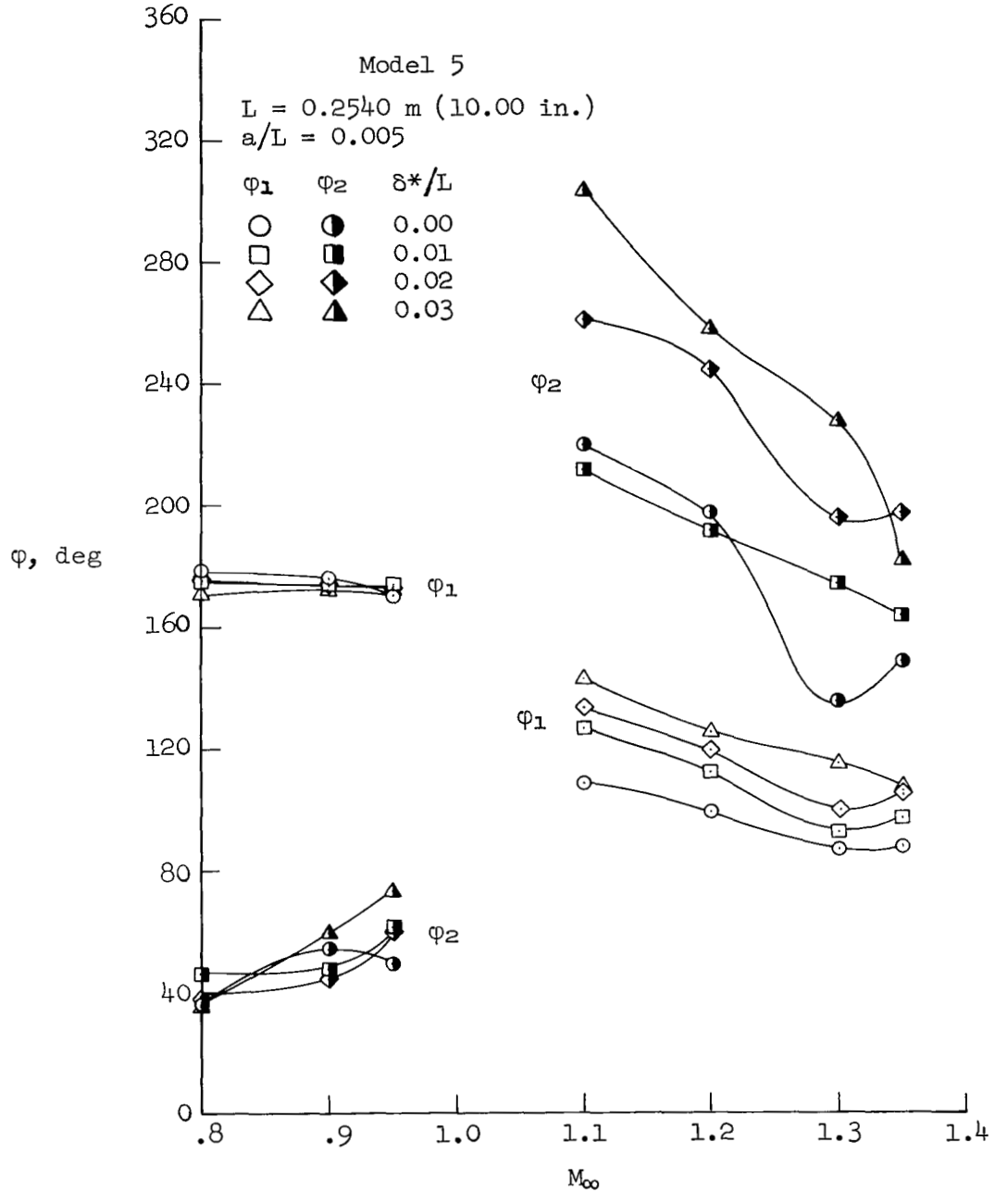

(e) Model 5; a/L = 0.005, L = 0.25400 m (10.00 in.) (concluded)

Figure 13.- Continued.

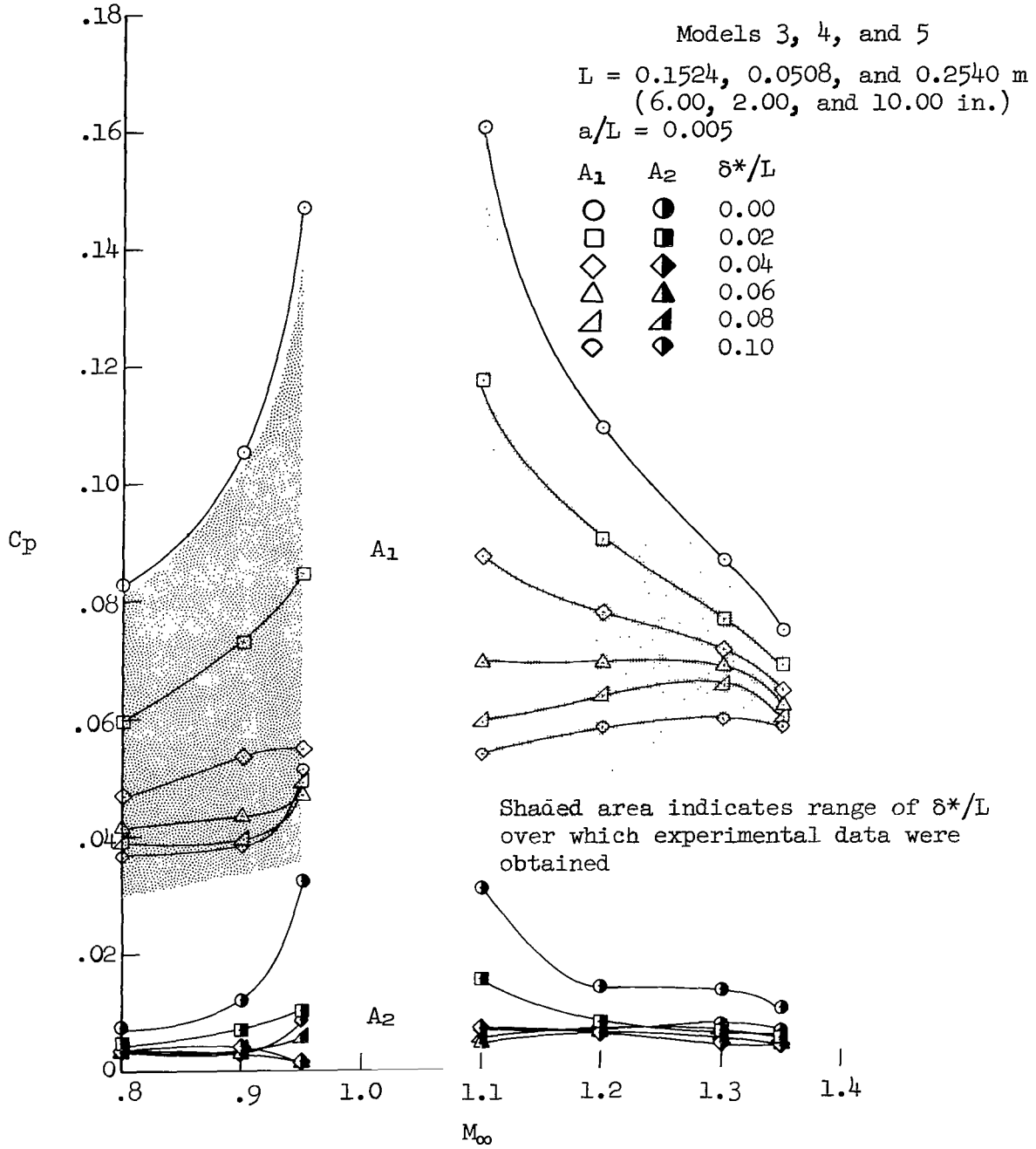

(f) Models 3, 4 and 5 combined; a/L = 0.005, L = 0.15240, 0.05080 and 0.25400 m (6.00, 2.00 and 10.00 in.)

Figure 13.- Continued.

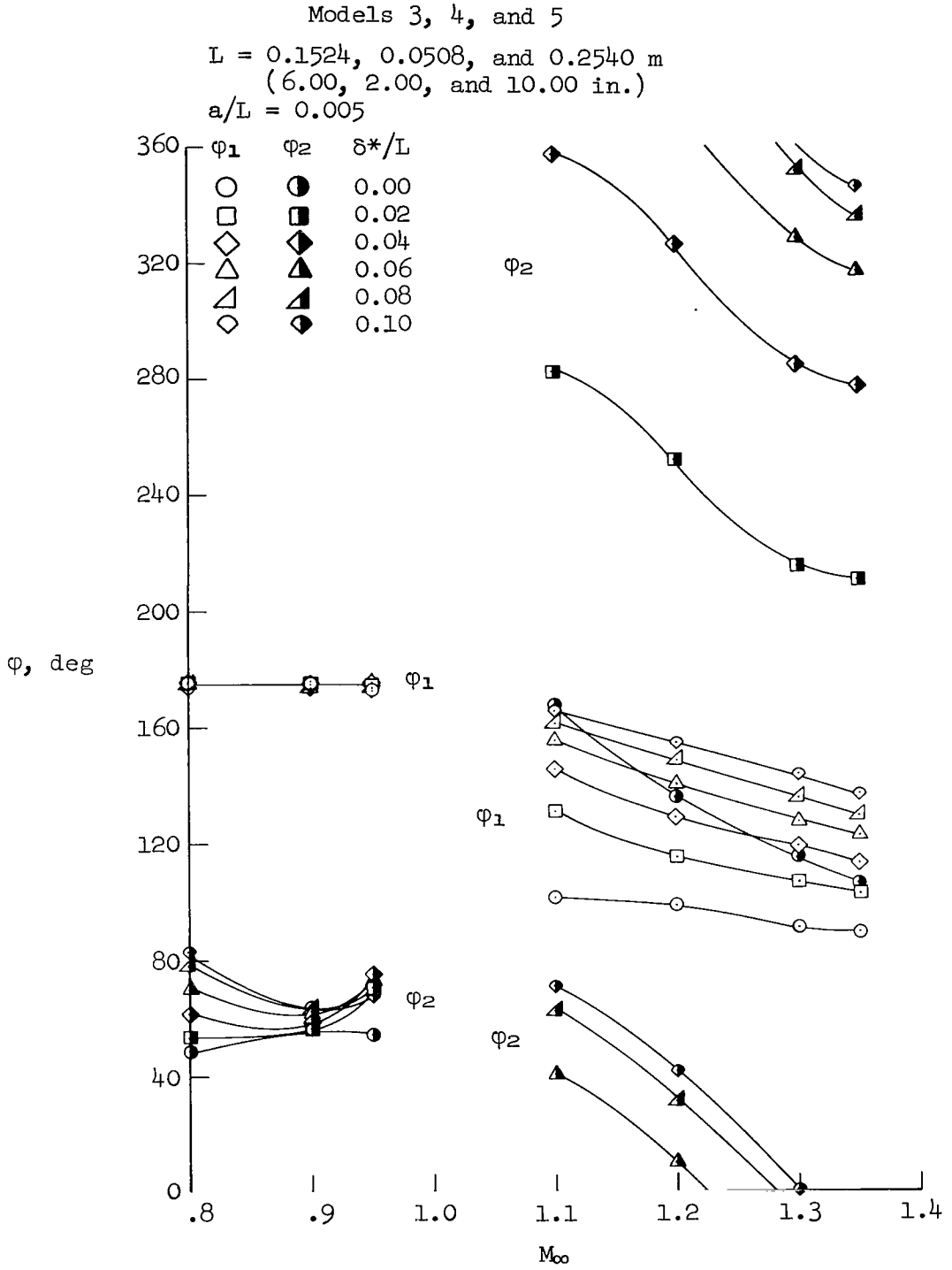

(f) Models 3, 4 and 5 combined; a/L = 0.005, L = 0.15240, 0.05080 and 0.25400 m (6.00, 2.00 and 10.00 in.) (concluded)

Figure 13.- Concluded.

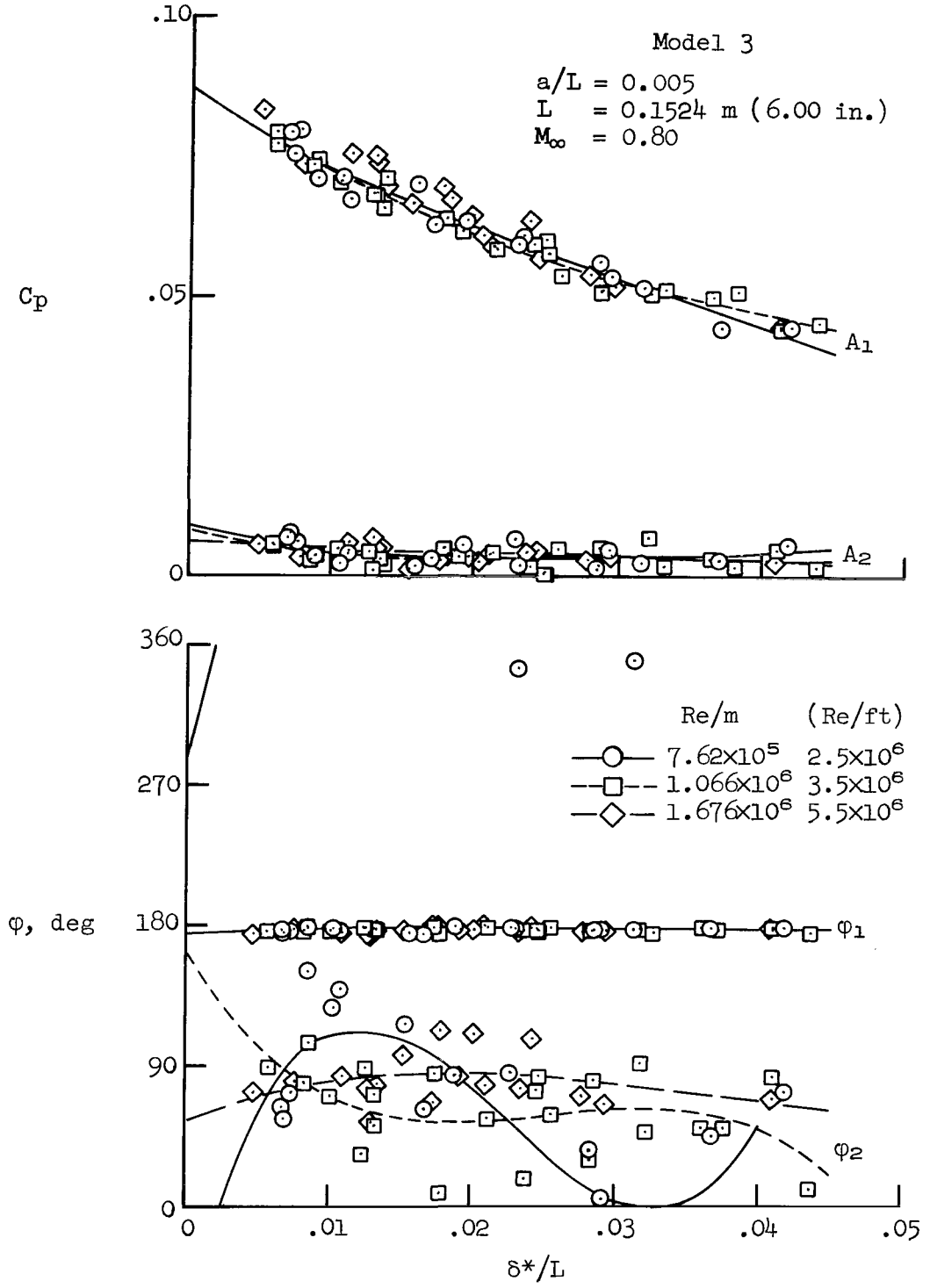

Figure 14.- Fourier components of the pressure coefficients as a function of the dimensionless boundary-layer displacement thickness for various unit Reynolds numbers at $M_\infty = 0.80$.

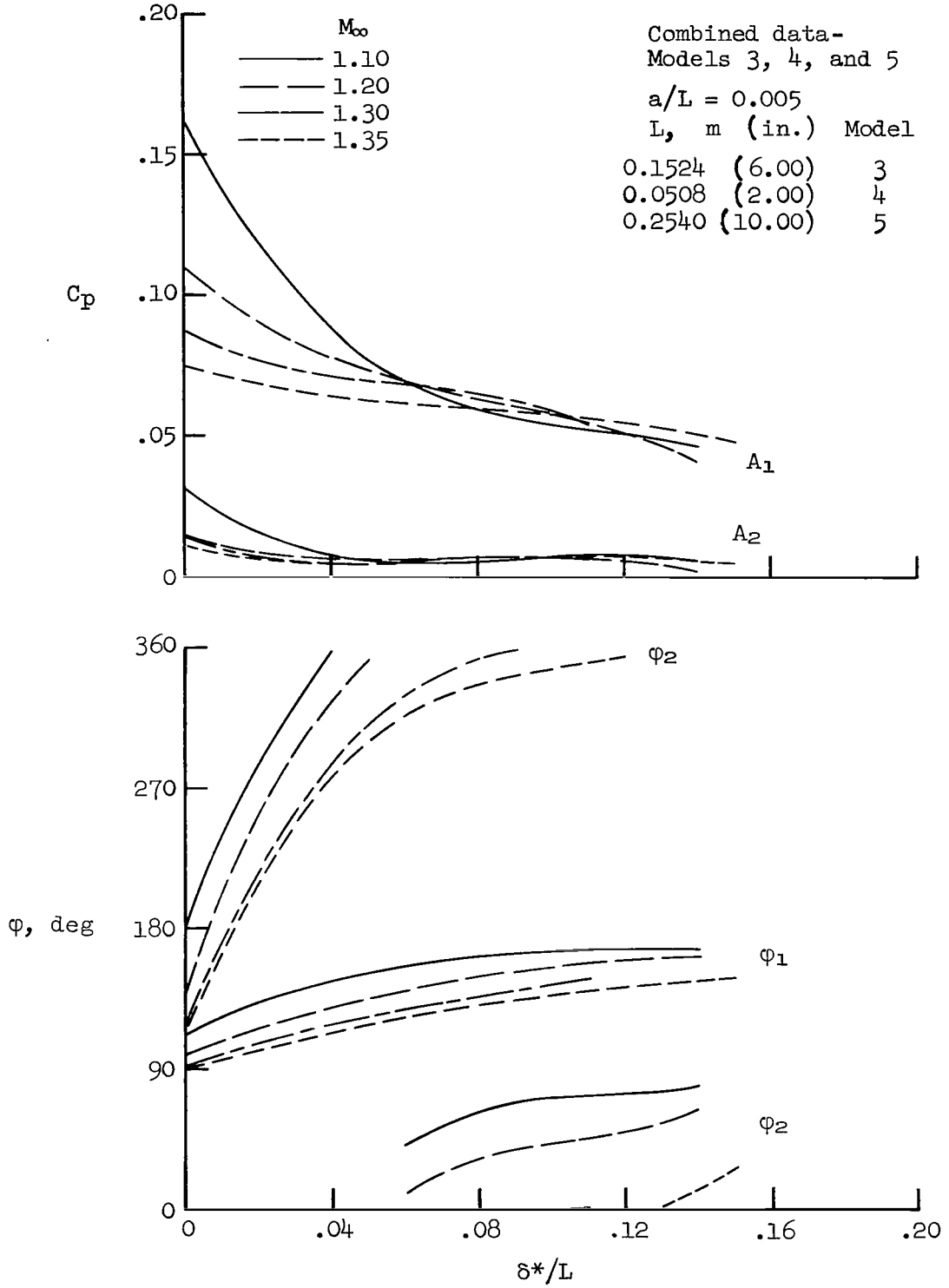

Figure 15.- Phase angle and amplitude of the pressure coefficients as a function of the dimensionless boundary-layer displacement thickness at supersonic Mach numbers.

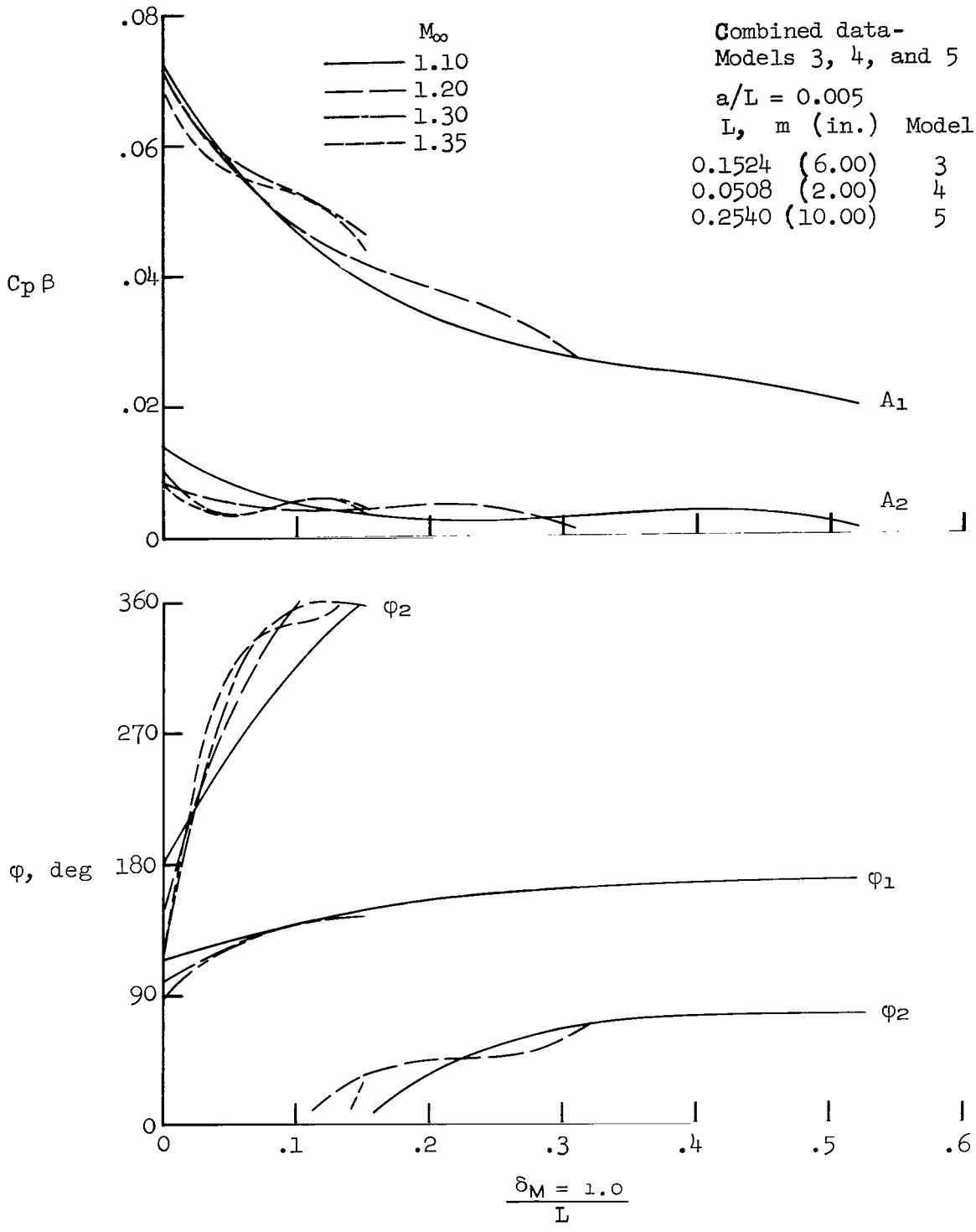

Figure 16.- Phase angle and normalized amplitude of the pressure coefficients as a function of the dimensionless thickness of the subsonic region of the boundary layer at supersonic Mach numbers.

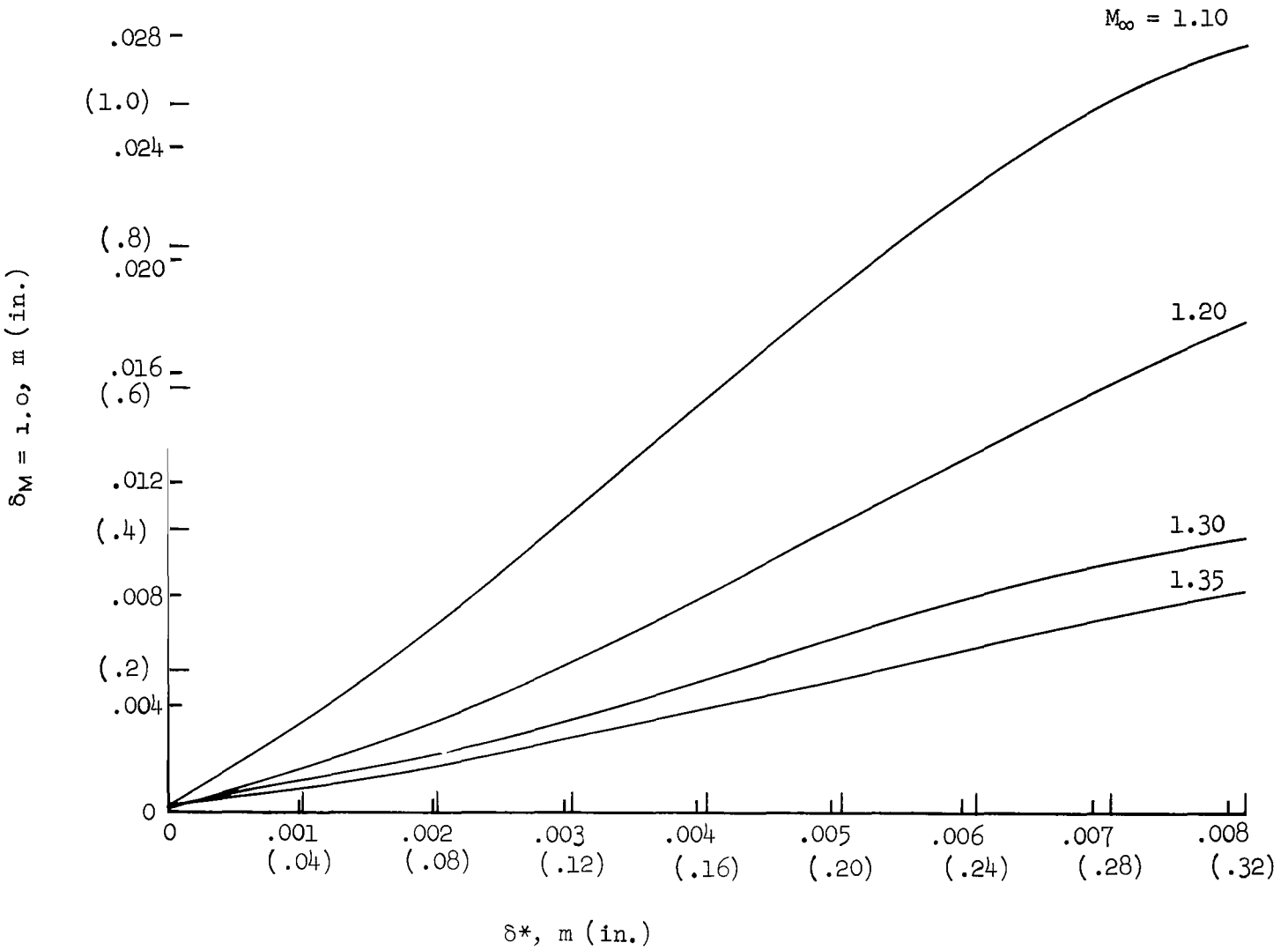

Figure 17.- Empirical relationship of $\delta_{M = 1.0}$ to δ^*.

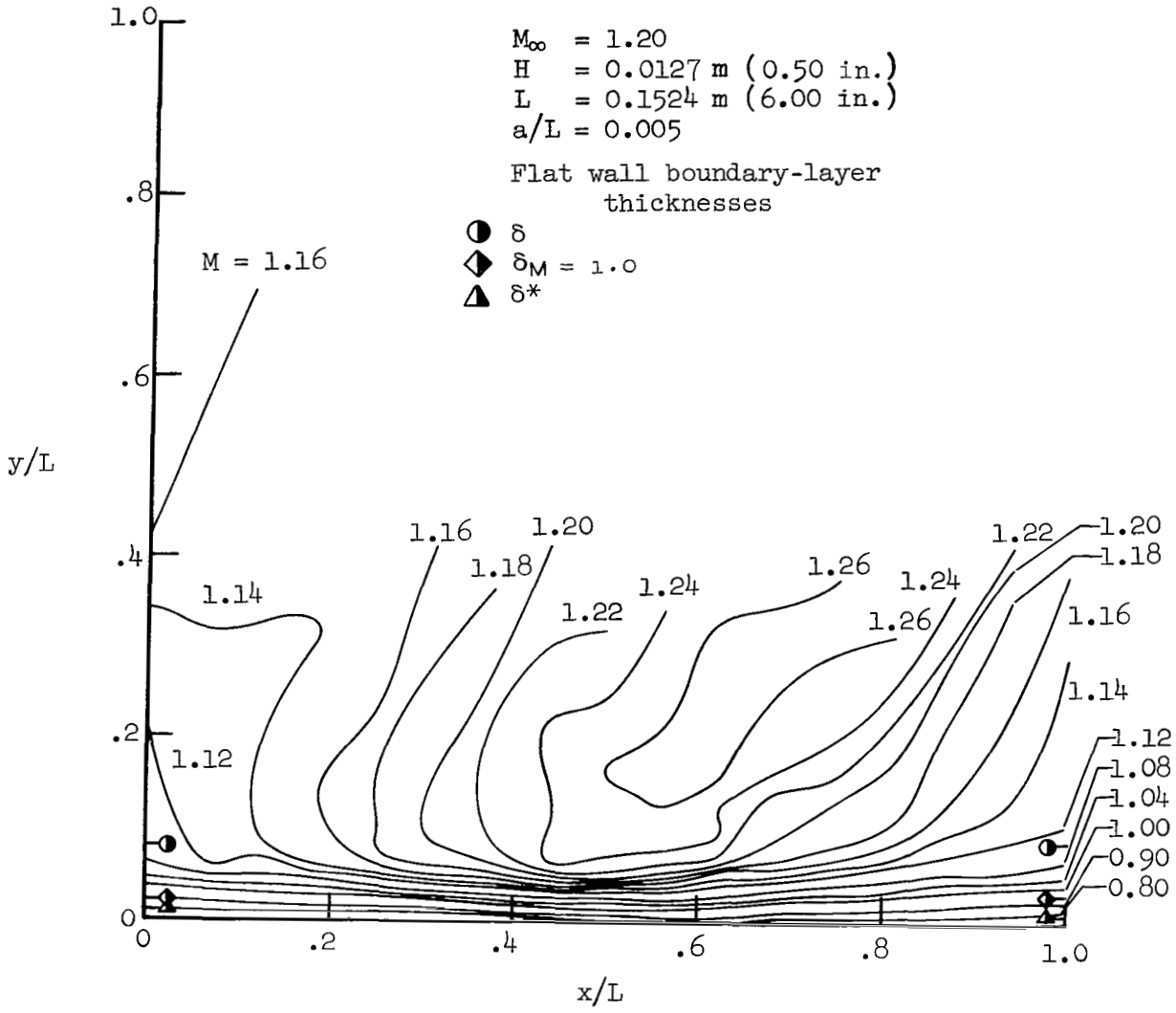

(a) M_∞ = 1.20, L = 0.15240 m (6.00 in.), H = 0.01270 m (0.50 in.)

Figure 18.- Constant Mach number contours within the boundary layer and free stream above the wavy-wall models.

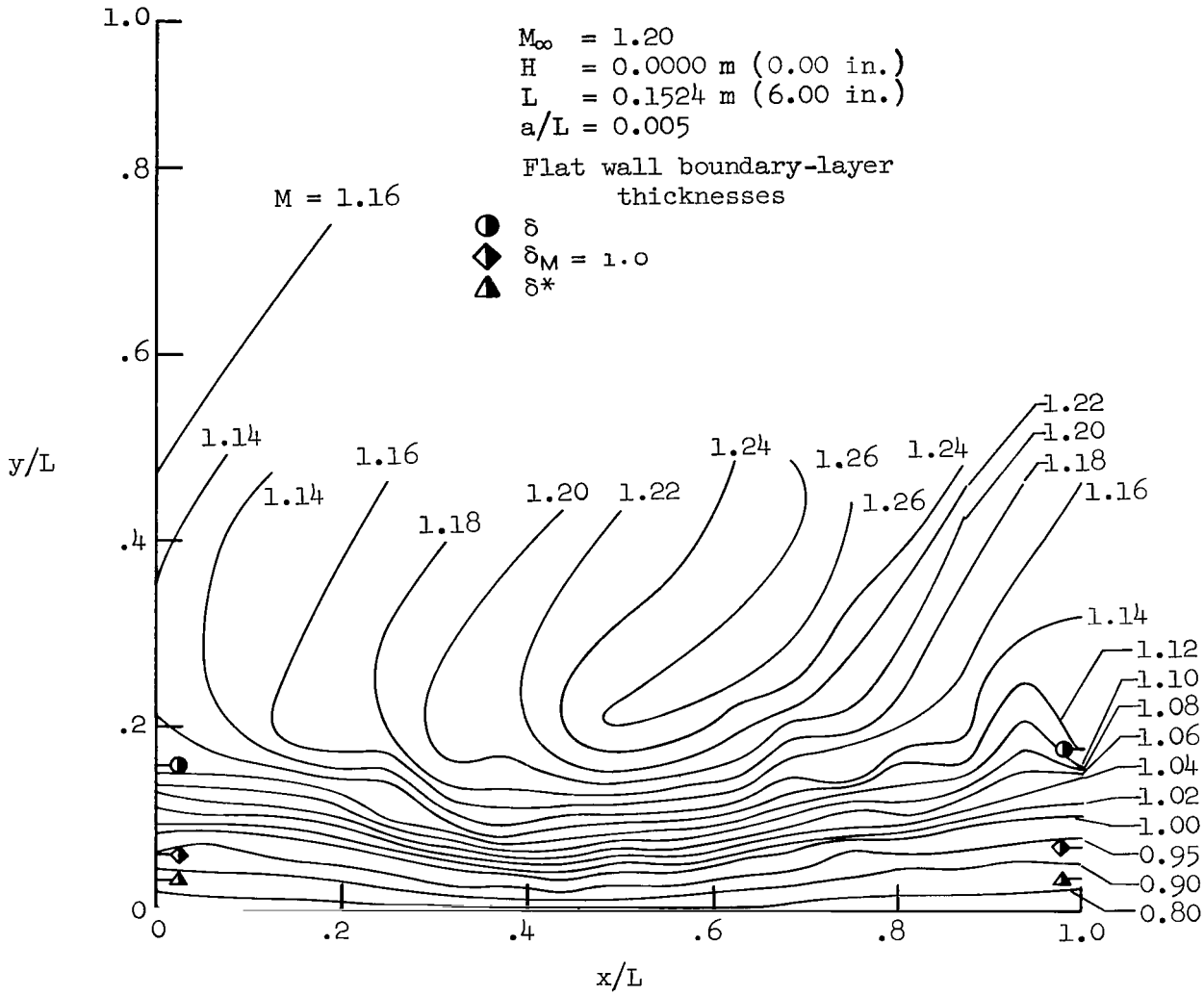

(b) M_∞ = 1.20, L = 0.15240 m (6.00 in.), H = 0.00 m (0.00 in.)

Figure 18.- Continued.

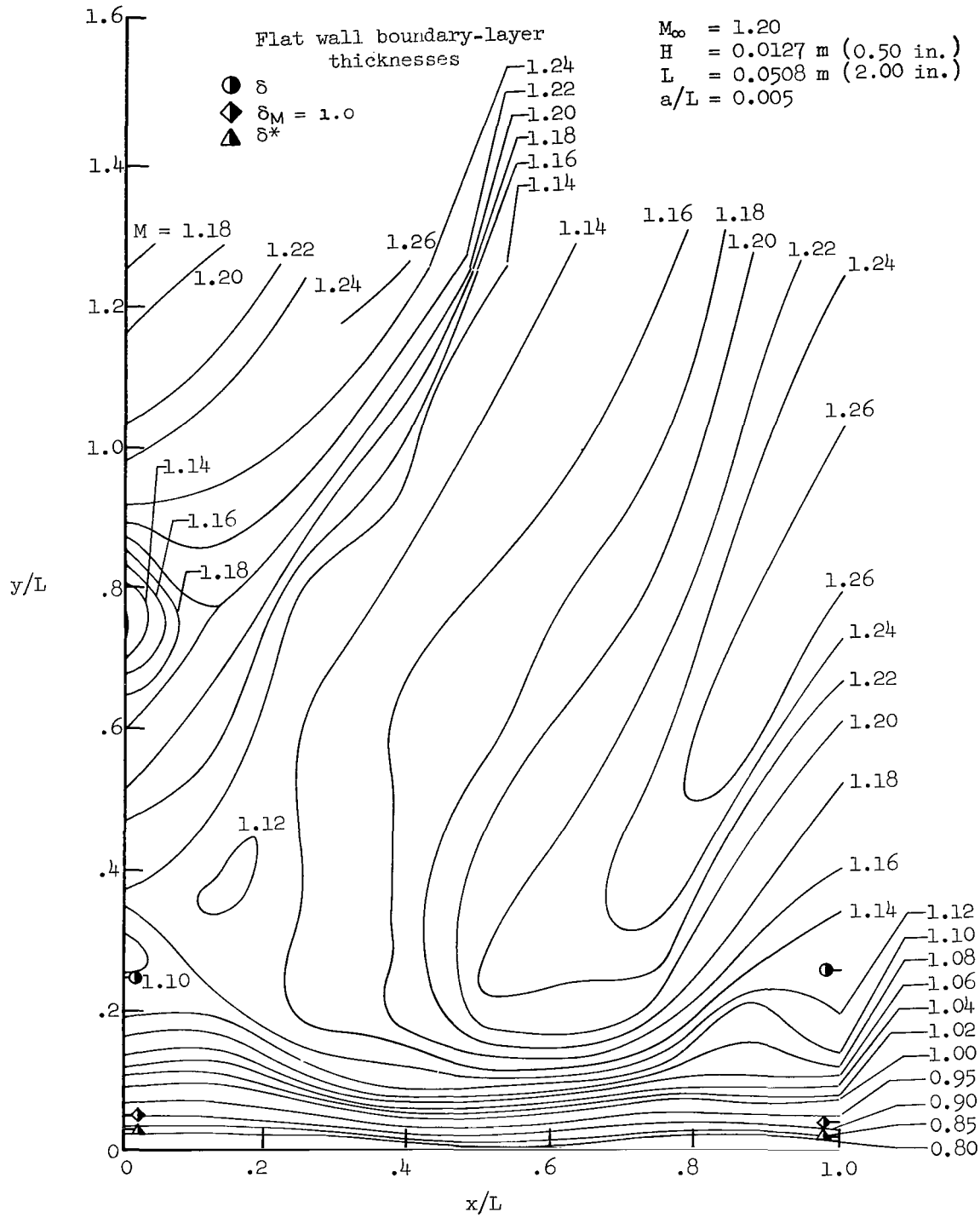

(c) M_∞ = 1.20, L = 0.05080 m (2.00 in.), H = 0.01270 m (0.50 in.)

Figure 18.- Continued.

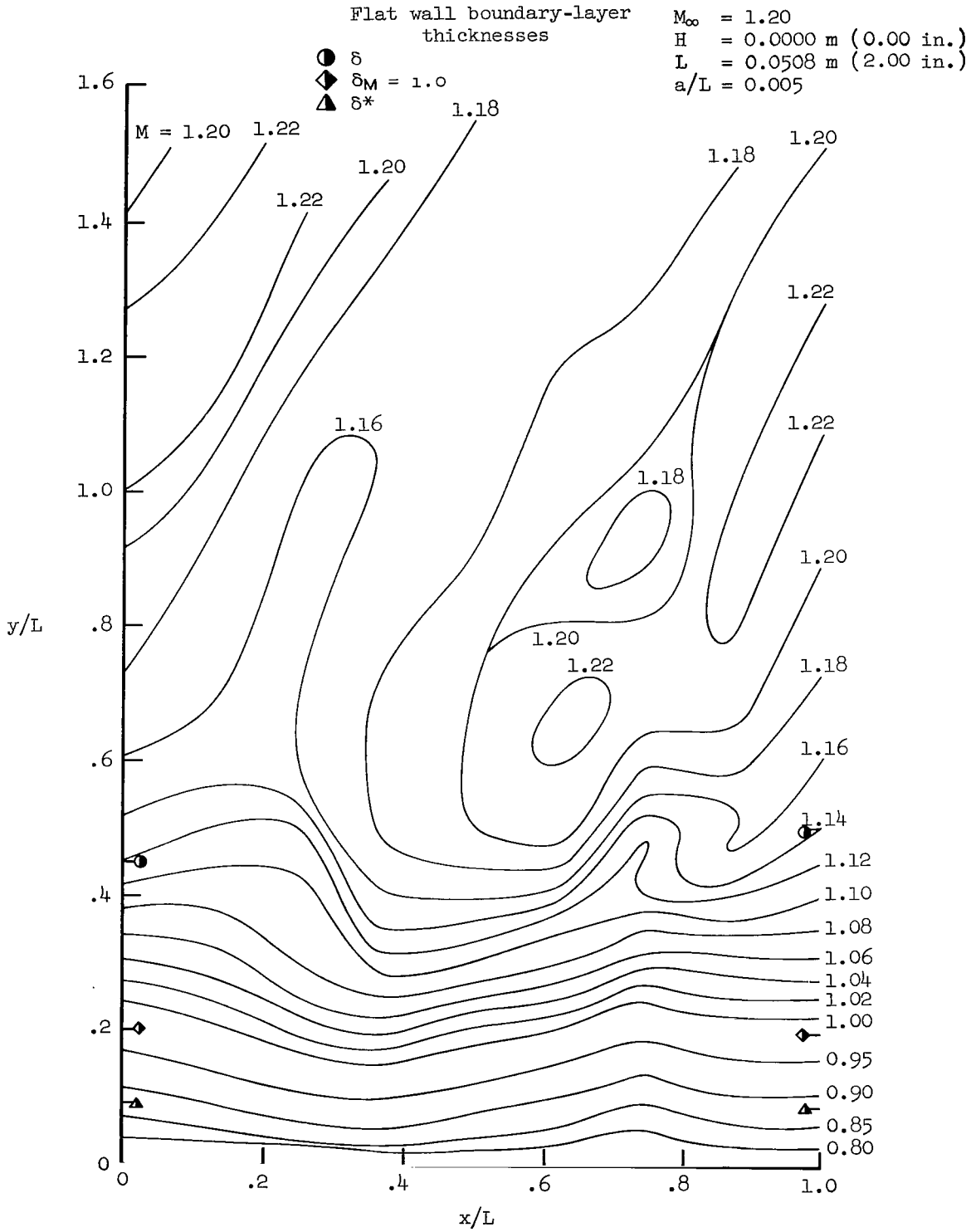

(d) M_∞ = 1.20, L = 0.05080 m (2.00 in.), H = 0.00 m (0.00 in.)

Figure 18.- Continued.

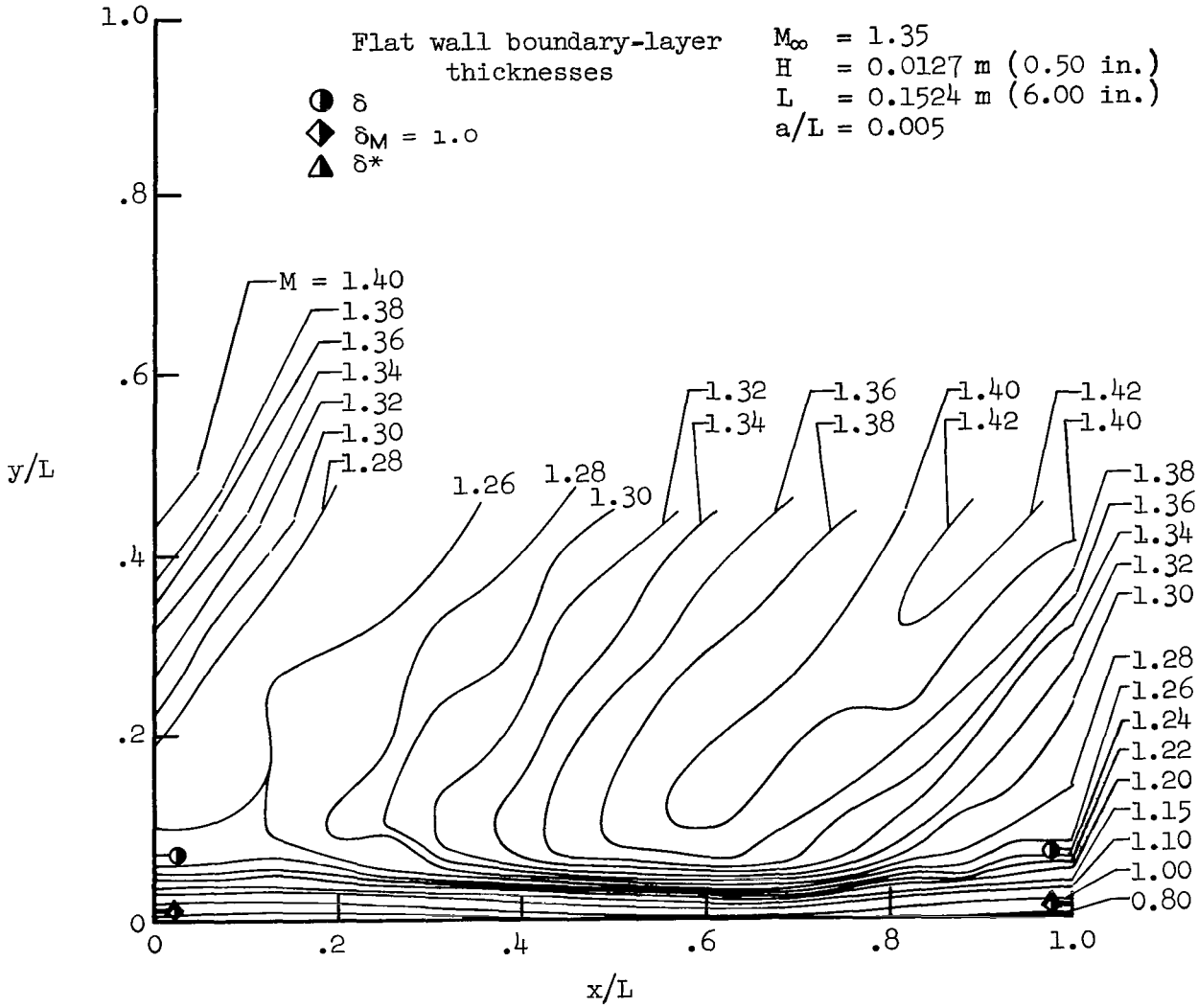

(e) $M_\infty = 1.35$, L = 0.15240 m (6.00 in.), H = 0.01270 m (0.50 in.)

Figure 18.- Continued.

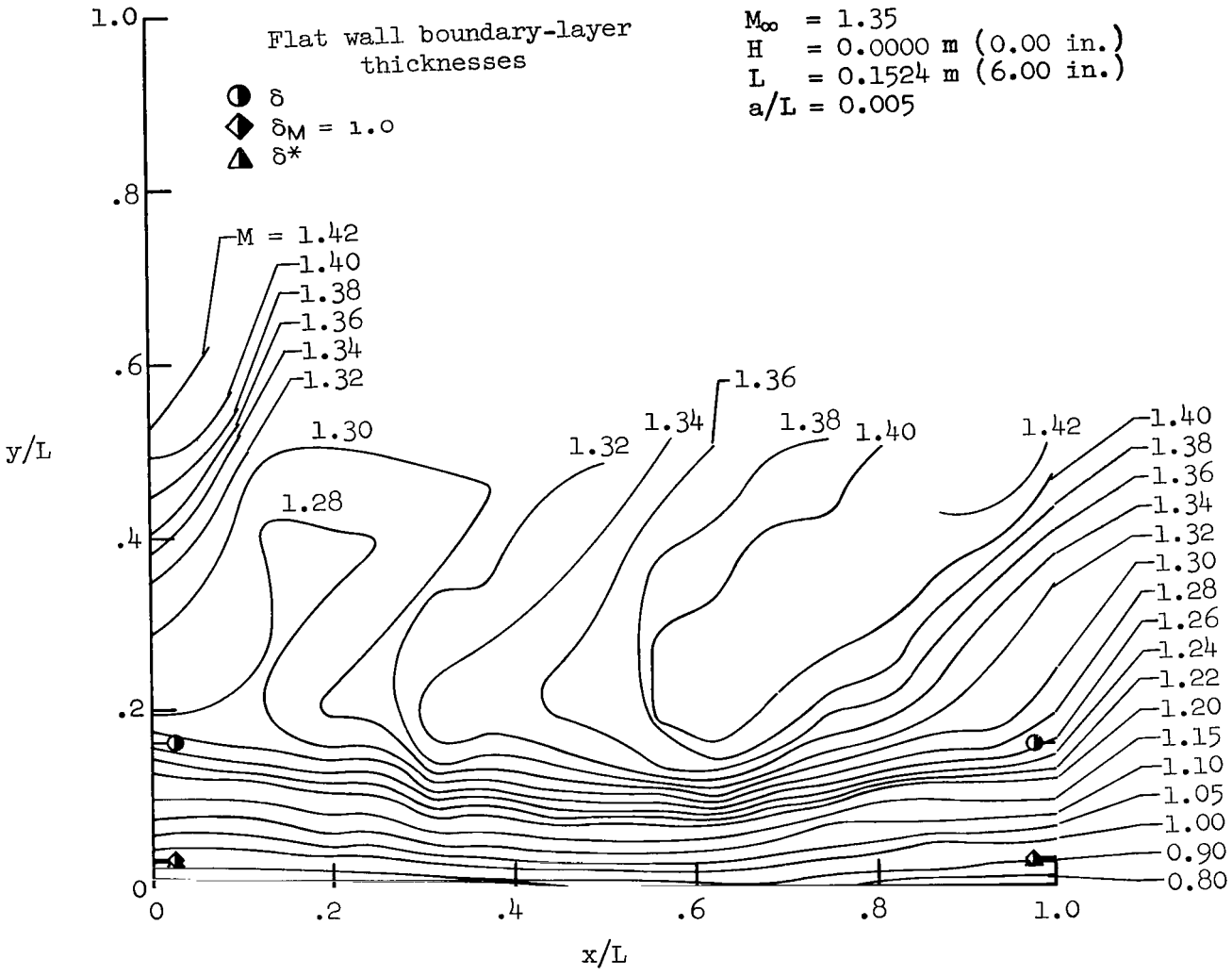

(f) M_∞ = 1.35, L = 0.15240 m (6.00 in.), H = 0.00 m (0.00 in.)

Figure 18.- Concluded.

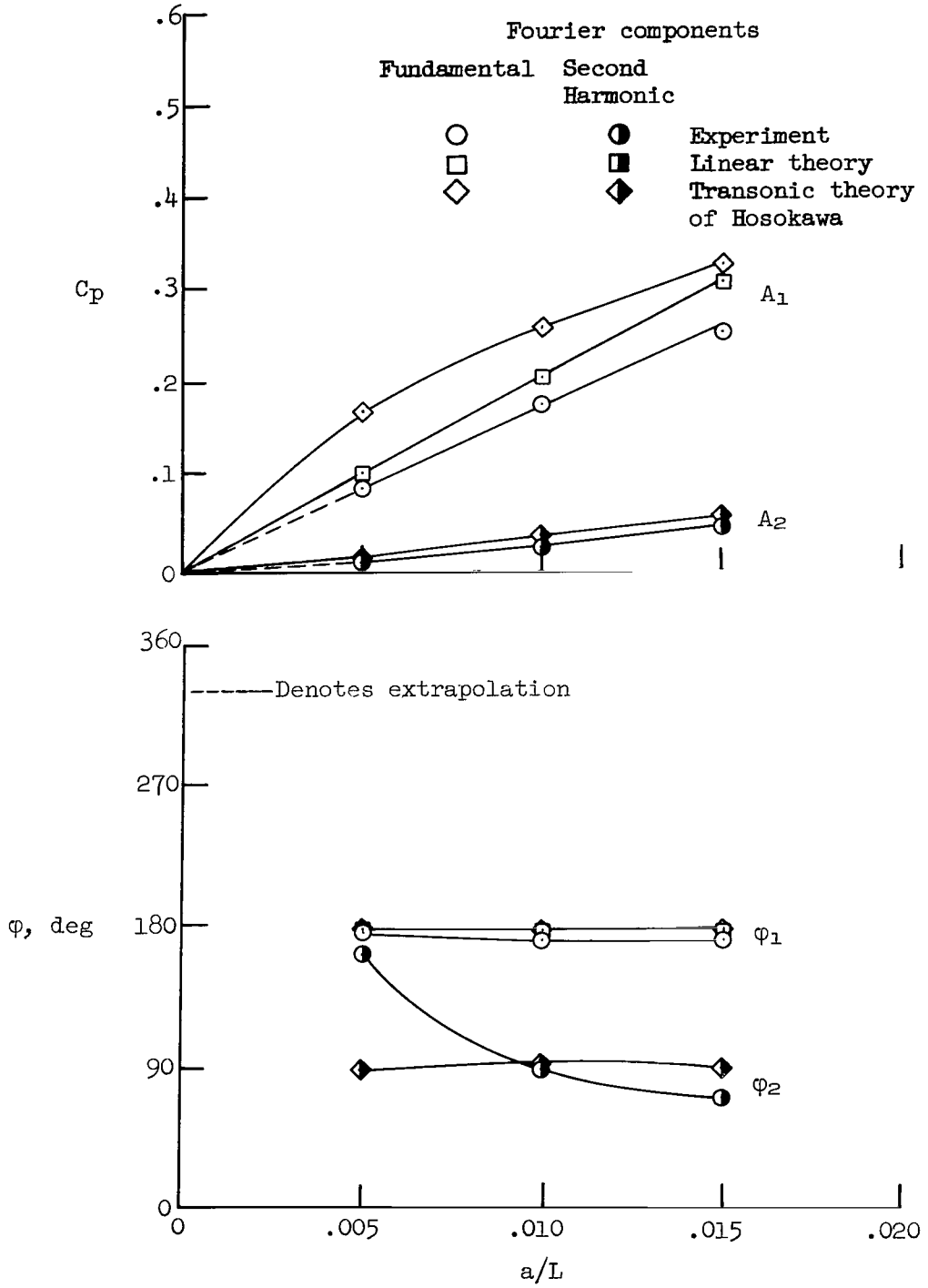

(a) $M_\infty = 0.80$

Figure 19.- Comparison of zero boundary-layer thickness experimental results as a function of amplitude-to-wavelength ratio with predictions of three theories.

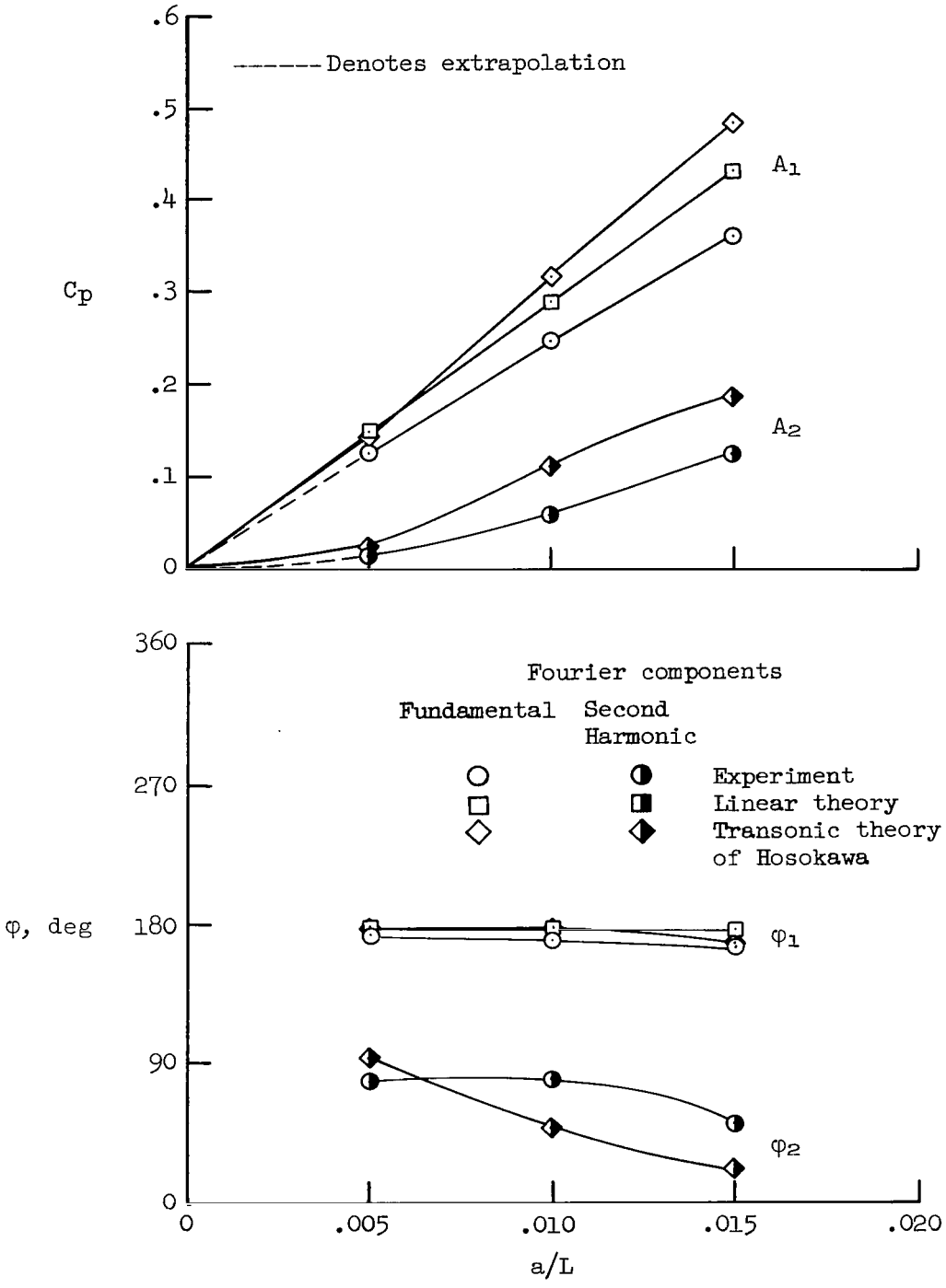

(b) $M_\infty = 0.90$

Figure 19.- Continued.

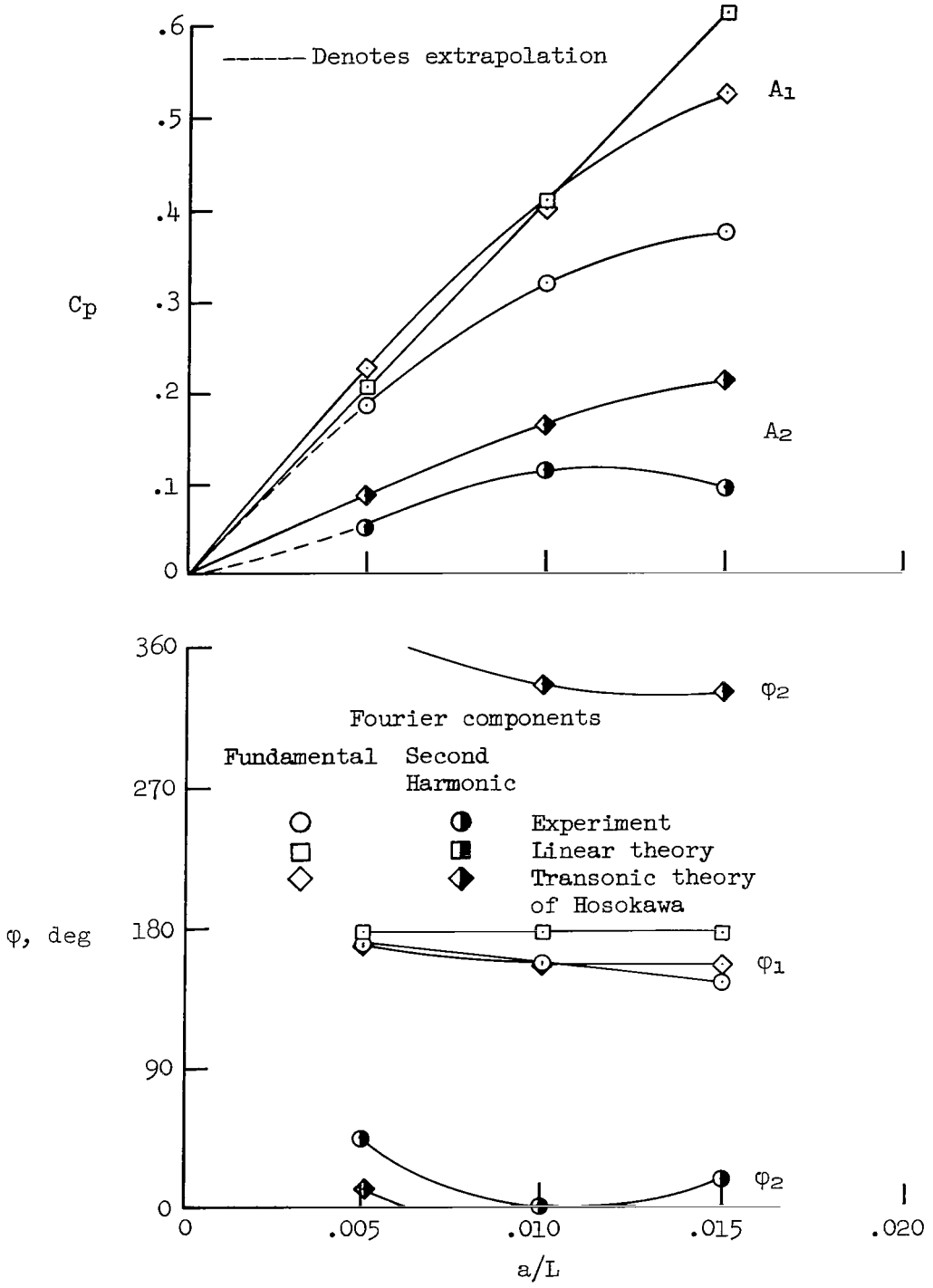

(c) $M_\infty = 0.95$

Figure 19.- Continued.

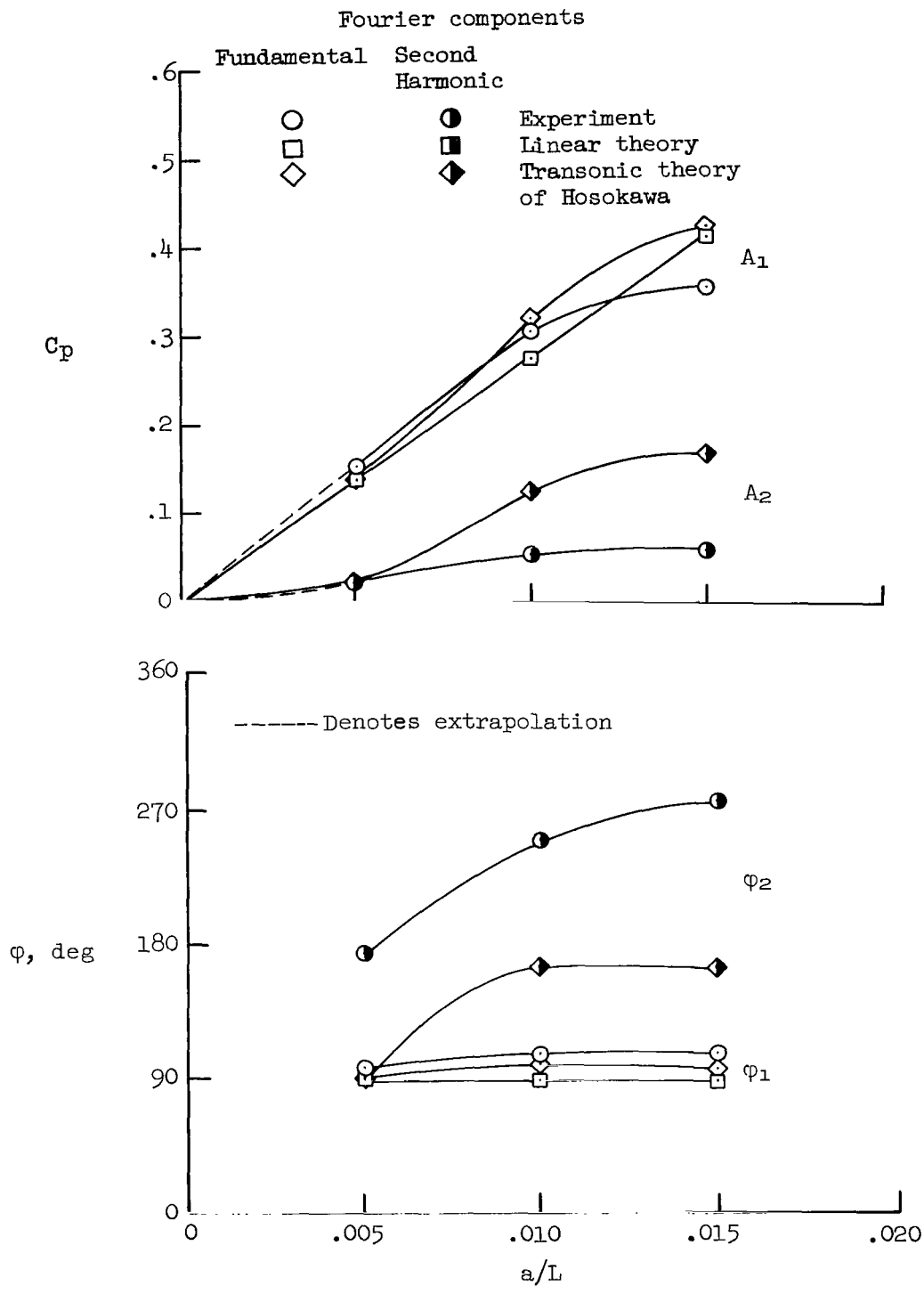

(d) $M_\infty = 1.10$

Figure 19.- Continued.

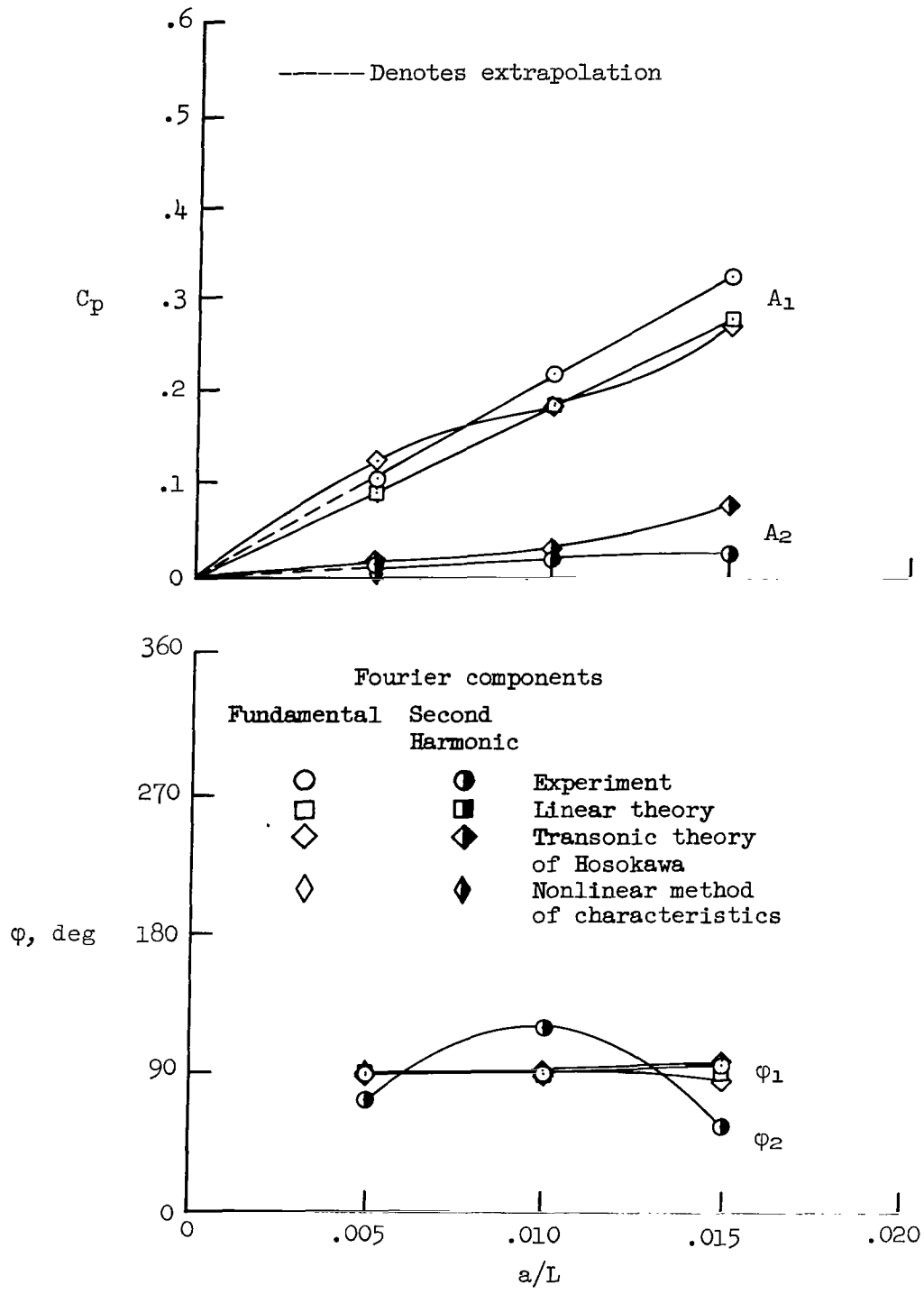

(e) $M_\infty = 1.20$

Figure 19.- Continued.

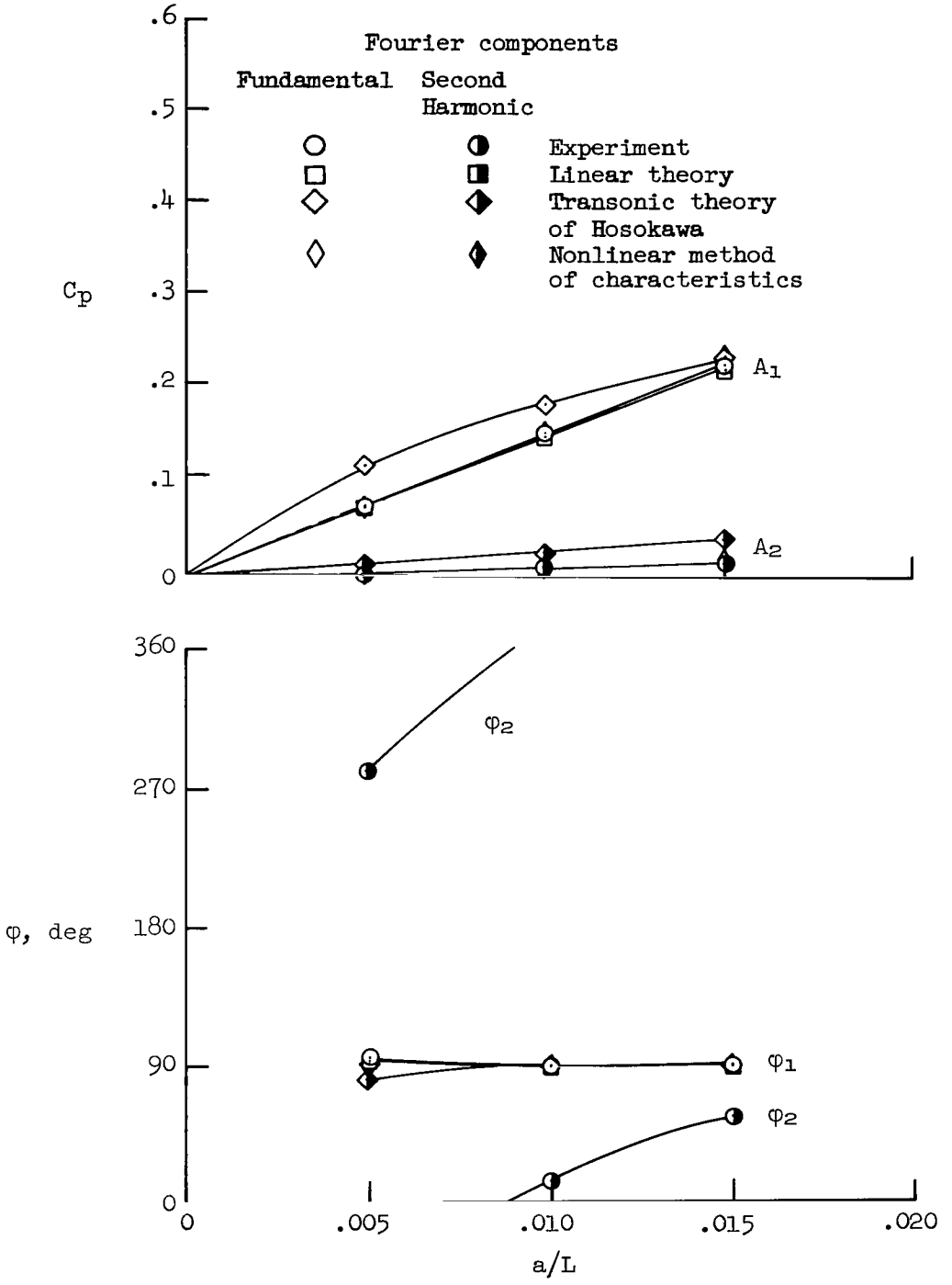

(f) $M_\infty = 1.30$

Figure 19.- Concluded.

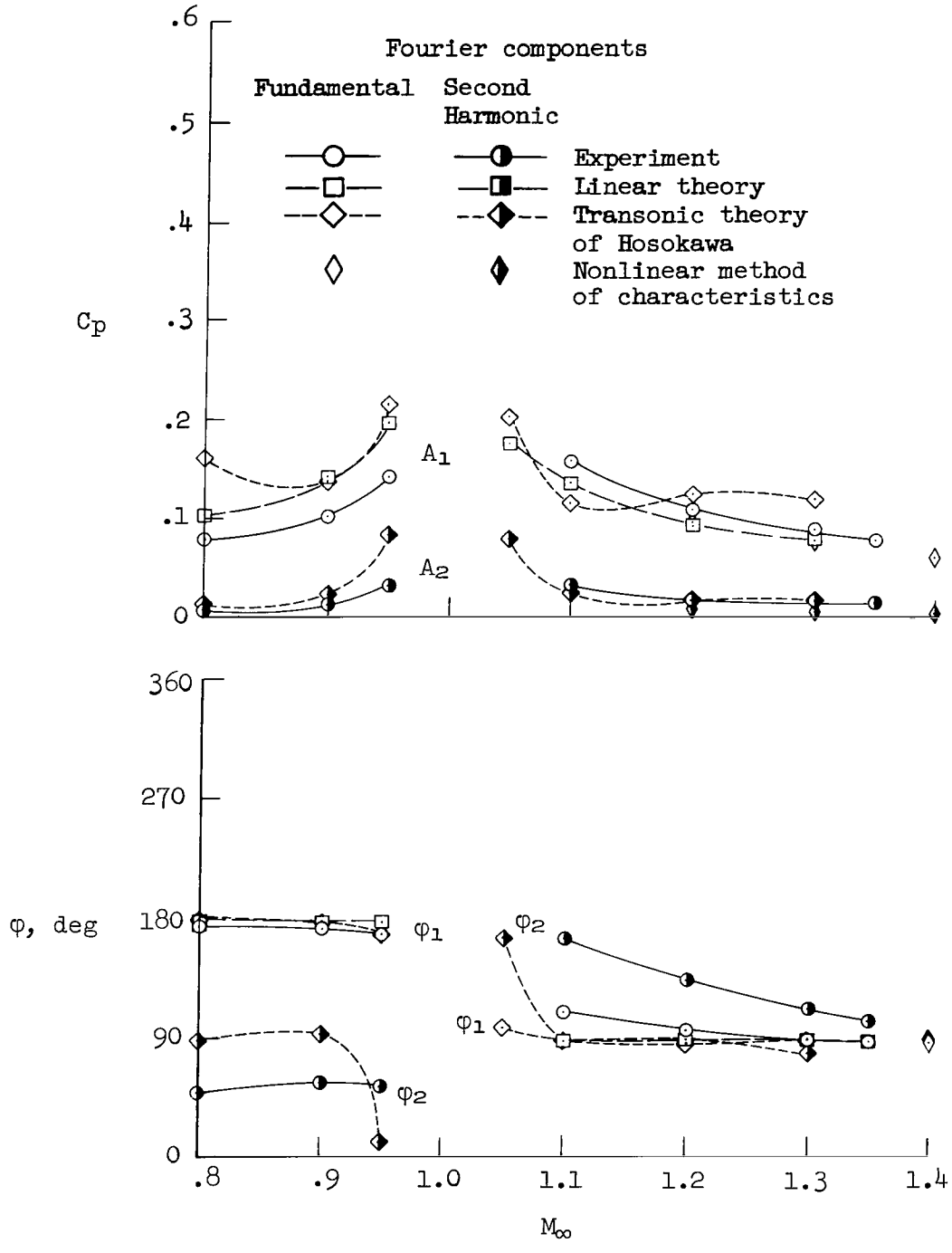

(a) a/L = 0.005

Figure 20.- Comparison of zero boundary-layer thickness experimental results as a function of Mach number with predictions of three theories.

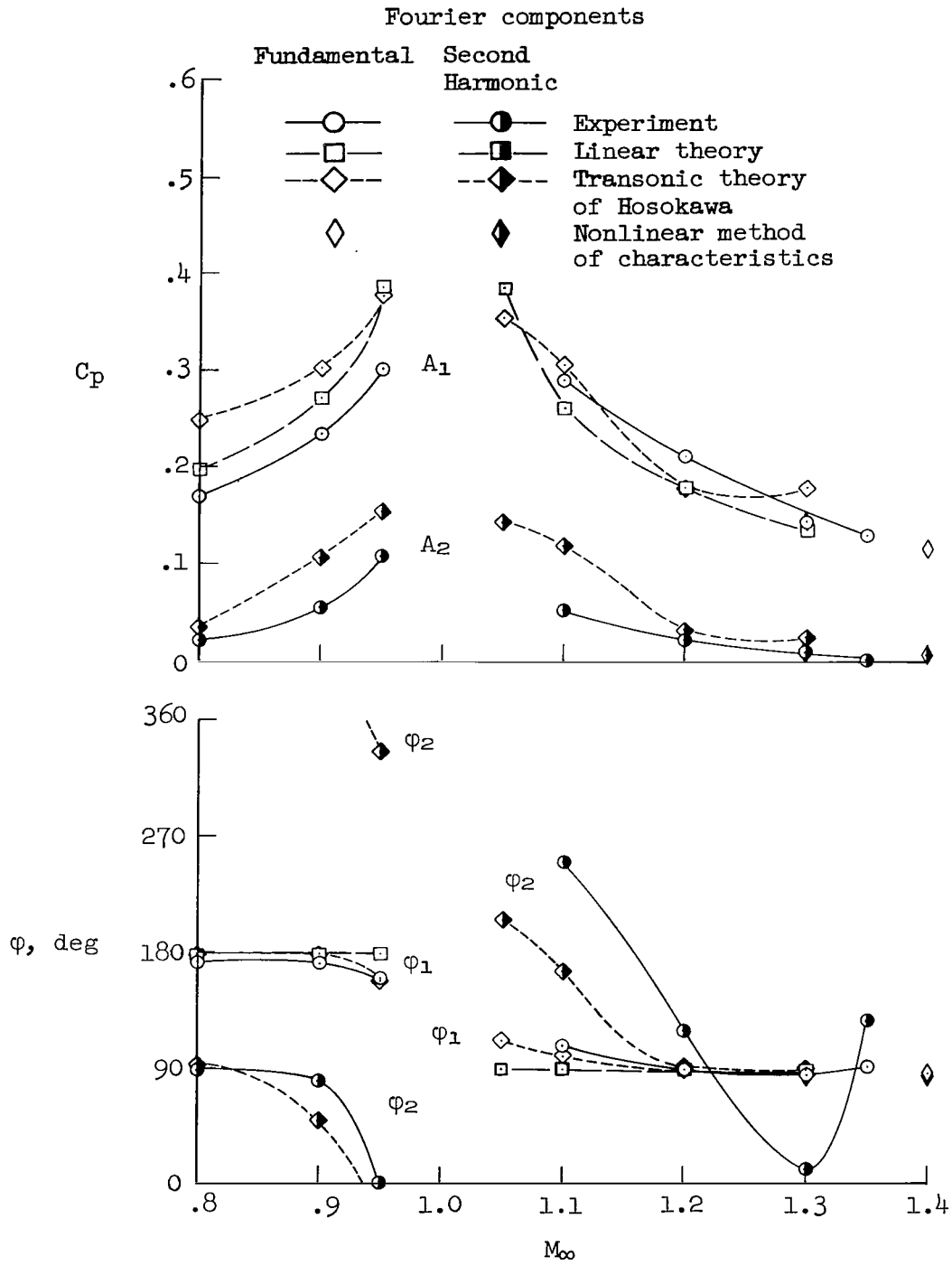

(b) a/L = 0.010

Figure 20.- Continued.

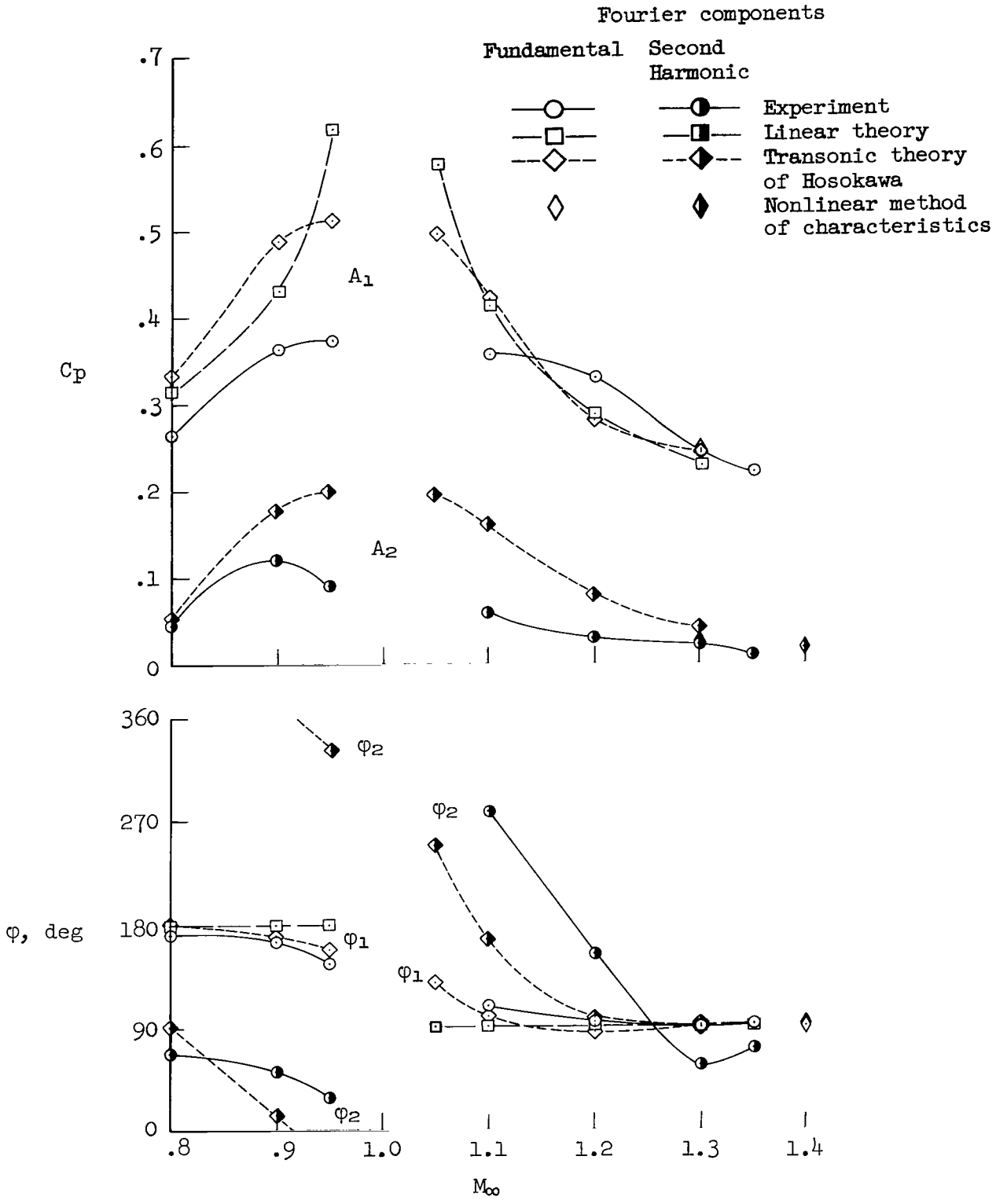

(c) a/L = 0.015

Figure 20.- Concluded.

NASA-Langley, 1971 — 12 A-3846

029 001 C1 U 12 710813 S00903DS
DEPT OF THE AIR FORCE
AF SYSTEMS COMMAND
AF WEAPONS LAB (WLOL)
ATTN: E LOU BOWMAN, CHIEF TECH LIBRARY
KIRTLAND AFB NM 87117

"The aeronautical and space activities of the United States shall be conducted so as to contribute . . . to the expansion of human knowledge of phenomena in the atmosphere and space. The Administration shall provide for the widest practicable and appropriate dissemination of information concerning its activities and the results thereof."

— NATIONAL AERONAUTICS AND SPACE ACT OF 1958

NASA SCIENTIFIC AND TECHNICAL PUBLICATIONS

TECHNICAL REPORTS: Scientific and technical information considered important, complete, and a lasting contribution to existing knowledge.

TECHNICAL NOTES: Information less broad in scope but nevertheless of importance as a contribution to existing knowledge.

TECHNICAL MEMORANDUMS: Information receiving limited distribution because of preliminary data, security classification, or other reasons.

CONTRACTOR REPORTS: Scientific and technical information generated under a NASA contract or grant and considered an important contribution to existing knowledge.

TECHNICAL TRANSLATIONS: Information published in a foreign language considered to merit NASA distribution in English.

SPECIAL PUBLICATIONS: Information derived from or of value to NASA activities. Publications include conference proceedings, monographs, data compilations, handbooks, sourcebooks, and special bibliographies.

TECHNOLOGY UTILIZATION PUBLICATIONS: Information on technology used by NASA that may be of particular interest in commercial and other non-aerospace applications. Publications include Tech Briefs, Technology Utilization Reports and Technology Surveys.

Details on the availability of these publications may be obtained from:

SCIENTIFIC AND TECHNICAL INFORMATION OFFICE

NATIONAL AERONAUTICS AND SPACE ADMINISTRATION

Washington, D.C. 20546